MICROFLUIDIC RESISTANCE SENSING FOR SINGLE CELL GROWTH RATE MEASUREMENTS AND CELL SEPARATION CHARACTERIZATION

By

Jiashu Sun

Dissertation

Submitted to the Faculty of the

Graduate School of Vanderbilt University

For the degree of

DOCTOR OF PHILOSOPHY

in

Mechanical Engineering

December 2010

Nashville, Tennessee

Approved:

Professor Deyu Li

Professor Erik M. Boczko

Professor Robert W. Pitz

Professor Greg D. Walker

Professor Yaqiong Xu

To Dad and Mom,

Weiping Sun and Jing Zhang

ACKNOWLEDGMENTS

First and foremost I would like to gratefully and sincerely thank my advisor, Dr. Deyu Li, for his guidance, patience, encouragement and never-ending support during my doctoral studies. This study would never have taken place without his insightful ideas and countless hours of instruction he provided. He also encouraged me to not only grow as an experimentalist but also an independent researcher. It is true that "The great teacher inspires" when I have been inspired by his enthusiasm for science and proficiency in research. His example will always serve as guidelines for my future career. I am very fortunate to gain a mentor like Dr. Deyu Li, and I will be forever grateful to him.

I would also like to express my greatest gratitude to Dr. Erik M. Boczko for exposing me the field of biophysics and working with me on yeast. His expertise in mathematical biology and gentle way of support has meant more to me than I could ever express. No matter how busy he was, he has always been there with patience when I needed his help. I could not have completed this work without him.

I would like to thank all the other members of my dissertation committee, Dr. Robert W. Pitz, Dr. Greg D. Walker, and Dr. Yaqiong Xu for their valuable comments, gentle encouragement and flexibility in scheduling.

My gratitude is also extended to Dr. Dongyan Xu, Dr. Yandong Gao, Dr. Juekuan Yang, Dr. Saumitra K. Vajandar, Mr. Yang Yang, Mr. Scott W. Waltermire and other group members. They are the most dedicated and generous people and I feel blessed to have the opportunity to work with them.

I take this opportunity to thank Dr. Dongqing Li, Dr. Charles P. Lin, Dr. Christopher C. Stowers, Dr. Jake Isaacs, Dr. Yuejun Kang, Dr. Guoqing Hu, Dr.

Kimberly C. Boelte, and Dr. Manoj Sridhar, for all their help in terms of academic support and research related discussions.

A special acknowledgement goes to Ms. Suzanne Weiss, Ms. Myrtle Daniels, and Ms. Jean Miller, the administrative assistants, Mr. Robin Midgett and Mr. Gary Walker, the electronics and mechanical technicians for taking care of all the important administrative and technical matters during my graduate study.

Finally, I will forever be indebted to my parents, Weiping Sun and Jing Zhang. They always have faith in me and supported everything I have ever attempted. Their endless love and encouragement allowed me to finish this journey, and hope this work could make them be proud of me.

TABLE OF CONTENTS

Page

LIST OF FIGURES

LIST OF TABLES

CHAPTER I

INTRODUCTION

Overview

Microfluidic lab-on-a-chip technologies show great promise for interrogating small cell populations or even single cells. These technologies provide many benefits, including compactness, portability, reduced reagent consumption, high throughput, and integration of multiple functions. Some lab-on-a-chip devices are simply scaled-down versions of conventional lab techniques, while other devices are equipped with novel functions taking advantage of the small length scales and low Reynolds numbers in microsystems. This dissertation aims at development of novel on-chip resistance sensing technologies, which have extensive applications in biological analysis. The on-chip resistance sensing technologies discussed in this dissertation include a MOSFET-based resistive-pulse sensing scheme and a reference-channel based resistance sensing scheme. Their applications are demonstrated by measurements of the volume growth rate of single budding yeast cells and characterization of the performance of size-based on-chip dielectrophoretic cell separation.

The dissertation is organized as follows. Chapter I introduces the background of resistive-pulse sensing, yeast cell volume growth, and on-chip cell separation. Chapters II and III discuss the MOSFET-based resistive-pulse sensing scheme and the reference channel-based resistance sensing scheme and their applications to the study of the volume growth rate of single budding yeast cells, respectively. Chapter IV describes size-based dielectrophoretic separation and characterization of its performance with the MOSFET-based resistive-pulse sensing. Finally, Chapter V summarizes the research work and points out some future research directions.

The Resistive-Pulse Sensing Scheme

Resistive-pulse sensing is based on a small sensing aperture separating two fluidic chambers containing electrolytes. A baseline ionic current through the sensing aperture is induced by applying an electrical bias between the two chambers. When a small particle, such as a bacterium, a cell, or a molecule, is translocated through the sensing aperture, it displaces a small amount of electrolyte equivalent to its own volume, which consequently leads to a transient modulation of the electrical resistance of the sensing aperture. Under favorable conditions, this resistance modulation can be employed to count and size the particles, and determine their surface charges as well.

The study of electrical resistance modulation from the presence of non-conducting spheres in a conducting medium was first carried out by Maxwell (Maxwell and Thomson, 1904), who derived the effective resistivity, ρ_{eff}, of an infinitely dilute suspension of non-conducting spheres in a solution of resistivity, ρ_s, as:

$$\rho_{eff} = \rho_s\left(1 + \frac{3f}{2} + \cdots\right), \qquad (1.1)$$

where f is the volume fraction of the spheres in the suspension.

Considering a tube of diameter D and length L, filled with a solution of resistivity, ρ_s, the resistance of the tube in the case of $L>>D$ is given as (DeBlois and Bean, 1970):

$$R = 4\rho_s L/\pi D^2, \qquad (1.2)$$

If a sphere of diameter $d<<D$ is located inside the tube (as shown in Fig. 1.1), the fraction (*f*) of the volume of the sphere (*ΔV*) to the total volume of the tube (*V*), can be written as:

$$f = \triangle V/V = 2d^3/3D^2L, \tag{1.3}$$

Combining Eqns. 1.1, 1.2, and 1.3, the resistance of the tube with a small sphere of diameter *d* inside can be determined as:

$$R^{'} = (4\rho_s L/\pi D^2)(1 + d^3/D^2L + \cdots), \tag{1.4}$$

The resistance modulation, *ΔR*, can then be written as:

$$\triangle R = R^{'} - R = 4\rho_s d^3/\pi D^4, \tag{1.5}$$

Therefore, the relative resistance modulation due to the presence of a non-conducting sphere, *ΔR/R*, can be derived as:

$$\triangle R/R = d^3/D^2L = \frac{3}{2} \triangle V/V, \tag{1.6}$$

If a constant current, *I*, is passed through the tube, the relative increase in voltage drop across the tube, *ΔU/U*, can be derived as:

$$\triangle U/U = I \triangle R/I\,R = d^3/D^2L = \frac{3}{2} \triangle V/V, \tag{1.7}$$

Note that the amplitude of the voltage modulation is proportional to the volume fraction in the limit of $d<<D$. Similarly, if the electrical potential drop across the aperture is kept constant, then a corresponding ionic current modulation will occur.

The classical example of resistive-pulse sensors is the Coulter counter, a commercially available device invented by W. H. Coulter in 1948 and patented in 1953 (Coulter, 1953). The Coulter counter is commonly used to count and size biological cells, microorganisms, and other small particles suspended in a conducting fluid (Bayley and Martin, 2000).

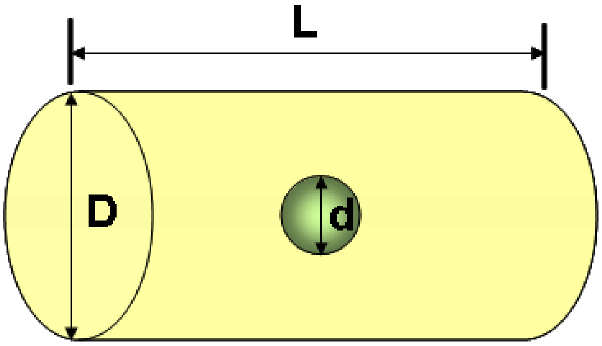

Figure 1.1: A schematic diagram of a non-conducting sphere of diameter *d*, inside a tube of diameter *D* and length *L*, filled with a solution of resistivity ρ_s.

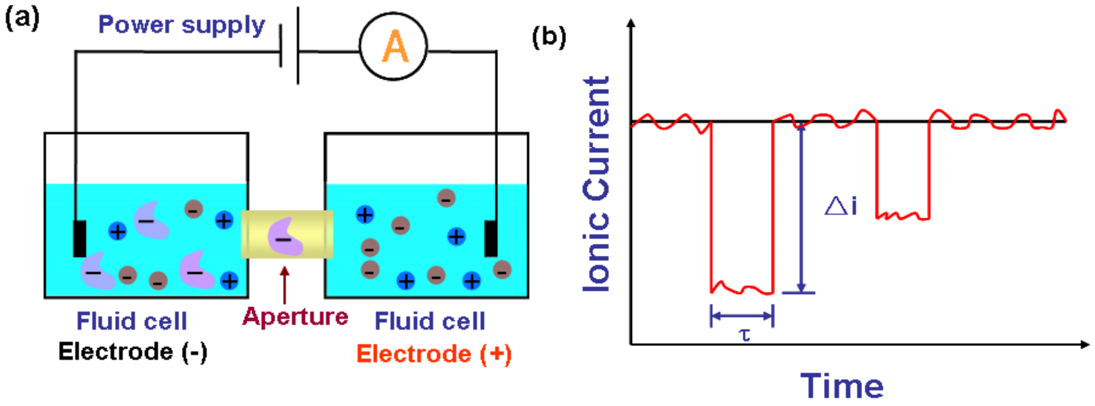

Figure 1.2: The working principle of a Coulter counter. (a) A schematic of the basic components of a Coulter counter – a small sensing aperture embedded between two fluid reservoirs and a baseline ionic current is induced through this aperture by applying an electrical bias; (b) A schematic of the typical signals of a Coulter counter. The number of pulses gives a count of the number of particles flowing through the aperture. The amplitude of the current pulses can be used to determine the size of the analyzed particles under favorable conditions.

Coulter (Coulter, 1956) first applied this device to count and size blood cells (6 ~ 8 µm in diameter) at a high count rate of ~6000 cells/s. In general, the detection limit of Coulter counters is restricted by the diameter of the sensing aperture (from ~20 µm to ~2 mm) (Bayley and Martin, 2000). To extend the detection limit, it is essential to fabricate smaller apertures. Kubitschek (Kubitschek, 1958) later fabricated a Coulter counter with a sensing aperture (10 µm in diameter and 50 µm in length) smaller than Coulter's original aperture (~100 µm in diameter) and successfully detected bacteria. The smallest volume of bacteria that can be detected with this device was ~0.2 μm^3, corresponding to a minimum volume ratio of 0.005%. DeBlois and Bean (DeBlois and Bean, 1970) further extended the detection limit to ~0.06 µm diameter objects through the use of individual submicron pores etched in irradiated plastic sheet. Their experimental results yielded a minimum volume ratio of 0.06 %. Over the past few decades, continuous optimization of Coulter counters led to diverse applications, such as to determine the size of different types of viruses ranging from 110 nm to 140 nm (DeBlois and Wesley, 1977), to accurately count and size particles at a high rate (Sikdar and Webster, 1980), and to study the dissolution of air bubbles and radial migration of particles as a function of time (Berge et al., 1989).

An important trend in Coulter counter development over the past two decades is to fabricate nanoscale sensing apertures that allow for detection of nanoscale particles and molecules. Bezrukov and co-workers (Bezrukov et al., 1994) used a single alamethicin channel (~5 nm long and ~ 2 nm in diameter) to detect single molecules with gyration radii as small as 5-15 Å. Kasianowicz and colleges (Kasianowicz et al., 1996) designed a 2.6 nm-diameter ion channel in a lipid bilayer membrane that was able to detect single DNA and RNA molecules. Later, various protein nanopores have been adapted to studying DNA translocation and its dynamics (Deamer and

Akeson, 2000; Bayley and Martin, 2000; Bayler and Cremer, 2001; Meller and Branton, 2002). However, the intrinsic instability of the protein nanopores restricted their usage in engineering devices for scientific research and clinical applications. One solution was to fabricate more robust, solid-state nanoscale apertures. Li and collaborators (Li et al., 2001; Li et al., 2003) demonstrated that ion and electron beam technologies could be used to successfully fabricate desired nanopores from solid-state materials, such as silicon nitride. These nanopores can serve as the critical components in the ultra-sensitive electromechanical devices that are capable of studying single DNA molecules and their folding behavior. In more recent years, other nanopore-based nanofluidic devices capable of detecting and discriminating individual biomolecules have been reported by different groups (Chang et al., 2004; Chen et al., 2004a; Chen et al., 2004b; Karnik et al. 2005; Fan et al. 2005; Fologea et al., 2005; Smeets et al., 2006).

Another trend in the development of Coulter counters is to create various kinds of on-chip devices for different biological applications. Compared to the conventional Coulter counter, on-chip Coulter counters have advantages such as they are portable, compact, consume a very low volume of reagent, reduce the cost for each device, and have the ability to integrate multiple functions. Larsen and co-workers (Larsen et al., 1997) reported the first on-chip Coulter counter aiming at counting and sizing live cells and particles in a liquid suspension. Their device was fabricated on a silicon substrate with standard silicon micromachining techniques and equipped with hydrodynamic focusing capability to reduce particle clogging in the sensing channel. Later, Koch and colleagues (Koch et al., 1999), and Roberts and co-workers (Roberts et al., 1999) designed and fabricated similar micromachined Coulter counters to detect particles in the size range of human blood cells. The schematic and SEM image of Koch’s device are shown in Fig. 1.3.

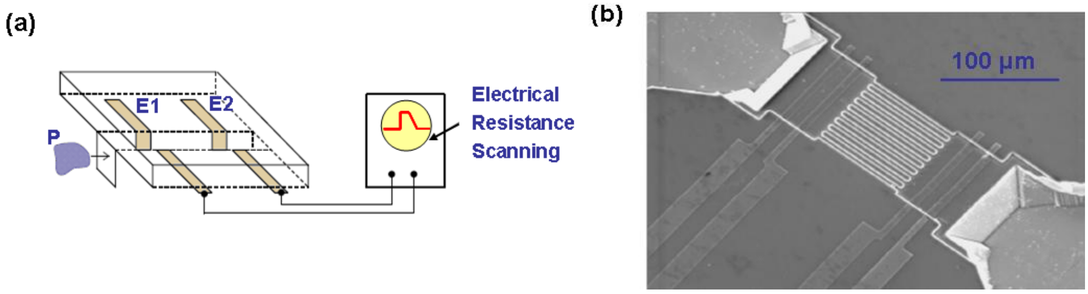

Figure 1.3: (a) A schematic of the micromachined Coulter counter; (b) An SEM image of the sensing channels and four titanium electrodes to allow for electrical measurements (Koch et al., 1999).

More recently, on-chip Coulter counters have been developed to detect single molecules and to incorporate new functions beyond simple particle counting and sizing. Saleh and Sohn (Saleh and Sohn, 2001) reported a microchip Coulter counter consisting of a sensing pore of 8.3 µm long and a cross section of 0.16 μm^2 to detect individual nanoscale colloidal particles as small as 87 nm in diameter. Later, they (Saleh and Sohn, 2003a) presented an on-chip microfluidic Coulter counter with an embedded artificial nanopore (200 nm in diameter and 3 µm in length) to detect single DNA molecules. The same authors (Saleh and Sohn, 2003b) also demonstrated a similar pore-based (1 µm in diameter and 7 ~ 9 µm in length) microfluidic device that enabled detection of antibody-antigen binding.

Just as conventional Coulter counters have a number of limitations, e.g., single analyte analysis at one time and low selectivity for particles of similar sizes, the on-chip Coulter counters are subjected to the same drawbacks as well. To deal with the compelling need for rapid multi-analyte analysis, Carbonaro and Sohn (Carbonaro and Sohn, 2005) integrated two pores (10 μm long, 1 μm wide and 1 μm high) on a single on-chip Coulter counter to perform multi-analyte immunoassay detection. To improve the throughput of the on-chip Coulter counters, Jagtiani and co-workers (Jagtiani et al., 2006) designed a multi-channel device that allowed parallel detection of particles or pollens. Later, Zhe and co-workers (Zhe et al., 2007) reported a design with four-parallel channels and electrodes in the middle of the sensing channel to eliminate the crosstalk between different channels, as shown in Fig. 1.4. This device showed a high throughput for pollen detection without compromising its sensitivity and reliability, compared with the single-channel device. In summary, to date, quite a few research groups have exploited various novel designs to enhance the capability of resistive-pulse sensing in order to realize high-speed counting and sizing.

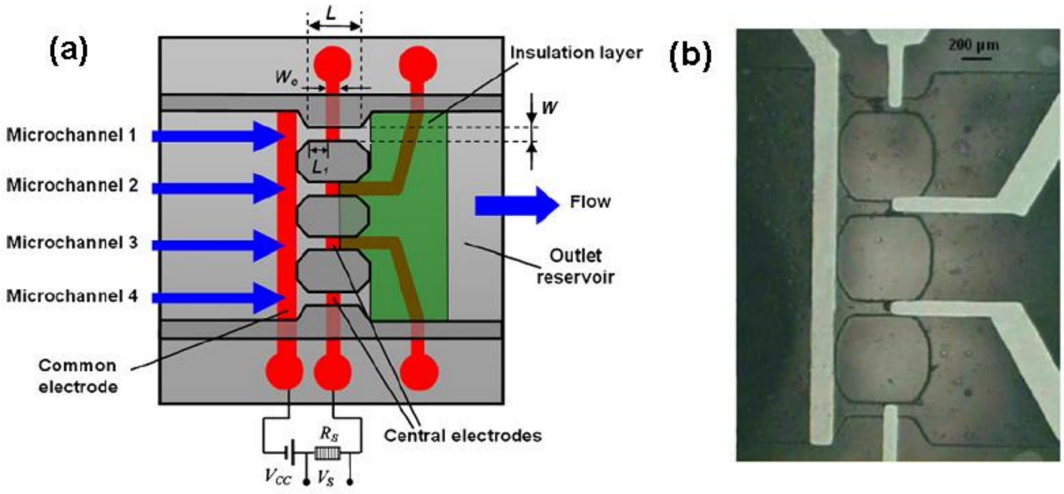

Figure 1.4: (a) A schematic of the on-chip multi-channel Coulter counter, which consisted of a pair of inlet and outlet reservoirs, connected by four parallel-sensing microchannels; (b) A microscopic image of the microchannels and the electrodes. The microchannels and reservoirs were built inside the polydimethylsiloxane (PDMS) and bonded to a glass substrate with gold electrodes on the surface (Zhe et al., 2007).

On the application side, commercial Coulter counters have been used for cell volume measurements (Bayley and Martin, 2000) and the elegance of Coulter counters is that under favorable conditions, the measurement results only depend on the volume of the electrolyte displaced by the cell, independent of the cell shape, color, or refractive index. This is a significant advantage over other cell volume measurement methods, whose results can be functions of cell parameters other than the cell volume. However, conventional Coulter counters have a few limitations for cell volume measurements. For example, commercial Coulter counters require that cells be suspended in a dielectric contrast fluid such as Isoton. These fluids lack the nutrients required for cell growth and cannot match the osmolarity of cell culture media. The difference in osmolarity can lead to swelling or even rupture of cells; and therefore, drastically affect the cell volume measurement. Another constraint of conventional Coulter counters is that it only makes one-time detection because of the unswitchable delivery routine, which prohibits successive volume measurements for single cells. There has been one report of constructing a pressure control system to reverse the pressure and deliver particles back and forth through the sensing aperture of a Coulter counter. The technique is demonstrated by successfully studying the size of a dissolving air bubble. However, the system requires a complex pressure control circuit and a pressure regulation system. In addition, the pressure-reverse can be affected by the drifting baseline signal (Berge et al., 1989).

Compared to their commercial counterparts, on-chip Coulter counters provide more flexibilities, which allow for adjustments with respect to different applications. However, all published on-chip Coulter counters are still based on a single-pass delivery routine. In this dissertation, we modify a recently developed MOSFET-based on-chip Coulter counter (Xu et al., 2007, Sridhar et al., 2008) to deliver a single growing yeast cell back and forth through the sensing channel. Taking advantage of the enhanced sensitivity of the MOSFET-based microfluidic Coulter counter and the flexibility of moving cells back and forth through the sensing aperture, we were able to measure the volume growth rate of individual budding yeast cells over their whole cell cycle. In addition, the measurement was made within the microfluidic device filled with the yeast nitrogen base (YNB), a suitable medium for culturing yeast, allowing cell growth in a physiologically relevant environment.

Yeast Volume Growth

The budding yeast, *Saccharomyces cerevisiae*, because of its simplicity, easy culturing, and short cellular life span, is a heavily studied eukaryotic model organism that has been used to study virtually every basic biological process from aging to stress, from apoptosis to quorum sensing and back again (Johnston and Singer, 1983, Gershon and Gershon, 2000, Bitterman et al., 2003, Mitchison, 2003). The budding yeast serves as a functional experimental object for studying complex human diseases and has found widespread application in bioprocess and industry. Currently, the budding yeast is at the center of several large scale systems biology and bioinformatics efforts aiming at extending the understanding of cell cycle progression, integration of genetic regulation, aging effect and physiological adaptation.

The cell cycle of the budding yeast *Saccharomyces cerevisiae* begins with the G_1 phase (gap 1) in which a single, unbudded yeast cell grows in volume. The transition between the G_1 phase and the S phase is marked by the emergence of a bud. The beginning of the S phase (synthesis) is usually defined as the commencement of DNA synthesis. At the end of the S phase, all chromosomes have been replicated. The cell then enters the G_2 phase (gap 2) and continues to grow. Meanwhile, the nucleus migrates to the junction between the cell and the bud. The G_2 phase is succeeded by the M phase (mitosis), during which cell growth stops and nuclear division occurs (Fig. 1.5). After cytoplasmic division is complete, the mother cell can be distinguished from the daughter by an observable bud scar on the surface of the mother cell (Baumstarkkhan et al., 1986; John, 1981; Blow, 1996).

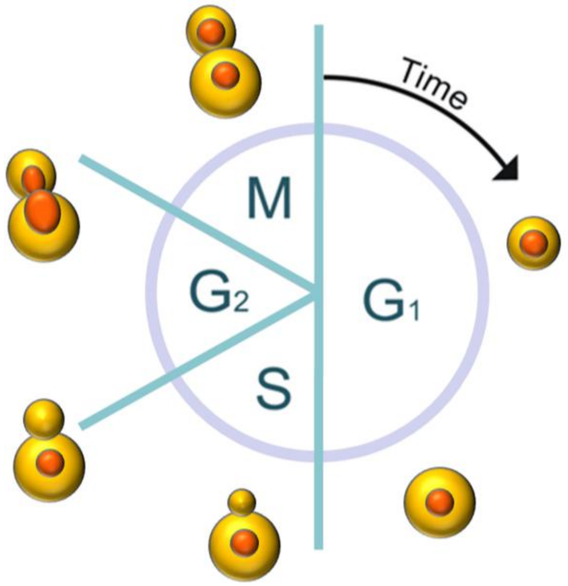

Figure 1.5: A schematic diagram of the budding yeast cell cycle. The yeast cell cycle begins with the G_1 phase. During this phase, a single, unbudded yeast cell grows in volume. The bud emerges at the beginning of the S phase, during which each chromosome is replicated. The cell continues to grow in the G_2 phase in which the nucleus migrates to the junction between the cell and the bud. The cell then enters the M phase, during which cell growth stops and nuclear division occurs (Blow, 1996).

An accurate measurement of budding yeast cell cycle and growth rate has important significance for extending cell cycle synchrony. Traditionally, most yeast assays are performed on ensembles of yeast cells. It has been generally accepted that the accuracy of the ensemble-based bioassays depends crucially upon the cell population synchrony, which for budding yeast has been determined by tracking the percentage of the yeast cells with buds in a whole cell culture as a function of time. One problem with the budding yeast population synchrony is that an initially synchronous culture will grow to be asynchronous and stationary very rapidly

(Boczko et al., 2010). Common methods for maintaining cell cycle synchrony in yeast typically only produce three or four synchronous cycles and afterwards induce physiological stress that could contaminate measurements (Walker, 1999, Stowers et al., 2010). One explanation for this rapid decay of cell cycle synchrony is the polarized growth and asymmetric division of the budding yeast. That is, at the time of division, the daughter cells are smaller in volume than their mothers (Woldringh et al., 1993). It is also found that the new daughter cells possess a longer cell cycle period than that of their mothers, which further compounds the difficulty to maintain the cell cycle synchrony. To improve the capability of maintaining cell cycle synchrony, there is a compelling need to develop an accurate model for cell cycle progression (Nurse, 1975, Lord and Wheals, 1980, Wheals, 1982, Jorgensen and Tyers, 2004). Because the volume growth rate of budding yeast is a direct proxy for the cell cycle progression, investigation of changes in volume during the yeast cell cycle has been an appealing research topic (Stowers et al., 2009).

The study of budding yeast cell volume growth was initiated with measurements on single cells. Bayne-Jones and Adolph (Bayne-Jones and Adolph, 1932) first investigated the growth curve of individual budding yeasts, *Saccharomyces cerevisiae,* strain F. The yeast culture was derived from a single yeast colony isolated from a commercial yeast cake and incubated at 37 ℃. The culture was then inoculated on top of a thin agar culture medium layer sitting on a glass microscope slide. The microscope with the culture slide mounted on the stage was enclosed in a small incubator at 37 ℃. When the single yeast cells were growing on the agar culture surface, the lengths and breadths of individual cells were read from the projected frames generated by the microscope. The volume of the yeast cell was calculated as:

$$Volume(V) = length(l) \times square\ of\ breath(b^2) \times \pi/6, \qquad (1.8)$$

Each new born yeast cell started as a bud bulging forth from a parent cell, enlarging in size, and finally gave rise to the production of a daughter yeast cell. The experimental results showed that the volume growth of individual yeast cells appeared in a series of waves. Each wave front corresponded to a fastest growth phase of the immature yeast. The growth ceased as the daughter matured and resumed with the formation of each new bud. After the appearance of the bud, a linear growth manner was found, and finally a declining growth rate was observed at the end of the cell cycle. The total growth in volume seemed like a sigmoid curve with lower growth rate before the bud appeared and after the daughter cell matured during each generation. The average volume increase during the yeast cell progression can be represented by a line including all the crests or troughs of the waves (Fig. 1.6).

Later, Lindegren and Haddad (Lindegren and Haddad, 1954) conducted similar measurements for individual budding yeast cells suspended in a liquid medium. They observed that the increase in volume of individual yeast cells began abruptly marked by the emergence of a bud. The bud bulged in a linear manner, and finally came to a sudden end when certain volume was achieved. During the bud growth, the volume of the parent cell stayed the same. This conclusion, an approximately sigmoid volume growth curve for individual yeast cells, was later validated by Mitchson utilizing an interference microscope (Mitchson, 1958). Hartwell and Unger (Hartwell and Unger, 1977) also observed that the parent cell changed little in volume (7%) over the budded period. Their experimental data from the time-lapse microscopic observation showed that during the budded period most of the volume increase was from the bud and very little from the parent cell, whereas both the daughter and the parent cell enlarged in volume over the course of the unbudded interval. They also concluded that the daughter yeast cell was smaller and had a longer subsequent cell cycle than its mother.

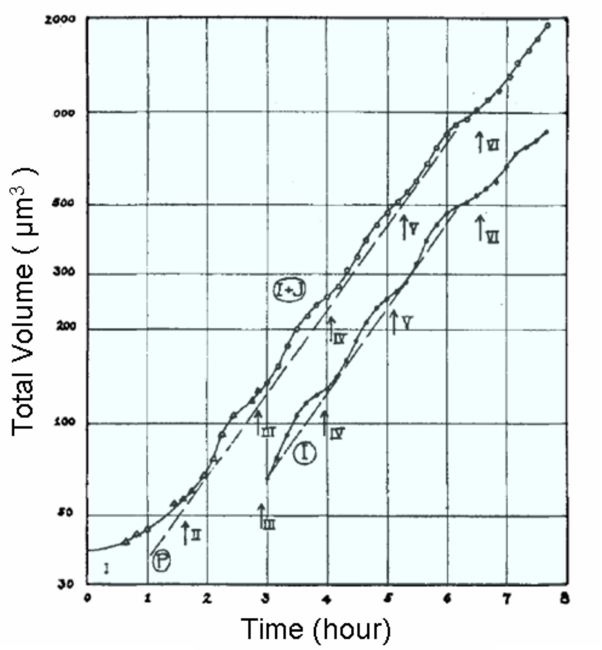

Figure 1.6: Progressions of the yeast cell in a culture at 37 ℃. At each arrow, a new generation of buds appeared. For each generation, an S-shape volume growth curve was observed (Bayne-Jones and Adolph, 1932).

Although budding yeast cells have a well defined elliptical shape, some factors such as cell rotation during the growth period may increase the measurement error resulting from the simple geometric assumption. To eliminate this geometric uncertainty, Owe Berg and Ljunggren (Owe Berg and Ljunggren, 1982) conducted measurements on a particular strain of *Saccharomyces cerevisiae* that presents a nearly exact spherical shape. As a result, the cell volume determined from the microscopic observation was independent of the cell orientation during the cell cycle. Their data indicated a linear growth curve for the budded yeast until it reached the final size, followed by a sudden stop, which was in substantial agreement with the findings by Bayne-Jones and Adolph (Bayne-Jones and Adolph, 1932).

Regarding the linear growth model for budding yeast, Woldringh and co-workers (Woldringh et al., 1993) argued for an exponential increase in volume. They applied a new method called intersection analysis to measure the volume growth of the daughter and the mother cells separately for a steady-state population. As shown in Fig. 1.7, based on the statistical data of hundreds of cells, the average volume of daughter cells increased from an initial volume of 25.9 µm^3 and reached 74.3 µm^3 at division during their first cell cycle. The average volumes of the divided mother and daughter cells were 44.2 µm^3 and 29.2 µm^3, respectively. However, we believe that it is at least equally possible to interpret their data using a piece-wise linear sigmoid growth curve with a low growth rate before the bud emerged, a fast linear growth after the bud emerged, and a reduced growth rate after the daughter matured, which is shown by the dashed red line in Fig. 1.7.

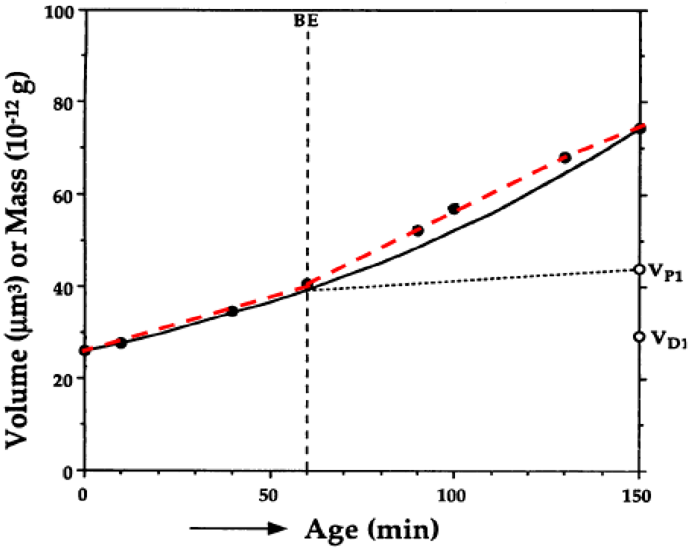

Figure 1.7: Average volume growth of daughter cells selected with the elutriator during their first cell cycle. The solid line represents an exponential volume increase curve argued by the authors (Woldringh et al., 1993) for daughter cells of an average volume of 25.9 µm^3 growing to an average volume of 74.3 µm^3 at division after 150 minutes. We believe that the dashed red line, which linearly connects the experimental data and follows a sigmoid volume growth curve, can interpret the data at least equally well.

Although the volume growth rate of individual budding yeast cells can be determined by microscopy, this method requires geometric assumptions of the yeast cell that may not be strictly valid. More complex optical systems allow for more accurate cell volume measurements. For example, cell volumes can be calculated from high quality z-stacks; however, this method is extremely data intensive and very expensive (Zadrag, et al., 2006). One convenient device that gives direct results of the cell volume is the Coulter counter, which has been widely used for clinical purposes such as monitoring blood counts and for bioprocess research such as measuring cell volume. Commercial Coulter counters have been used to measure the mean volume of bacteria and the result is in substantial agreement with that from microscopic observations (Kubitschek and Friske, 1986). However, commercial Coulter counters require that cells be suspended in a high dielectric contrast fluid such as Isoton, and hence cannot be used for live cells in a time course.

In summary, the volume growth of individual budding yeast cells follows a sigmoid curve with lower growth rate before the bud appears and after the daughter cell matures during each cell cycle. At the time of division, the daughter cells are smaller in volume than their mothers. In addition, the new-born daughter cells have a longer cell cycle than their mothers.

Cell Separation

Cell separation is a vital process in fundamental biological research as well as in clinical studies. Conventional cell separation techniques can generally be classified into two categories: centrifugation and membrane filtration (Tsutsui and Ho, 2009). Other innovative techniques, including fluorescence-activated cell sorting (FACS)

(Bonner et al., 1972), magnetically activated cell separation (MACS) (Miltenyi et al., 1990), acoustic cell filter (Trampler et al., 1994), and cell affinity chromatography (CAC) (Mandrusov et al., 1995), have also been developed as more sophisticated tools to conduct cell separation based on cell properties other than cell size. During the last fifteen years, lab-on-a-chip techniques provided unprecedented opportunities to minimize the conventional separation devices, and to realize on-chip cell separation using various novel microstructures and characteristics of laminar flow. These on-chip cell separation technologies are becoming essential parts in the revolutionary tools for point-of-care diagnostics and drug discovery on highly integrated chips (Radisic et al., 2006; Tsutsui and Ho, 2009).

Since the most widely used conventional cell separation techniques, i.e., centrifugation and membrane filtration, are based on cell sizes, a lot of microfluidic cell separation schemes are designed to separate cells by size. Clever manipulation of the well-controlled laminar flow inside microfluidic channels provides many opportunities to separate different size cells into different streams. For example, using the asymmetric bifurcation of the laminar flow around carefully-designed obstacles, cells of different sizes in the suspension media can be forced to follow different paths as they travel through the microfluidic devices and eventually be separated according to their sizes. This method has been used to separate red blood cells, white blood cells, and platelets suspended in plasma (Fig. 1.8) (Davis et al., 2006). A more straightforward method for size-based microfluidic cell separation is to create micropost arrays that are separated from each other by different distances, serving as microsieves of different sizes. For example, by designing microsieves of four different sizes (2.5 µm, 5 µm, 10 µm, and 15 µm) on a microfluidic chip, Mohamed and co-workers (Mohamed et al., 2004) successfully trapped red blood cells, white blood cells, and spike neuroblastoma based on their different sizes (Fig. 1.9). Despite the remarkable simplicity of these passive cell separation techniques without the need of applying any external forces, these techniques suffer from problems such as cell clogging in the microchannels as well as cell rupture because of the shear stress in the flow field.

In additional to these passive separation techniques, non-inertial forces have been introduced into microfluidic chips to realize more controlled cell separation. For instance, dielectrophoretic force (Li and Kaler, 2004; Cen et al., 2004; Choi and Park, 2005), optical gradient force (Grier, 2003), magnetic force (Han and Frazier, 2006), and acoustic force (Petersson et al., 2005) have all been investigated to separate cells and also improve separation performance. Based on the relevance to the research work performed in this dissertation, we will focus on introduction of the dielectrophoretic separation technique, which is an effective way to separate cells either by their sizes or by their dielectric properties.

Dielectrophoresis (DEP) arises when polarizable dielectric particles are subjected to a highly non-uniform electric field. The polarization of particles leads to an electric charge separation within the dielectric particle. In addition, the medium surrounding the particle can also be polarized to a different extent based on its polarizability. The combination of the polarization of the particle and surrounding medium gives rise to a dipole moment, which interacts with the non-uniform electric field, and generates dielectrophoretic motion in the direction along (positive DEP) or against (negative DEP) the electric field gradient, depending on the intrinsic electrical properties of the particle (Fig. 1.10). For cells, their membrane capacitance and conductance are the key factors in determining the nature of the DEP (Pohl, 1978; Jones, 1995; Morgan and Green, 2003).

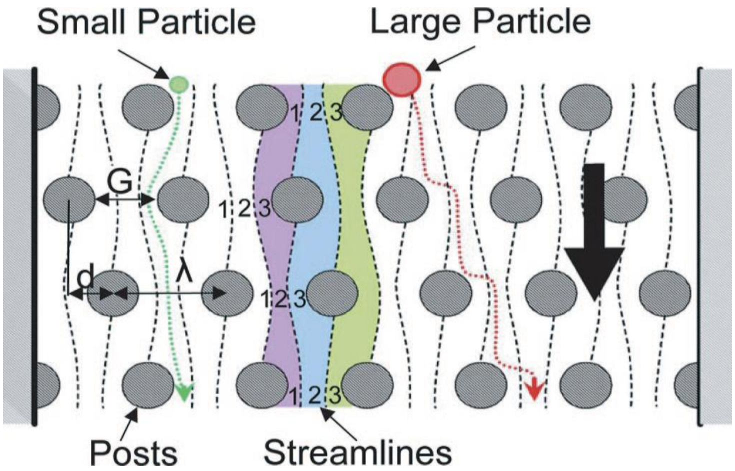

Figure 1.8: A schematic of cell separation via deterministic lateral displacement in an array of microposts. The arrangement of the microposts created a laminar flow field composed of periodic flow patterns (such as the colored region) that included three equal flux streamlines. As cells flowed through the micropost array, small cells stayed within a streamline between two dashed lines and came back to the same lateral position after every three rows, whereas large cells were forced away continuously from their original lateral positions after each row (Davis et al., 2006).

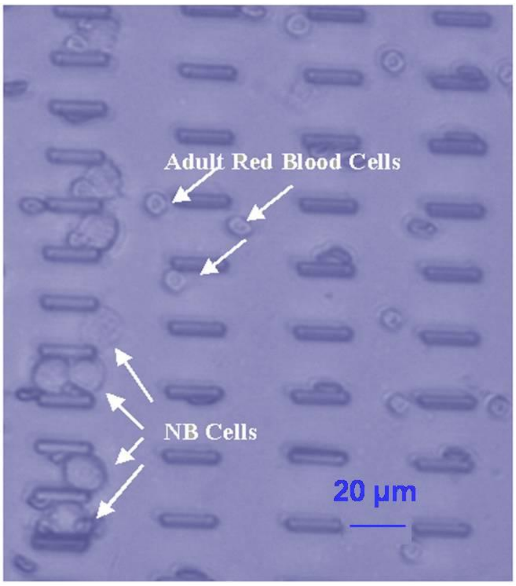

Figure 1.9: A picture of a microfiltration device that allowed red blood cells to flow freely, while spiked neuroblastoma cells were trapped at the first row of the 10 µm wide by 20 µm deep channels (Mohamed et al., 2004).

For a homogeneous, dielectric sphere of radius R and permittivity ε_2, immersed in a dielectric medium of permittivity ε_1 and exposed to an electric field $\vec{E}_0$, the expression for the effective dipole moment can be written as (Jones, 1995; Morgan and Green, 2003):

$$\vec{\rho}_{eff} = 4\pi\varepsilon_1 K_{CM} R^3 \vec{E}_0, \qquad (1.9)$$

where K_{CM} is the Clausius-Mossotti (CM) factor, which represents a measure of the effective polarization of a particle as a function of its dielectric properties and the suspension medium, as well as the frequency of the external electric field. The CM factor can be expressed as:

$$K_{CM} = \frac{\varepsilon_2^* - \varepsilon_1^*}{\varepsilon_2^* + 2\varepsilon_1^*}, \qquad (1.10)$$

where ε_1^* and ε_2^* are the complex permittivities of the medium and the particle that are related to the frequency of the time-varying (AC) electric field (ω) and their respective electric conductivities (σ). The formula for ε_1^* and ε_2^* can be written as:

$$\varepsilon_{1,2}^* = \varepsilon_{1,2} + \frac{\sigma_{1,2}}{j\omega}, \qquad (1.11)$$

If a lossless dielectric particle is subjected to an AC electric field, the induced dipole moment could be collinear or antiparallel to the electric filed, $\vec{E}_0$, depending on the relative magnitude of ε_1 and ε_2.

Given the expression of the effective dipole moment, $\vec{\rho}_{eff}$, the dielectrophoretic force on a spherical particle can be written as:

$$\vec{F}_{DEP} = \vec{\rho}_{eff} \times \nabla\vec{E}_0 = 2\pi\varepsilon_1 K_{CM} R^3 \nabla\left|\vec{E}_0\right|^2, \qquad (1.12)$$

Eqn. (1.12) indicates that the magnitude of the DEP force is proportional to the particle volume and the dielectric permittivity of the suspending medium. The direction of the DEP force is the same as the gradient of the square of the magnitude of the electric field intensity, $\nabla\left|\vec{E}_0\right|^2$.

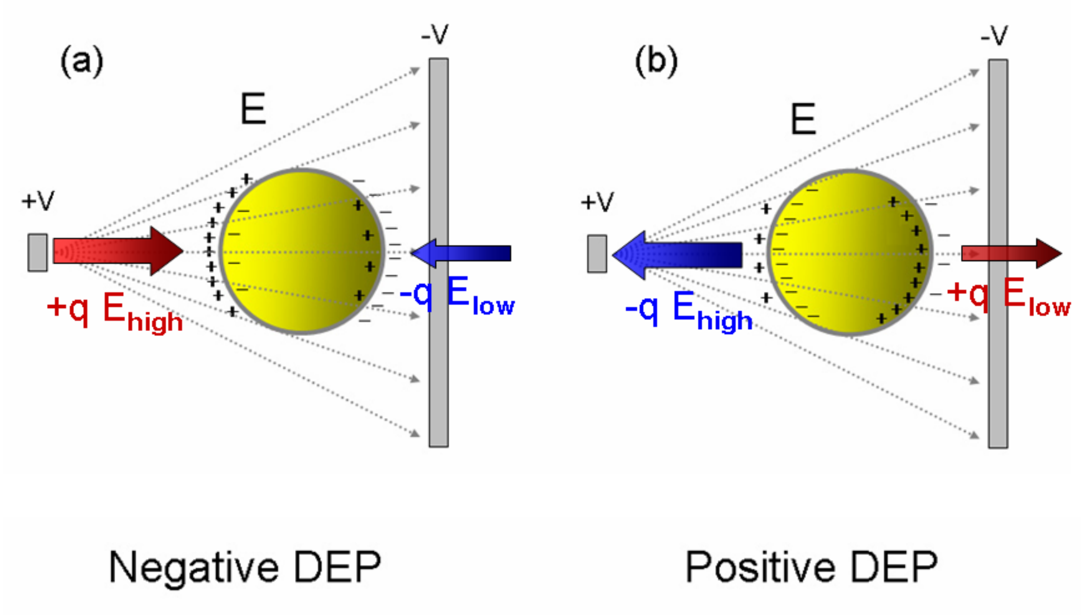

Negative DEP

Positive DEP

Figure 1.10: A schematic illustration of the dielectrophoretic motion of a spherical particle. (a) The suspension medium is more polarizable than the particle, which results in a repulsive force away from the local electric field intensity maxima, and is called negative DEP; (b) The particle is more polarizable than the suspension medium, giving rise to an attraction force towards the local electric field intensity maxima, and is called positive DEP.

DEP force is usually weak and only effective to affect the dynamic behavior of small particles in the diameter range from 1 to 1000 µm. Particles experience dielectrophoretic force if the electric field is non-uniform, no matter whether the electric field is AC or DC in nature. Therefore, both AC and DC DEP have been used for cell separation. AC DEP cell separation is based on the different polarity (positive or negative) responses of cells around a cross-over frequency under a non-uniform, AC electric field (Morgan and Green, 2003). In this technique, arrays of metal microelectrodes are fabricated on the microfluidic chip to generate a highly non-uniform AC electric field at relatively low voltages. For example, Doh and Cho (Doh and Cho, 2005) demonstrated a high-throughput microfluidic device to continuously separate live and dead yeast cells according to their different DEP responses. The DEP force repels live cells away from the central streamline (positive DEP) while collects the dead cells in the central streamline (negative DEP) (Fig. 1.11). Similar work has been done by other groups (Becker et al., 1995; Li and Kaler, 2004) to sort different cells based on their different polarization responses to the AC electric field.

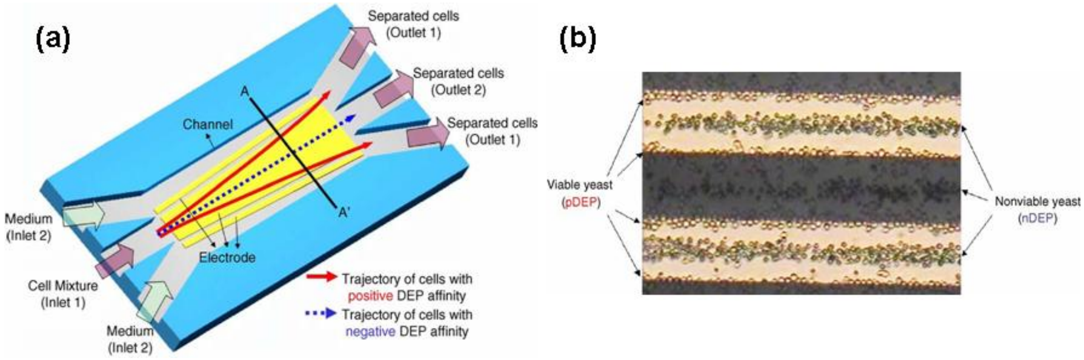

Figure 1.11: (a) A schematic of the AC-DEP separation device; (b) The microscopic image showing the DEP separation of the live and dead yeast cells subjected to an AC electric field (Doh and Cho, 2005).

In addition to the polarity based cell separation, since dielectrophoretic force is proportional to the particle volume, as shown in Eqn. (1.12), AC DEP can also separate cells based on their sizes (Choi and Park, 2005; Hu et al., 2005). For example, Choi and Park (Choi and Park, 2005) fabricated a size-based dielectrophoretic separation chip using an array of trapezoidal electrodes that were able to generate an asymmetric electric field gradient along the direction perpendicular to the laminar flow direction. The chip was used to separate polystyrene beads of different sizes since the trajectory of dielectric beads was determined by a combined effect of the AC DEP force and the hydrodynamic drag force. Larger polystyrene beads experienced stronger negative AC DEP force and were defected more than the smaller ones in the transverse direction of the laminar flow field (Fig. 1.12). This microfluidic device efficiently separated particles of 6 μm and 15 μm and gained a purity of 96.8 ±0.6% and 99.5 ±0.5%, respectively, which had been verified using an inverted fluorescence microscope.

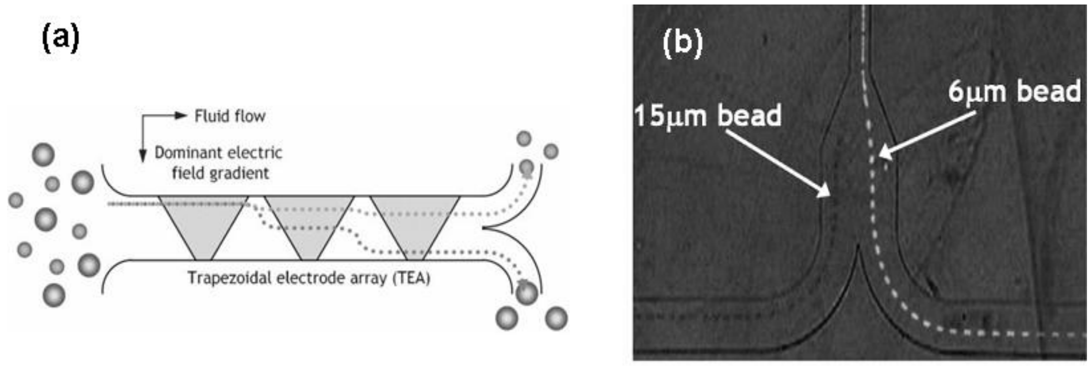

Figure 1.12: (a) A schematic illustration of a trapezoidal electrode array (TEA) for size-based AC DEP beads separation. An AC voltage enabled the TEA to generate an asymmetric electric field. Particles subjected to this non-uniform AC electric field experienced negative DEP force and were levitated to different lateral positions according to their size; (b) Superimposed trajectories of the 6 μm and 15 μm diameter spherical particles separated by negative DEP (Choi and Park, 2005).

In addition to AC DEP, DC DEP has also been used in microfluidic chips for cell separation (Kang et al., 2006; Kang et al., 2008). A local non-uniform DC electric field around an insulating post can be generated from a large DC electric bias applied to the inlet and outlet of the microfluidic device (Sun et al., 2009). This local non-uniform electric field can be used to induce different transverse DC DEP migration of particles or cells depending on their sizes. The large electric potential difference between the inlet and the outlet of the microfluidic device also introduces an electroosmotic flow in the microchannel to facilitate the cell motion along the microchannel. In a DC electric field, the cell membrane blocks the DC current so that the cell behaves just like an insulating particle with $\varepsilon_2 = 0$ (Jones, 1995). Therefore, Eqn. (1.10) can be simplified as:

$$K_{CM} = \frac{\varepsilon_2 - \varepsilon_1}{\varepsilon_2 + 2\varepsilon_1} = -\frac{1}{2}, \tag{1.13}$$

Eqn. (1.12) can then be reduced to:

$$\vec{F}_{DEP} = -\pi\varepsilon_1 R^3 \nabla \left|\vec{E}_0\right|^2, \tag{1.14}$$

Note that under a DC electric field, the DEP force is proportional to the cell volume as the electric field gradient is constant over time.

Cummings and Singh (Cummings and Singh, 2003) first applied DC DEP to realize in-flow particle filtration and concentration through patterning insulating micropost arrays in the microfluidic device. Under an applied DC bias, an electrokinetic flow of the particles due to the combined effects of electrophoretic migration and electroosmotic flow was induced. The dielectrophoretic traps were formed near the insulating posts where the DEP force dominated over the electrokinetic flow. Barbulovic-Nad and collaborators (Barbulovic-Nad et al., 2006) created an insulating structure in the microchannel using an oil droplet, where a locally non-uniform DC electric field was applied to introduce DC DEP to separate microparticles (Fig 1.13).

More recently, Kang and colleagues (Kang et al., 2008) fabricated an insulating structure with a PDMS block in their design, which generated a local non-uniform electric field for DC DEP cell separation. As discussed above, since the magnitude of the DC DEP is proportional to the cell size, the trajectories of different size cells will be discriminated. Therefore, cells can be separated into different streams after they pass through the PDMS hurdle. This DC DEP scheme was applied to separate fixed white blood cells from the lysis debris (Fig 1.14). Similarly, Parikesit and co-workers (Parikesit et al., 2008) developed a microfluidic device with sub-micron deep channels to separate DNA macromolecules according to their sizes using DC DEP.

It is worth noting that most published microfluidic cell separation techniques focused on demonstration of the separation principle; and therefore, the experiments were usually performed with a mixture of particles or cells of relatively large size difference. Many experimental results only show superimposed images of different streams composed of large and small particles or cells over a short period of time. It is, therefore, difficult to determine the separation performance over a long time period. As pointed out in a review article (Tsutsui and Ho, 2009), careful characterization of separation performance and optimization of the separation scheme based on the characterization are necessary in future studies.

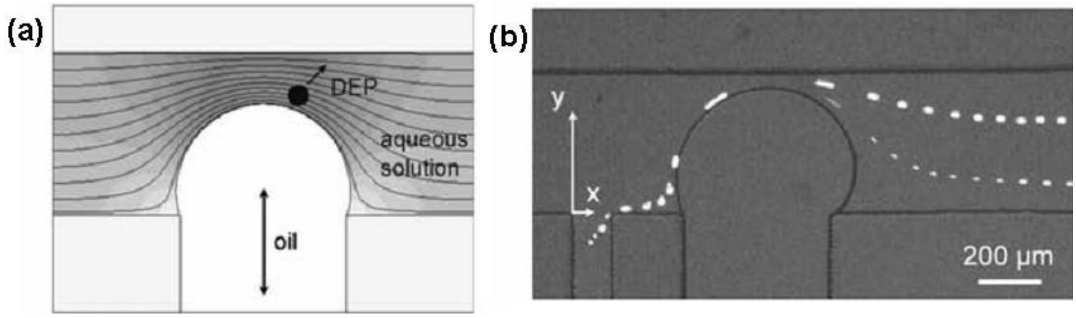

Figure 1.13: (a) A schematic illustration of an insulating structure created by an oil droplet and the electric field strength contours near the oil droplet to induce DC DEP on a particle; (b) Trajectories of the 5.7 μm and 15.7 μm diameter spherical particles separate by the DC DEP (Barbulovic-Nad et al., 2006).

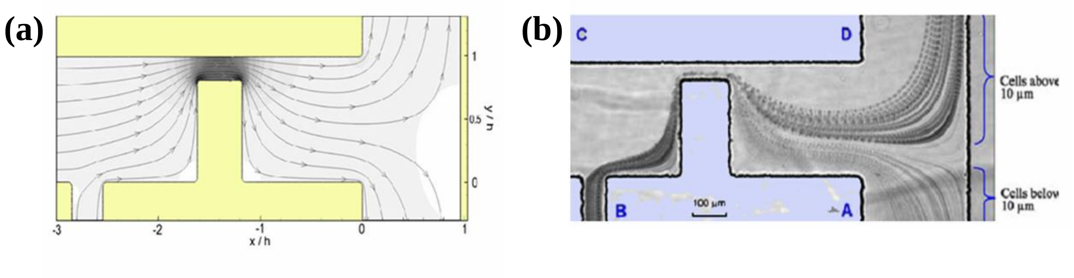

Figure 1.14: (a) Simulation results showing the distribution of the electric field and contours of the electric field strength inside the microfluidic channels; (b) The trajectories of the white blood cells and the lysis debris. The mixture of two different cells was fed into the separation regime through branch B. The large white blood cells went up to branch D while the small debris went down to branch A (Kang et al., 2008).

CHAPTER II

YEAST VOLUME GROWTH MEASUREMENTS USING THE MOSFET-BASED MICROFLUIDIC COULTER COUNTER

This chapter describes measurements of the volume growth rate of ten individual budding yeast cells using a recently developed MOSFET-based microfluidic Coulter counter. The MOSFET-based microfluidic Coulter counter is very sensitive, provides signals that are immune from the baseline drift, and can work with cell culture media of complex composition. These desirable features allow us to measure directly the volume growth rate of the budding yeast LHY3865, a strain of *Saccharomyces cerevisiae*, in YNB culture media over a whole cell cycle. The measured volume growth curve appears sigmoidal with individual variation bounded by 1.38 μm^3 root mean square deviation (RMSD). Analysis of the data indicates that even though both piecewise linear and exponential models can fit the global growth profile equally well, the data strongly support local exponential growth phenomena. Accurate volume growth rate measurements are important for applications in systems biology where quantitative parameters are required for related modeling and simulation.

Motivation

Bioassays are typically performed on ensembles of cells. Therefore the assay results usually depend crucially on the state of cells relative to one another. If the cells in an ensemble have a multimodal distribution with respect to some variable, then measurements that depend on that variable are confounded by averaging. The cell cycle has been shown to provide an example that is of critical importance when studying regulatory networks in system biology (Stowers and Boczko, 2007). One approach to obtain more meaningful results from ensemble-based assays is to prepare a population of cells that maintain the cell cycle synchrony. A synchronous population has a unimodal population density that moves through the cell cycle as a solution and is periodic in time (Boczko et al., 2010). For budding yeast, because of the inherent asymmetry involved in the division of the yeast cells, prepared population synchrony decays very rapidly (Walker, 1999; Stowers et al., 2010; Nurse, 1975). However, simulations have shown that a continuous volume filtration strategy can extend prepared synchrony by an order of magnitude (Stowers et al., 2009). The calculation of the design parameter and the volume filtration cutoffs required accurate models of individual yeast growth rates as a function of the cell cycle.

We choose to study the budding yeast *Saccharomyces cerevisiae* because it is a versatile, well studied, and widely used eukaryotic model organism. The budding yeast volume growth rate has been traditionally measured using various optical approaches, which either require geometric assumptions of cells or need to process extremely large amount of data. The optical microscopy measurement of the volume growth rate of individual budding yeast cells has revealed a sigmoid growth curve (Mitchison, 2003; Hartwell and Unger, 1977). However, researchers are still debating about the precise functional representation of the volume growth curve with polynomial and exponential functions as two contenders. In this chapter, we develop a new sensing scheme based on the newly developed MOSFET-based microfluidic Coulter counter to measure the volume growth rate of multiple budding yeast cells for accurate functions describing the volume growth of budding yeast.

Experimental Methods

Yeast Cell Preparation – The Baby Machine

S.cerevisiae LYH3865 strain budding yeast (Stowers and Boczko, 2007) was cultured in YNB media containing 2% glucose and 0.2% glutamine in this study. A baby machine was used to produce populations of newborn daughter yeast cells (Helmstetter, 1991). The baby machine consisted of a Millipore nitrocellulose porous membrane coated with poly-d-lysine. The membrane was supported by a stainless steel mesh sandwiched between two plastic funnels approximately 1 inch in diameter. A 2 mL active yeast culture was loaded onto the porous membrane and the yeast cells were adhered to the coated poly-d-lysine. The baby machine was then inverted and warm media was perfused through the porous membrane at a rate of 1 mL/sec. As the yeast cells reproduced, the mothers stayed attached to the membrane while the daughters dropped and were collected in the media. The baby machine effluent was then diluted appropriately to contain about 100 cells/mL and placed in an incubator for two hours. Typically, when yeast cells are introduced into fresh media they experience a lag phase, during which the yeast cells condition their media and then resume growth (Chen et al., 2004c; Brejning et al., 2005). During this incubation step the mean diameter of the daughter cells may expand slightly, and finally reaches ~3.5 μm. The volume growth during the incubation period is slow and follows the trend as we measured before the bud emerges. Therefore, measurement starting from the end of the 2 hour incubation period still captures all essential volume growth characteristics that are of interest without losing important information.

The MOSFET-Based Microfluidic Coulter Counter

The volume growth rate of single budding yeast was measured with a recently-developed MOSFET-based microfluidic Coulter counter (Xu et al., 2007; Sridhar et al., 2008). As shown in Fig. 2.1, instead of the common two-terminal layout of Coulter counters, we have constructed a three-terminal PDMS microfluidic circuit bonded with a glass substrate. The horizontal fluidic circuit was composed of two large microchannels sandwiching a small sensing channel (15 μm×15 μm×50 μm for width×depth×length), and the vertical microchannel was connected to the gate of a commercial MOSFET (2N7000 N-channel FET, Fairchild Semiconductor) to detect the change of the electric potential at the end of the sensing channel, which is related to the resistance modulation of the sensing channel upon the translocation of an individual budding yeast cell. An electrical bias was applied across the horizontal channels by two DC power supplies (Agilent E-3612A, Agilent Technologies) to induce electroosmotic flow to drive yeast cells through the sensing aperture. We used two power supplies to adjust the MOSFET gate potential to ensure that it works in the sub-threshold regime. An additional power supply (Agilent E-3617A, Agilent Technologies) was used to provide a constant source-drain bias to induce the MOSFET drain current, which was measured by a current preamplifier (Keithley 428, Keithley Instruments Inc.). The measured drain current was first passed through a low-pass filter (SR 560, Stanford Research Systems) with a cut-off frequency of 30 Hz before it was fed into the digital data acquisition system. The fluidic and MOSFET circuits were commonly grounded.

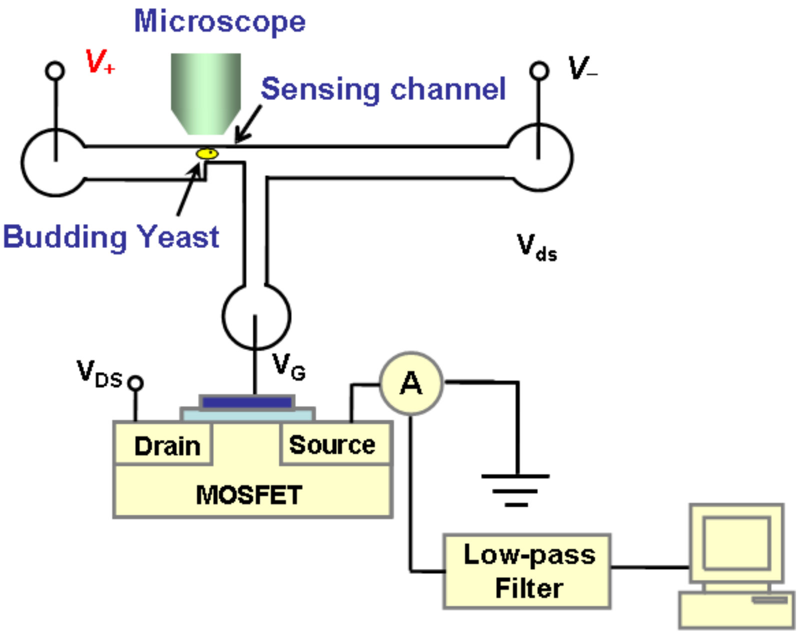

Figure 2.1: A schematic of the measurement setup with the MOSFET-based microfluidic Coulter counter (not to scale). The fluidic and MOSFET circuits are commonly grounded.

In the yeast volume growth rate measurement, the YNB media were first loaded into the three wells of the microfluidic device. The device temperature, monitored with a thermocouple (800004, Sper Scientific) every 15 min, was held constant at 29±1°C by radiation heating from a lamp. A small portion of daughter cells from the incubator was then loaded into the device and one cell was selected and moved back and forth through the sensing channel for volume growth rate measurement over ~2.5 hours. The cell motion was realized with electroosmotic flow induced by an electric bias applied across the horizontal channel, as shown in Fig. 2.2. The PDMS-glass microchannel has a negative zeta potential, which will lead to an electroosmotic flow under the applied electric bias. If the electric field is reversed, the direction of the flow is also altered. In this manner, the selected cell can be moved back and forth by switching the polarity of the applied electric bias. Each time the yeast cell was translocated through the sensing channel from the upstream to the downstream, the MOSFET drain current modulation was recorded. The resistance modulation of the sensing channel because of the translocation of the yeast cell led to a modulation of the MOSFET's gate potential, and hence, a pulse of the MOSFET drain current.

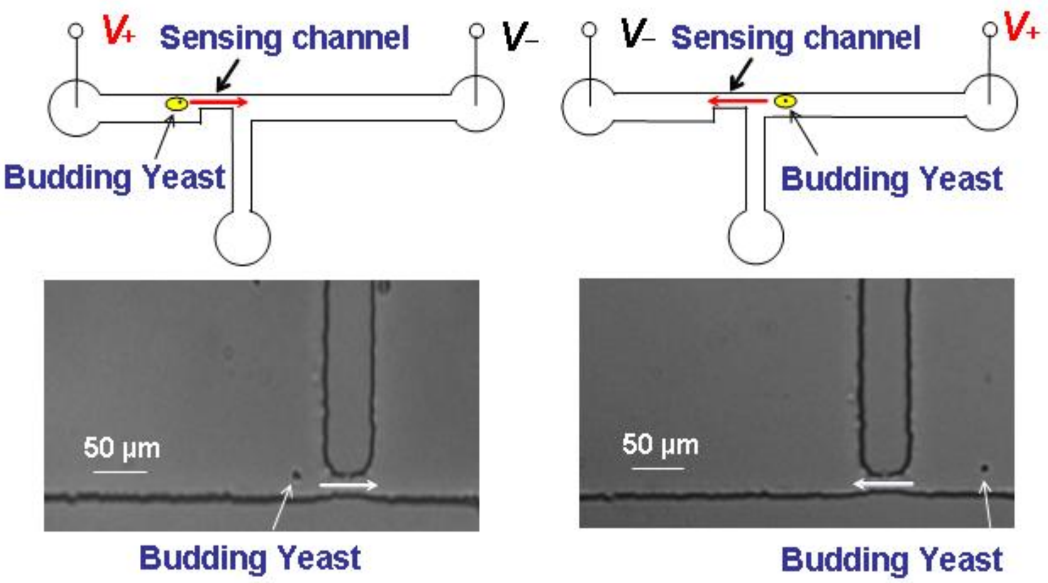

Figure 2.2: Schematic and microscopic images of a single yeast cell moving back and forth through the sensing channel by switching the applied electrical voltage. (Left panel) The yeast cell moves from the upstream to the downstream; (Right panel) The yeast cell moves back from the downstream to the upstream.

Theoretical analysis of the MOSFET drain current modulation while the MOSFET is operating in the sub-threshold regime is given by (Sridhar et al., 2008):

$$\frac{\Delta I_D}{I_D} \approx \left(\frac{q}{kT} - \frac{1}{2V_G}\right)(V_G - V_-)\left(\frac{R}{R_t}\right)\frac{\Delta R}{R}, \tag{2.1}$$

where I_D and ΔI_D are the MOSFET drain current and its modulation, respectively; q, k, and T are the elementary electronic charge, the Boltzmann constant, and the temperature, respectively; V_G and V_- are the MOSFET gate potential and the potential applied to the downstream well, respectively; R, ΔR, and R_t are the resistance of the sensing channel, its modulation, and the total resistance of the three horizontal channels, respectively. Based on Eqn. (2.1), the percentage modulation of the MOSFET drain current is proportional to the percentage modulation of the sensing channel resistance for constant V_G and V_-. Since q/kT is about 40 V^{-1} at room temperature and other factors in front of the sensing channel resistance modulation is on the order of unity, the percentage modulation of the MOSFET drain current can be 30-50 times larger than the percentage modulation of the resistance. This amplified percentage modulation leads to a pulse easily detectable from the baseline, which enhances the sensitivity of the device to extract small resistance modulation from the translocation of small particles.

Under a DC electric field, the intact cell membrane of yeast cells is composed of lipids and proteins that would block ion transport, and hence, the cells behave like a good insulator (Jones 1995; Lapizco-Encinas et al., 2004). If the yeast cell is regarded as a sphere and non-conductive relative to the highly conductive culture media, the resistance modulation to the baseline can be written as (Xu et al., 2007):

$$\frac{\Delta R}{R} = \frac{1}{4}\frac{\pi d^3}{LWD}, \qquad (2.2)$$

where d is the yeast cell diameter, L, W, D are the length, width and depth of the sensing channel, respectively. The above equation indicates that the resistance modulation of the sensing channel is directly proportional to the volume ratio of the cell to the sensing channel. Note that this expression is accurate only if the diameter of the sphere is much smaller than the size of the sensing aperture. In our case, because of the enhanced sensitivity, we can use relatively large channel to detect small cells, and the cross-sectional area ratio of the yeast cell to the sensing channel is less than 0.085. It has been shown that the upper limit of the cross-sectional area ratio for a linear response is about 0.16 (Sridhar et al., 2008), which is still much larger than that for the largest yeast cell used in our measurements.

It is worth noting that the shape of a budding yeast cell is not strictly spherical, but can be described more appropriately as an ellipsoid. However, this only leads to very small measurement error. For example, it has been shown that compared to a sphere of the same volume, an ellipsoid of revolution with an axial ratio of 4 to 1 would give rise to a pulse difference of merely 3% (Kubitschek, 1969). Given the fact that budding yeast usually have an axial ratio much smaller than 4:1, the error from non-spherical geometry will be minimal. A budded yeast cell presents a lopsided peanut shape, which is neither spherical nor elliptical. Fortunately, both our previous study and results in the literature show that for two microparticles of the same size stuck together translocated through the sensing aperture of a Coulter counter, the resulted pulse amplitude would be doubled. This indicates that even for a lopsided peanut shape particle, the resistance modulation is still very closely proportional to that of the volume ratio, as long as the cross-sectional area of the particle is much smaller than that of the sensing aperture (Sridhar et al., 2008), which is indeed the case in our measurements.

The Effect of the Baseline MOSFET Drain Current Drift

Eqn. (2.1) and Eqn. (2.2) indicate that the percentage modulation of the MOSFET drain current is linearly proportional to the volume ratio of the sensing object to the sensing channel, as experimentally confirmed using polystyrene beads (Sridhar et al., 2008). One more problem in the experiment is that the baseline MOSFET drain current could drift over time in the experiment, even though all the potentials supplied to the fluidic circuit and the MOSFET are kept constant. Fortunately, Eqn. (2.1) indicates that the percentage modulation of the MOSFET drain current is not a function of the baseline drain current if the MOSFET is working in its sub-threshold regime and V_G and V_- are held constant. To verify this, we conducted a characterization run in which we moved a polystyrene bead back and forth through the sensing channel 10 times during a period of a little over an hour and recorded the corresponding MOSFET drain current modulation. The characterization results show that indeed, the percentage modulation of the MOSFET drain current is not a function of the baseline MOSFET drain current, as shown in Fig. 2.3.

The average percentage modulation of the MOSFET drain current for the polystyrene bead is 12.17% with a standard deviation of 0.22%, considering the measurement uncertainty, the measured modulation can be regarded as the same. To extract the drain current modulation from the drifting baseline MOSFET drain current, a linear fit of the MOSFET drain current was first constructed over a short time period including the modulation event and the modulation was traced and extracted using a MATLAB code (MATLAB®).

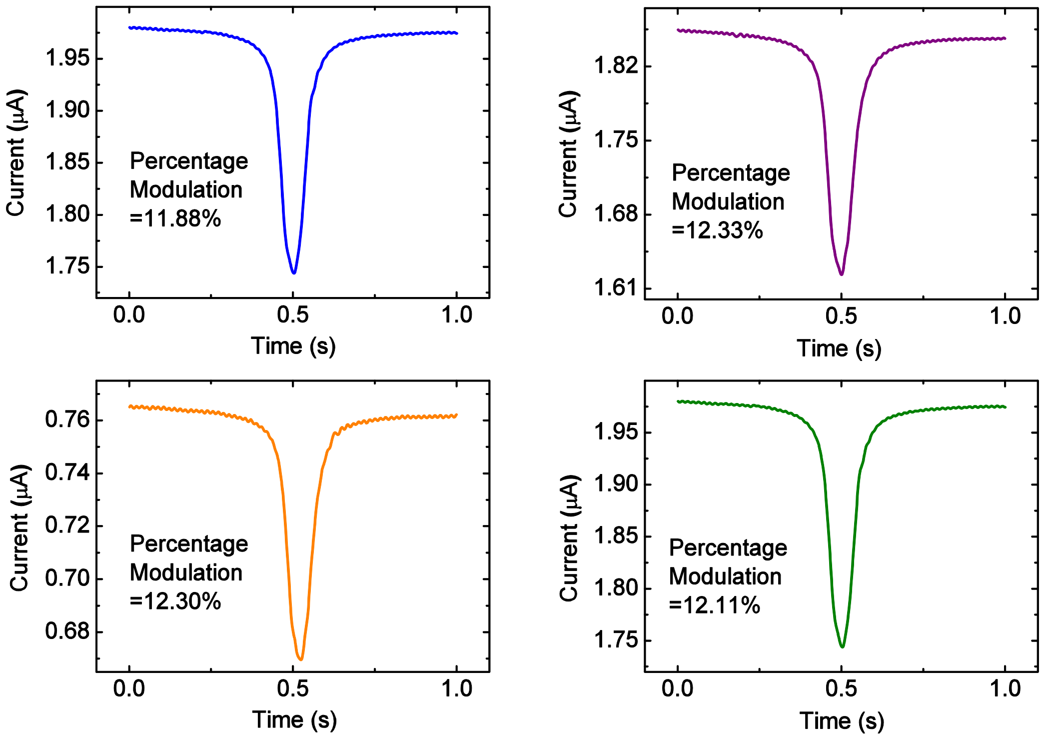

Figure 2.3: Calibration results of the MOSFET drain current modulation as a 4.84 μm in diameter polystyrene bead moves back and forth through the sensing channel.

Calibration of the Size Measurement with the Microfluidic Coulter Counter

It is expected that there exist some slight geometrical variations of the sensing microchannel, because of various factors in the fabrication process such as the spinning speed, exposure time, baking conditions, etc. To remove the measurement error caused by the geometrical variations, the performance of each device was calibrated with more than a hundred of 4.84 μm diameter polystyrene beads (PS05N, Bangs Laboratories, Inc.) after each measurement of the budding yeast growth rate. The mean diameter of a total of 100 microbeads was taken as 4.84 μm, according to the quoted size of the microbeads from the manufacturer. The standard deviation of the 100 microbeads as measured with the MOSFET-based microfluidic Coulter counter ranged from 0.2 μm to 0.3 μm, which was less than half of the nominal value (0.59 μm) from the manufacturer. To further verify that the mean diameter of the microbeads is 4.84 μm, the diameters of a total of 102 microbeads have been measured with a scanning electron microscope (SEM). The mean diameter of the microbeads was determined as 4.80 μm, which was in good agreement with the quoted value from the manufacturer. The standard deviation of the 102 microbeads was calculated as $\sigma = 0.15\ \mu m$, which was again less than half of the nominal value (0.59 μm). The volume of the measured yeast cell was then calculated based on the percentage modulation of the MOSFET drain current from the translocation of the polystyrene beads. We believe that this calibration process could help to remove the systematic error of the volume growth measurement.

Measurement Uncertainty

Several factors can contribute to the measurement uncertainty. One major factor is from the calibration of the microfluidic Coulter counter with the 100 microbeads. Taking manufacture specified standard deviation of 0.59 μm, the uncertainty of the mean size of the 100 beads is then $0.59 \times 2 \big/ \sqrt{100} = 0.118\,\mu m$ (Coleman and Steele, 1999). This corresponds to a volume uncertainty of $0.118 \times 3 / 4.84 = 7.31\%$ with respect to the manufacture specified average bead size; and therefore, leads to the same uncertainty in the calculated yeast cell volume. This uncertainty source is from the calibration process because of the non-uniformity of the polystyrene beads. It only leads to a systematic error in the measurement results but does not affect the trend of the yeast growth curve, which is one major concern in the current research. More accurate measurements with less uncertainty can be achieved by using beads of more uniform size distribution for calibration. Another uncertainty source is the data extraction from the linear fit of the drifting baseline MOSFET drain current. The ten repetitive measurements of the same polystyrene bead present a standard deviation of 0.22%.

Following the standard uncertainty analysis approach (Coleman and Steele, 1999), within 95% confidence, the uncertainty from this source is 2.262 times the standard deviation, which leads to an uncertainty of 0.498%. In addition, as indicated in the literature and discussed above, for Coulter counters, the uncertainty from the non-spherical geometry only leads to a deviation of less than 3%. The standard uncertainty of the volume growth rate measurement combining these uncertainties can then be calculated as $\sqrt{(7.31\%)^2 + (0.498\%)^2 + (3\%)^2} = 7.92\%$.

Effects of the Electric Field

A complete understanding of the effects of the electric field on cell growth is not achieved yet but it is known that the external electric field affects cell growth because it can generate stress on the cell membrane, reorganize the membrane components, and even kill the cell (Crombie et al., 1990; Jaffe and Poo, 1979; Ryan et al., 1988). The interaction between the applied electric field and the cell occurs through both direct cell and electric field interactions and the electric field induced Joule heating effect (Voldman, 2006). The imposed transmembrane potential induced by an external DC electric field across the membrane of a spherical cell in suspension can be approximately evaluated as (Grosse and Schwan, 1992):

$$|\Delta U| = 1.5\left|\vec{E}\right|R, \tag{2.3}$$

where $\left|\vec{E}\right|$ denotes the magnitude of the external electric field and R is the cell radius.

Besides the imposed transmembrane potential, cells generally maintain a negative endogenous transmembrane potential due to the existing electric field at the cell membrane. For fungi such as budding yeast, the endogenous potential ranges from -120 to -250 mV (Anderson et al, 1992).

In our measurements, the maximum electric field is inside the small sensing channel with a strength of 122.6 V/cm, whereas the minimum electric field of 2.3 V/cm is within the upstream microchannel. If we assume that the yeast cells are spheres of ~ 4 μm in diameter, the highest imposed transmembrane potential is only 36.77 mV while the cell traverses the sensing channel. In addition, the yeast translocates the sensing channel within a time period of ~0.2 s. The relatively low imposed transmembrane potential and the short time period for the yeast to experience this potential helps to reduce the effects of the electric field on the cell growth.

The Joule heating effect only leads to a maximum temperature rise of about 0.2°C, based on a conservative estimation. The microfluidic device was made by bonding PDMS with a glass substrate, and a significant portion of the heat produced from Joule heating can be transferred away through the glass substrate. Moreover, even we assume that the PDMS and glass structure is a perfect insulator, the maximum temperature rise during the short measurement step is only about ~0.2°C, from the analysis as follows. This indicates that the Joule heating effects are negligible because the electric field is applied only for a short time period (~1 minute) during the measurement step every 15 to 20 minutes.

The total applied voltage across the whole device is 7.2 V and the total resistance of the horizontal channel is 1.5×10^7 Ω. Assuming each time the voltage is applied for 1 minute, the total energy dissipated in the microfluidic circuit is then

$$\frac{7.2^2\times60}{1.5\times10^7}=2\times10^{-4}\ J, \qquad (2.4)$$

The total amount of culture media in the channel and the wells is about 7.5×10^{-5} kg assuming that the density of the culture media is the same as that of water. Using the simple energy balance, assuming that no heat is transferred through the PDMS or glass, the temperature rise can be calculated as

$$\frac{2\times10^{-4}}{4180\times7.5\times10^{-5}}=6\times10^{-4}\ ^{\circ}C, \tag{2.5}$$

Therefore, the temperature rise in the wells and the large channels are negligible, which can also be inferred from the fact that the electric field in the upstream channels (2.3 V/cm) and downstream channel (12.3 V/cm) are much smaller than that in the small sensing channel. Any significant temperature rise must be in the small sensing channel with a large electric field of 122.6 V/cm. To quantitatively evaluate this temperature rise, we need to solve the energy balance equation that describes the generation and dissipation of heat, which can be written as (Landau and Lifshitz, 1959; Ramos et al., 1998):

$$\rho_m c_p \bar{v}\cdot\nabla T+\ \rho_m c_p\frac{\partial T}{\partial t}=k\nabla^2\mathrm{T}+\ \sigma\left|\vec{E}\right|^2, \tag{2.6}$$

where $\bar{v}$ is the velocity of the electroosmotic flow inside the sensing channel, T is the temperature, ρ_m is the density, c_p is the specific heat, k is the thermal conductivity, and σ is the electrical conductivity of the medium.

Again, to be conservative, the PDMS and the glass are assumed to be perfect insulators without any heat loss through them. Assuming that after certain time period, the temperature field reaches steady state, so the transient term $\rho_m c_p\frac{\partial T}{\partial t}$ can be neglected. This is a conservative assumption since in the initial transient period, the media temperature is lower than that it achieves after reaching steady state. The velocity of the media in the sensing channel can be estimated from the duration of the resistive pulse when the yeast cell translocates through the sensing channel as $\bar{v}=170\ \mu m/s$. The electrical conductivity of the yeast culture media, σ, is measured with a conductivity meter (Eutech Instruments) as 0.17 S/m. The thermophysical properties of media are assumed to be similar to those of water as: $\rho_m = 1 \times 10^3\ kg\ m^{-3}$, $k = 0.6\, J\ m^{-1}\ s^{-1}\ \ K^{-1}$ and $c_p = 4.18\ \times 10^3\, J\ kg^{-1}\ \ K^{-1}$.

The above equation has been solved using a MATLAB code (MATLAB®) following the approach of Xuan et al. (Xuan et al., 2004; Erickson et al., 2003). We calculated the temperature rise of a channel up to 100 μm long, which gives a maximum temperature rise of $\nabla T = 0.2$ ℃, as shown in Fig. 2.4, occurring at the end of the channel. Considering the fact that our sensing channel is only 50 μm long, the temperature rise should be even smaller. We believe that this temperature rise due to Joule heating is not important because it is smaller than the natural temperature variation (1 ℃) for cells (Voldman, 2006).

Because the electric field is applied only intermittently and the small sensing channel is short and connected to large channels at the up and down stream, this conservative analysis indicates that the Joule heating effect is not important in the measurement.

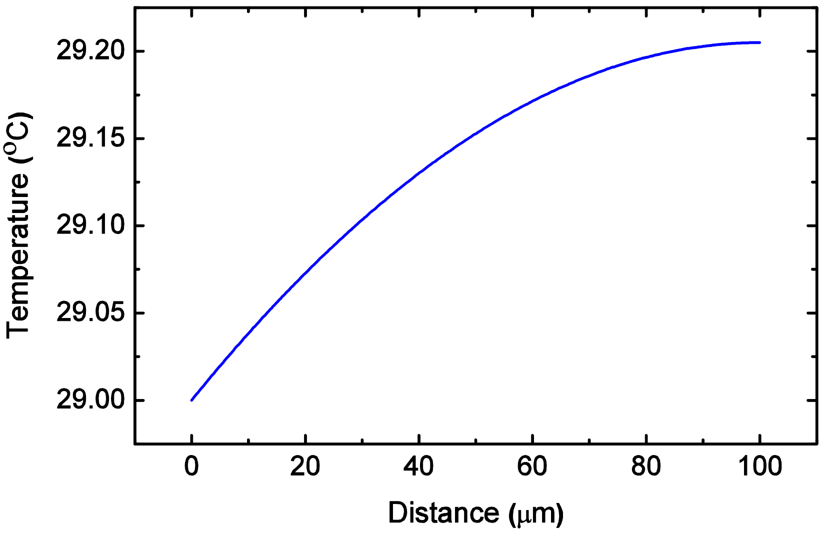

Figure 2.4: Simulated temperature rise in the small sensing channel. The simulation is based on an upstream temperature of 29°C.

Results and Discussions

Experimental Results

Fig. 2.5 shows the recorded MOSFET drain current as a function of time when a budding yeast cell was translocated through the sensing aperture at different times in one cell cycle. Each translocation event corresponds to one MOSFET drain-current modulation and the percentage modulation of the MOSFET drain current increases over time, because of the increasing yeast cell volume as the cell grows in the microfluidic device. Fig. 2.6 plots the volume growth profile of ten different individual budding yeast cells, whose volume increases from 22.7-24.3 μm^3 to 37.9-42.7 μm^3. The initial volume dispersion may be attributed to a combination of measurement uncertainty and inherent population variation. The volume of daughters eluted from the baby machine (a bud scar analysis confirms that the population comprises 99% daughters) are not identical (Helmstetter, 1991) and display a narrow distribution.

Fig. 2.6 depicts the volume growth curves for ten individual budding yeast cells, in which four curves contain 9 data points, while the other six curves contain 10 data points. The time at which the first measurement is conducted inside the microfluidic device is defined as t = 0. The average interval time step between each measurement is around 15 min. This interval is selected based on two considerations: (1) to minimize the effects of the electric field; and (2) to take one measurement while the cell volume growth is not exceeding 10%. A simple formula based on an exponential upper bound was used to compute the time step. For instance, if the growth rate is assumed to be 0.62% per minute (Brewer et al., 1984), then sampling every h minutes $h < 1000/6.2 \times \ln(1.1) \approx 15\ \mathrm{min}$ will suffice.

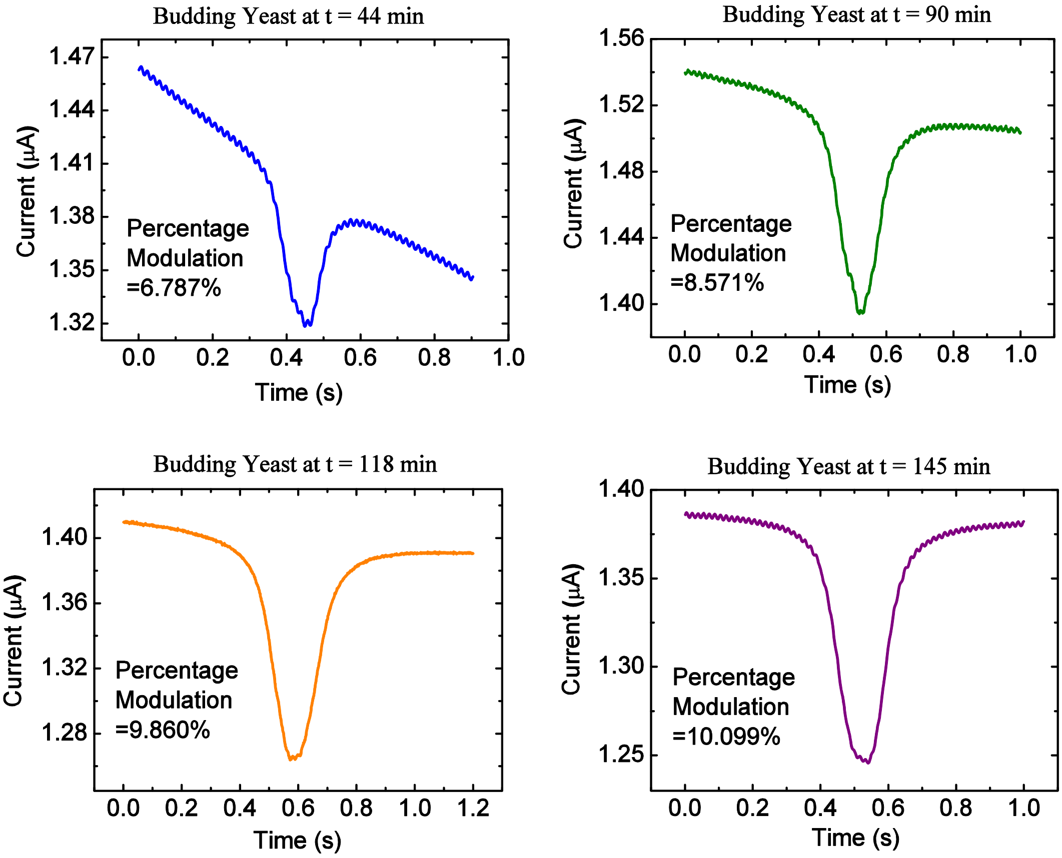

Figure 2.5: Drain current of the MOSFET measured for a single yeast cell at different time points.

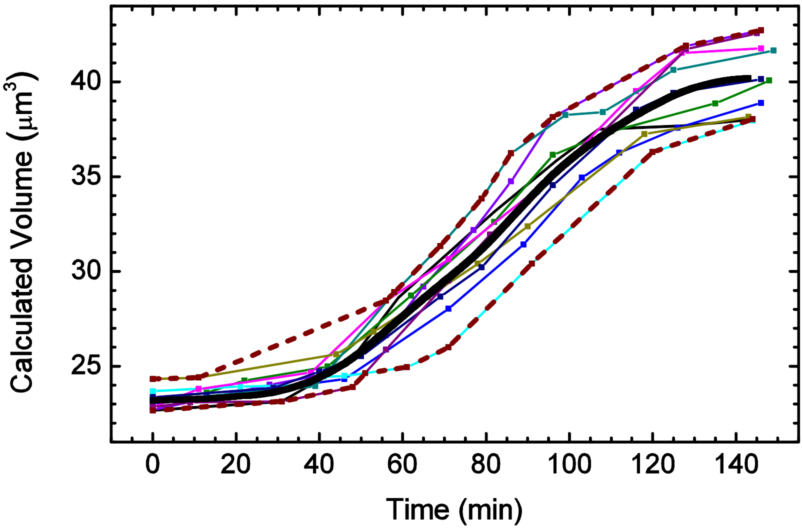

Figure 2.6: The absolute volume growth over time for 10 different daughter yeast cells. The volume growth data are seen to be bounded by two sigmoid curves computed from the family of interpolants and shown as the dashed red lines. The solid black curve at the center represents the pointwise average over the 10 interpolants of the data.

All ten measured growth curves display the same sigmoid shape characterized by an increase in slope where budding occurs, followed by a decrease in slope when the budded daughter cell becomes mature. The data are seen to lie within an envelope that is bounded by two sigmoid curves computed from the family of interpolants and shown as the dashed red lines in Fig. 2.6. The solid black curve at the center represents the pointwise average of the 10 interpolants of the data. The maximum root mean square deviation of the data from the mean curve is 1.38 μm^3. The small residual is a further indication, beyond visual inspection, that the mean curve well describes the trend of the data. The mean curve exhibits the sigmoid shape, which compares well with published literature (Mitchison, 2003; Woldringh et al., 1993).

The percentage growth of the yeast cell volume can be better perceived in a normalized growth rate, where the volume of each yeast cell is normalized with respect to its initial volume, as shown in Fig. 2.7. It can be seen that over the whole cell cycle, the total volume of the mother cell and its daughter can increase by 56% to 88%. It is clear from the normalized volume traces shown in Fig. 2.7 that the volume of the mother and daughter pair does not double prior to segregation at the end of mitosis. This phenomenon is attributed to the observation that the daughter cell is smaller at division than the mother (Stowers, et al., 2009). The magnitude of the size difference depends on the yeast strain, the growth environment and the replicative age of the mother. The larger the mother daughter size disparity the faster an initially synchronous culture will dephase. Quantitative data of the type shown in Fig. 2.7 will help us to more accurately parameterize models of yeast population growth and division (Brewer et al., 1984).

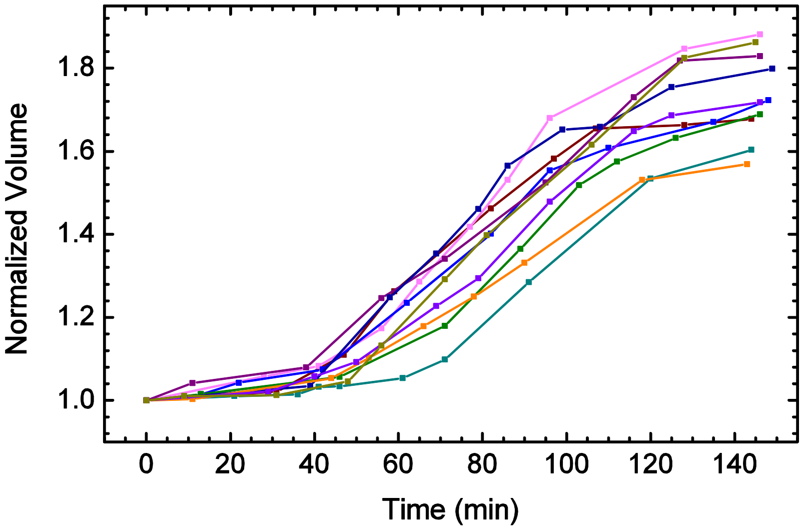

Figure 2.7: The normalized volume growth curves with respect to the initial volume of each yeast cell.

Data Analysis

In this section we provide an analysis of the measured data to investigate biophysical aspects of the yeast growth. An aspect of the analysis is to quantify the variation of the data and to determine the features that appear systematic. One way to accomplish this is to compute a mean curve and a bounding envelope, and to analyze the measurement results for each budding yeast cell with respect to these curves. Further we use the mean curve and its derivative to examine local and global growth models. The volume measurements from different experiments were made at non-corresponding time points, with non-uniform spacing within each measurement. Data analysis in such a situation is best performed using interpolation. All calculations were performed in the Mathematica environment (Wolfram Research, Inc.). The measured data were linearly interpolated and the pointwise min and max were computed to produce the upper and lower boundary curves. The effect of interpolation order has been checked by also performing third order interpolation and we found essentially no effects on the appearance of the mean curve or important derived quantities such as the RMSD.

An essential tool to analyze the properties of the data is the derivative of the mean curve shown in Fig. 2.8. The derivative provides a natural way to decompose the growth into several phases. Fig. 2.8a indicates that the qualitative behavior of the derivative of the mean curve recapitulates the important features of each individual curve (as shown in Fig. 2.8b). The essential qualitative behavior is that the slope(s) rise to a maximum and then decline, while always remaining positive, as is to be expected for growth phenomena. The mean curve begins with a 30-40 minute period of approximately linear growth, with a rate of ~0.01 μm^3/min. The derivative is seen to be multimodal with a brief shelf starting at 60 minutes that interrupts a 20-30 minute period of exponential like growth. The shelf then rises to the global maximum at 95 minutes. After this the derivative is in decline, nearly returning to its original value of 0.01 μm^3/min.

The links between yeast growth and metabolism are still incompletely understood. Many metabolic shifts and effects are known in yeast, too numerous to review or to comprehensively cite (Griffin, 1994; Rosa and Peter, 2006). For example, one well known metabolic shift that impacts growth rate and is an example of an interesting phenomenon that could be studied with the techniques described here. The diauxic shift is the transition from growth on fermentable sugars such as glucose to that on non-fermentable carbon sources such as ethanol, lactate, acetate and others, that become available or have accumulated in the media during prior metabolic activity (van Dam, 1996; Vivier et al., 1997). This phenomenon is commonly associated with a bisigmoid growth curve where the growth rate slows and then increases again. Often this behavior is attributed as a clever strategy on the part of yeast to outcompete other species who are less alcohol tolerant by rapidly consuming the high chemical potential carbon sources. Similar metabolic behaviors that result in changes in growth rate, such as the acetate switch, are well known in the bacterial world (Wolfe, 2005). Several of the individual derivative curves, shown in Figure 2.8b, at least four of the ten, display multimodality, providing evidence that this feature is realized, perhaps in a subpopulation. However, the derivative data are noisy and we have small sample. It is therefore concluded that the shelf in the derivative of the mean curve is an interesting and perhaps spurious feature revealed by the analysis that requires further measurements for confirmation.

Now we turn to analyzing mathematical descriptions or models of the mean growth curve. The data from 30 minutes to 60 minutes are best fit by an exponential model. This is shown in Fig. 2.9. Three growth models are considered. In Fig. 2.9a, the green curve depicts the best fit exponential model of the form $ae^{ct}+b$, the blue curve depicts the best fit linear model of the form $at+b$, while the red curve represents a power law model of the form, at^c+b. While the linear model has one fewer parameter, it is clear from the mean curve and its derivative, that the growth data display non-zero curvature. While the power law model fits the data qualitatively, the residuals in Fig. 2.9b show that the exponential fit is a better representation. The residuals also reveal that the time window in which the yeast are growing near-exponentially lies within the time interval from 37-54 minutes. The best fit parameters of the three models are shown in Table 2.1. These parameters can be used to accurately estimate the growth rate within this portion of the growth curve.

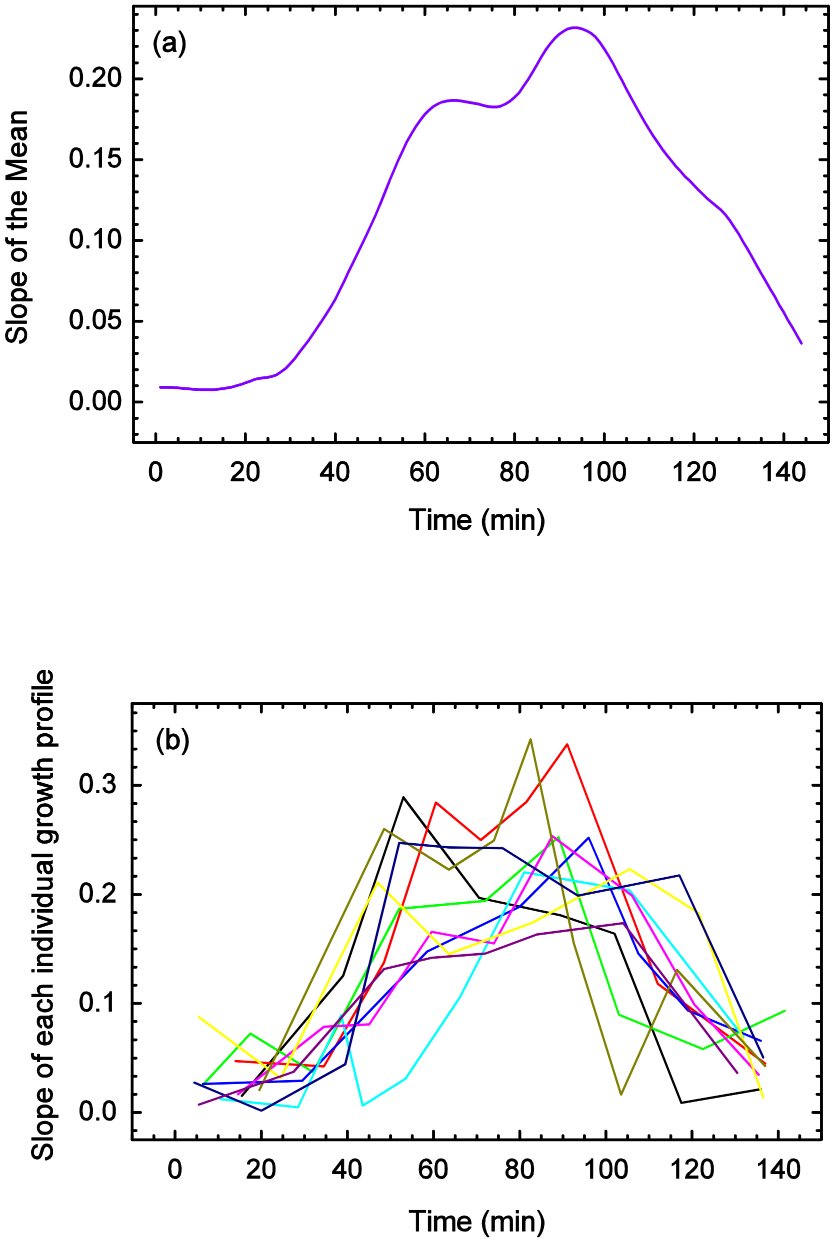

Figure 2.8: (a) The slope of the growth curve calculated as the derivative of the mean curve with respect to time; and (b) The slope of each individual growth profile. The slopes confirm that the mean curve captures the important features of each individual curve.

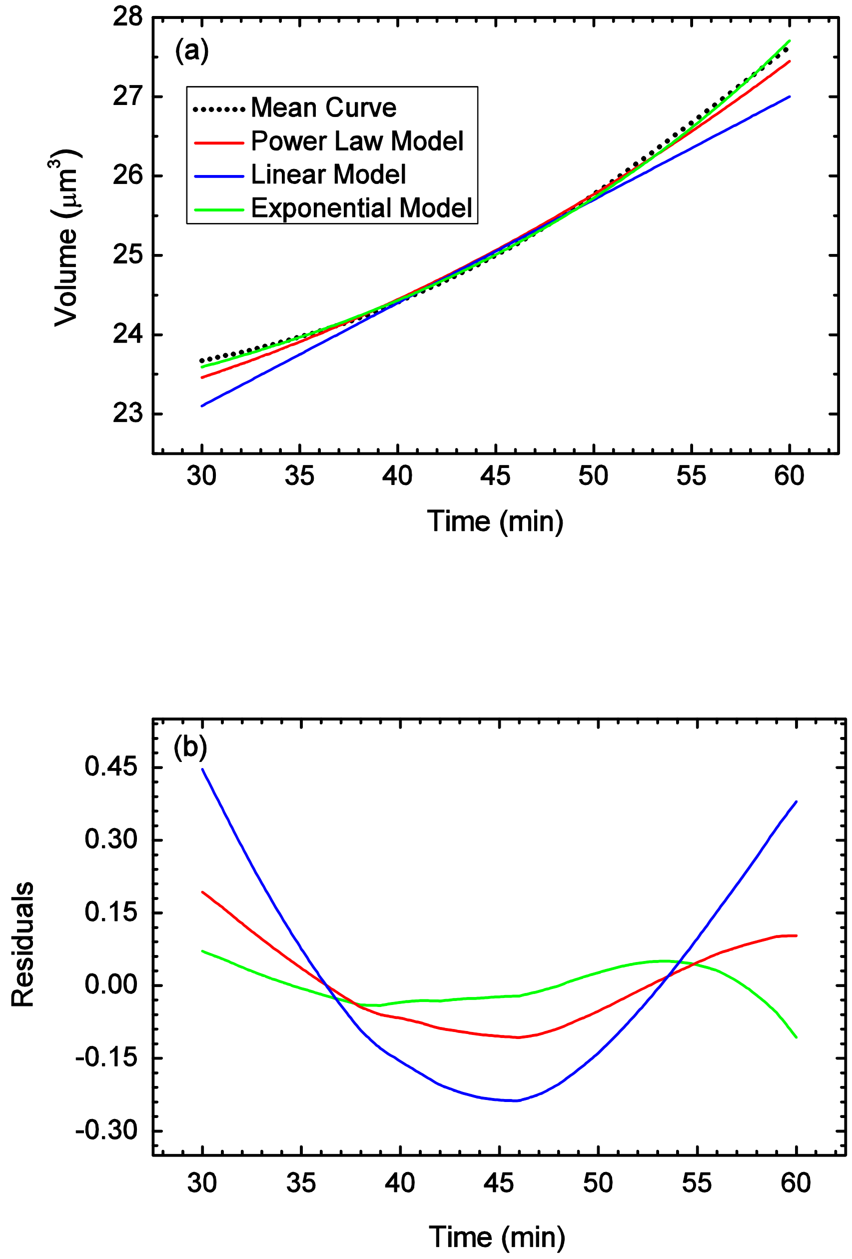

Figure 2.9: (a) The best fit models of three different functions for the local volume growth between 30 and 60 minutes; (b) The residuals of the three best fits.

Table 2.1 Best fit parameters and RMSD determined for the three different models against the mean curve data between t = 30 min and t = 60 min.

Parameter	**$ae^{ct}+b$**	**$at+b$**	**$at^{c}+b$**
a	0.43	0.13	0.00068
b	22.03	19.20	22.33
c	0.043		2.18
RMSD	0.036	0.20	0.083

Globally the growth data support several sigmoid models nearly equally well: A piecewise linear (PL) model with three segments,

$$PL(t) = \begin{cases} a(t-40)+b & for\ \ 0 \le t < 40 \\ (d-b)(t-40)/70+b & for\ \ 40 \le t < 110 \\ c(t-110)+d & for\ \ t \ge 110 \end{cases} \qquad (2.7)$$

a Gompertz growth model, $a+b\exp(-\exp(-ct+d))$, and a Hill's function, $a+\frac{bt^{d}}{t^{d}+c^{d}}$, all fit the data with nearly the RMSD as the mean curve, as shown in Fig. 2.10 and summarized in Table 2.2.

Table 2.2 Best fit parameters determined for the three models for the global growth.

Parameter	**Hill**	**Gompertz**	**PL**
a	23.4171	23.4366	0.0138779
b	19.001	18.4648	23.8511
c	84.2354	0.0342305	0.0706643
d	3.92566	2.47842	37.9011

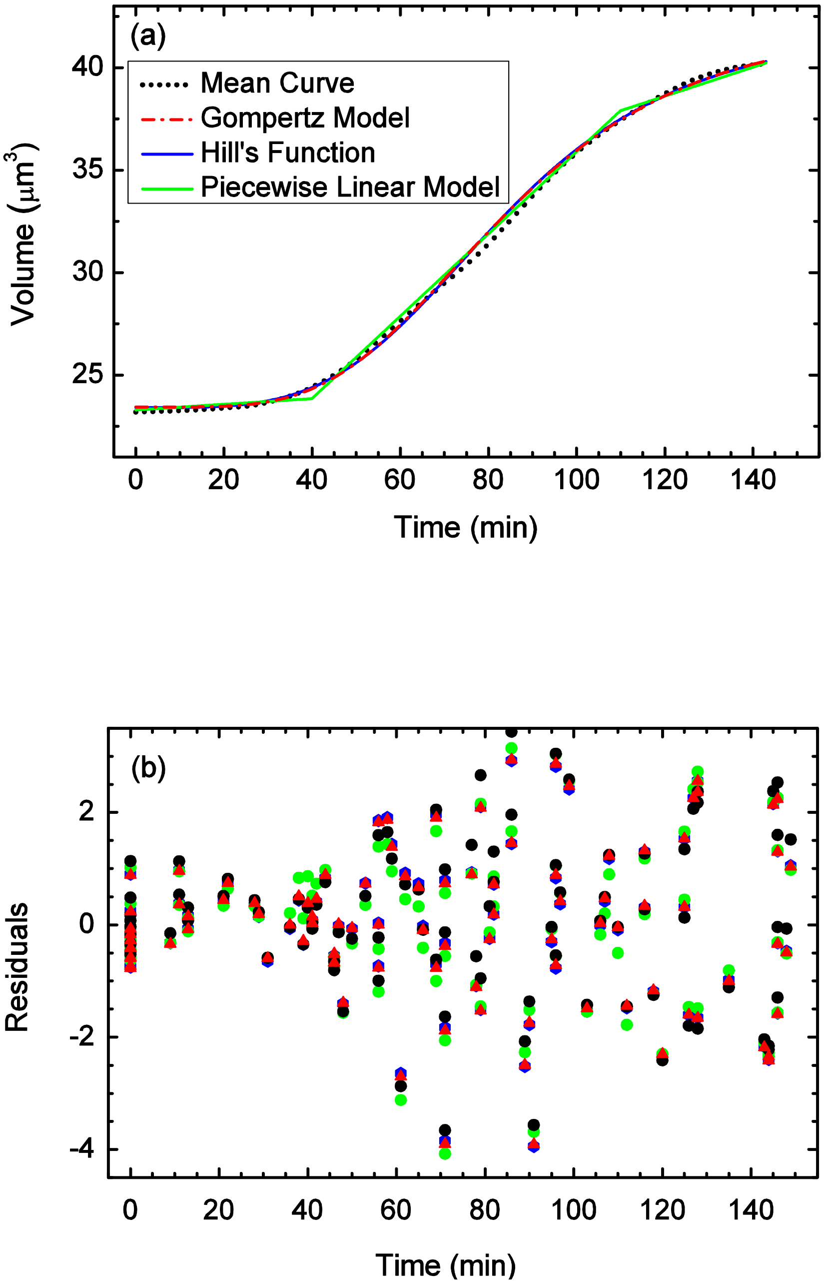

Figure 2.10: (a) Three different models for the global volume growth versus the mean experimental growth curve; (b) The residuals of the three different models in the corresponding colors.

Summary

The volume growth of ten individual budding yeast cells over their whole cell cycles has been measured with a MOSFET-based microfluidic Coulter counter. The enhanced sensitivity and the ability of using YNB media in the device allow for direct measurements of the volume growth rate of individual live yeast cells in physiologically relevant environment.

Measurement results indicate a sigmoid volume growth profile with reduced growth rates (0.01 μm^3/min) at the initial and the final stage of the cell cycle. The maximum growth rate in the fast growth phase is more than an order of magnitude higher, around 0.25 μm^3/min. Detailed analysis of the growth curve strongly suggests a local exponential growth phenomenon. However, the global growth curve can be described equally well by a piecewise linear and two nonlinear growth models.

The simple and convenient volume growth measurement technique and the ability to use cell culture media in the measurement set-up provide the possibility to measure yeast cell volume growth under different relevant physiological conditions to study the effects of different factors on yeast cell cycle.

CHAPTER III

THE REFERENCE CHANNEL-BASED MICROFLUIDIC RESISTANCE SENSING SCHEME

In this chapter, a reference channel-based sensing scheme, which can make real-time measurements with small time interval (1 second) between two measurement points, has been developed and demonstrated by monitoring the volume growth rate of single budding yeast cells. The device consists of two identical microfluidic channels: one sensing channel and one reference channel. The introduction of the reference channel allows for cancellation of the effects of baseline ionic current drift, which often exists in microfluidic devices. It is well known that in microfluidic circuits, the channel impedance drifts over time due to changes in the media caused by evaporation and electrochemical reactions at the electrodes, which is especially true for cell culture media containing complex components. In the reference channel-based microfluidic sensing scheme, the same ionic current passes through both the sensing and the reference channel; therefore, it is cancelled out when we compare the voltage drops across the sensing and the reference channel. Using this scheme, ideally we can eliminate any effects from the fluctuations and drifts of the ionic current and obtain the resistance information of the sensing channel, which is related to the volume of the cell in the sensing channel.

Motivation

We have demonstrated that the MOSFET-based microfluidic Coulter counter is able to measure the volume growth rate of single budding yeast cells over their whole cell cycles. However, several limitations associated with the sensing scheme can be identified: (1) The sensing scheme requires that cells are exposed to a relatively high electric field in the small sensing channel (Sun et al., 2010), which is because a few volts of electrical potential needs to be used to induce the electroosmotic flow to deliver the cell back and forth through the sensing channel; (2) Both the desire to reduce any potential side effects of the relatively strong electric field, and the time required to switch the polarity to alter the electroosmotic flow direction mandate a relatively long time interval between two data points; (3) This sensing scheme requires that cells are suspended in the culture media, which limits its applications to many cell types that need to attach to a substrate to be alive and function well.

One the other hand, real-time cell volume change is an important, relevant parameter in many cell biology studies. For example, the size or shape changes of lymphocyte can reflect whether they are activated or not (Ackerman and Knouff, 1959). In addition, the volume growth of transformed cells due to the loss of growth inhibition is tied to the loss of tumor-suppression gene function (Butler et. al., 2001). Other examples include the response of MDCK cells to osmotic challenges marked by volume swelling (Hua and Pennell, 2009), and the volume growth of *Saccharomyces cerevisiae* as a direct proxy for cell cycle progression (Sun et al., 2010). Therefore, we pursue new microfluidic resistance sensing schemes that overcome the limitations of the MOSFET-based resistive-pulse sensing technique, which should be able to measure cell volume changes in real-time, allow cells to attach to the substrate and expose to lower electric field. In this chapter, we describe a reference channel-based sensing scheme that enables real-time detection of the volume change of single cells attached to the substrate, which is demonstrated by measuring the volume growth rate of single yeast cells in a small microfluidic channel.

Theory

Electrical Current through Microfluidic Channels

It is well known that various factors can influence the electrical current in microfluidic channels, such as evaporation of the media, evolution of the surface charge density, and electrochemical reactions at the electrodes. The charged species in a microfluidic channel will experience electrostatic force under an applied electric field, giving rise to a drift current. In addition, if the concentration of charged species is not uniform, the mass diffusion will also lead to an electrical current. This is further coupled with the flow of charged species driven by other external field such as a pressure difference, which is known as streaming current. Considering a dilute solution, the current density, $\vec{\imath}$, combining all the above-mentioned contribution can be written as (Probstein 1994):

$$\vec{\imath} = -\sigma \nabla \phi - F \sum z_i D_i \nabla c_i + F \vec{u} \sum z_i c_i, \qquad (3.1)$$

where σ is the scalar electrical conductivity of the solution, ϕ is the applied potential, F is Faraday's constant, z_i is the charge number, D_i is the mass diffusivity, c_i is the molar concentration, respectively, for species i, and $\vec{u}$ is the average velocity. From this equation, the electrical current through a microchannel is related to the electrical conductivity, the external electric field, the concentration gradient of each species, and the average velocity.

The basic principle of electric impedance-based sensing is to exploit changes in the electrical resistance resulting from different electrical conductivities between biological cells and the surrounding medium. For impedance measurement, a constant voltage or an AC current source is used to provide the baseline electric current, and a differential or a lock-in amplifier is used to measure a voltage signal to extract the impedance change (Ateya et al., 2005; Sabounchi et al., 2008; Scott et al., 2008). Ideally, the baseline electric current should be extremely stable and modulation of the current should be solely due to the changes in cell properties, such as cell volume. Eqn (3.1) states that this condition could be satisfied if the solution is electrically neutral, the concentration gradient is zero, and the convection of charge can be neglected.

However, if an electric field exists in a microfluidic channel, electrolytic reactions could occur inside the channel, which could significantly change the concentration and velocity of some species. Therefore, the electric current will be affected by many factors in a complex manner. This is especially true for microfluidic channels filled with cell medium containing multiple components, such as sodium chloride, phosphates and glucose. As a consequence, most impedance-based detection scheme in microfluidic systems face the challenge of background electric current drift over time, especially for long-term measurements (Scott et al., 2008; Hua and Pennell, 2009). In extreme cases, the current modulation caused by the presence or swelling of cells could be totally overwhelmed by the background electric current drift.

To reduce the effects of background electric current drift, we introduce a reference channel, which is placed very close to the sensing channel in the microfluidic sensing system. Therefore, the effects of background electric current drift can be eliminated by comparing the voltage drop across the sensing and the reference channel. The ratio of voltage drop across the sensing and the reference channels only involves the resistance of the sensing and the reference channel but not the electric current through the microfluidic channel, which can be used to extract the resistance change of the sensing channel. If we further assume that because the sensing and reference channels are very close to each other and the electrical conductivity of the media in both channels are the same, then the resistance ratio only contains the geometrical information of the channel, and hence, the volume change of the cell inside the sensing channel.

Cell Growth Inside A Small Channel

It has been shown that the relative electrical resistance change of a tube filled with conducting media from the presence of an insulting sphere is proportional to the volume fraction of the sphere to the tube in the small sphere limit (Maxwell and Thomson, 1904; Deblois and Bean, 1970). If a cell is approximated as a sphere that is electrically non-conducting at low electrical frequency, its volume can be determined via impedance-based detection. However, cell shapes can deviate significantly from spherical. For example, for budded yeast cells, it is a lopsided peanut shape instead of spherical. Therefore, it is necessary to first obtain the relation between the channel resistance change and the cell volume inside the channel. To do so, the electrical resistance change due to a budding yeast cell growing asymmetrically inside a small channel was calculated by a three-dimensional finite element model using Comsol Multiphysics 3.3 (Comsol, Inc).

The unbudded yeast cell first increases in volume until a bud bulges from it. After bud emergence the mother yeast cell grows very slowly and most volume increase is from the bud, which will eventually divide from the mother cell. During the budded period, a bud on a mother cell will result in a lopsided peanut shape (Hartwell and Unger, 1977; Koschwanez et al., 2004). We first consider an unbudded mother yeast cell as a sphere of diameter D ($D = 4\ \mu m$), attached to the bottom of a microfluidic channel (15 μm wide, 8 μm deep and 15 μm long) (Fig 3.1a). The channel is filled with yeast medium and a bud emerges along the x-axis where the effect of flow-induced shear stress is unnoticeable (Tourovskaia et al., 2005). The bud is generalized as a small sphere that has an initial diameter d ($d = 0.4\ \mu m$). The distance between the centers of the two spheres can be taken as $\frac{D+d}{2} - 0.1\ \mu m$, which accounts for the overlap between the two spheres (Fig 3.1b). At each time step, the diameter of the bud increases by Δd ($\Delta d = 0.4\ \mu m$), and the distance between the two centers subsequently increases by $\frac{\Delta d}{2}$ (Fig. 3.1c) till the diameter of the bud reaches 4 μm (Fig. 3.1d). The total volume of two intersecting spheres is computed using a MATLAB code (MATLAB®).

If we neglect the effects of species concentration non-uniformity and the pressure driven flow, the electrical current density through the microfluidic channel can then be determined by solving the following governing equation:

$$\nabla \cdot (-\sigma \nabla \phi) = 0. \qquad (3.2)$$

The expression within the brackets represents the current density.

Eqn. (3.2) is solved subject to a 0.06 V potential difference across the channel, with a medium electrical conductivity of 0.01 S/m, a cell electrical conductivity of 1×10^{-20} S/m and insulting surfaces at all other boundaries. From this solution the electrical current through the channel can be computed by integrating the current density through any cross section. The electrical resistance of the channel is then equal to the ratio of the applied voltage divided by the electrical current.

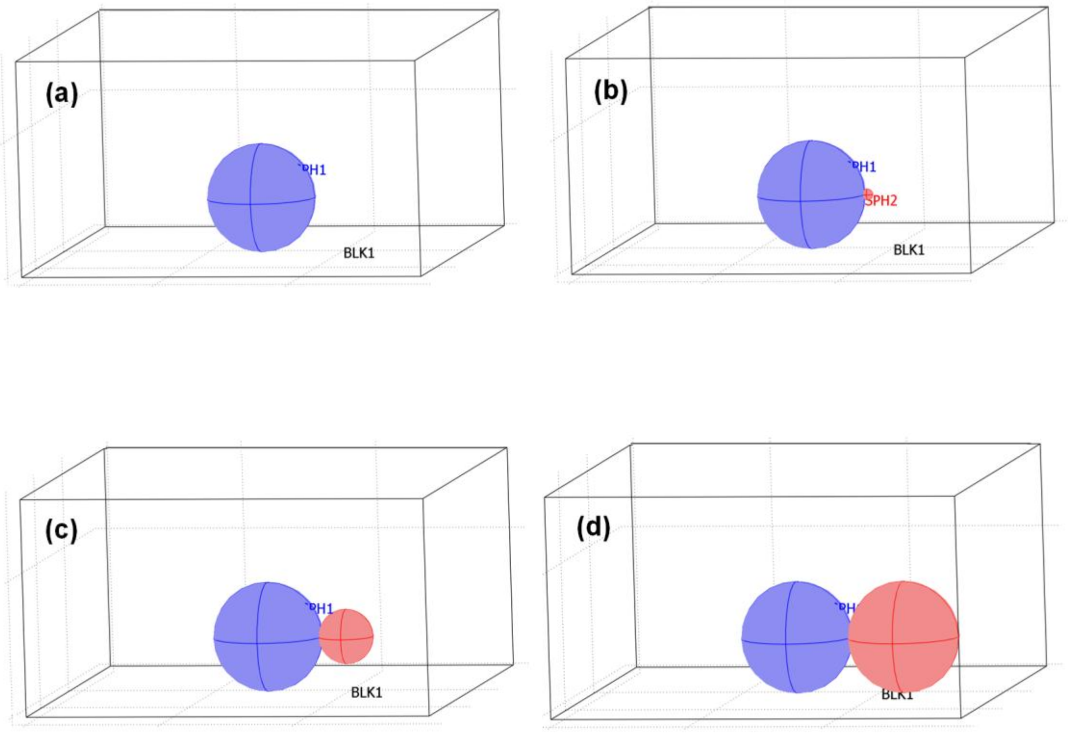

Figure 3.1: (a) A spherical yeast cell (4 µm in diameter) attached to the bottom of a microfluidic channel (15 µm wide, 8 µm deep and 15 µm long); (b) A spherical bud with a diameter of 0.4 µm emerged along the x-axis; (c) The diameter of the bud increasing by 0.4 µm at each time step; and (d) The spherical bud finally reaches 4 µm in diameter.

Fig. 3.2 plots the distribution of electric potential (isosurfaces), electric field (streamlines) and total current density (arrows) in the channel with a budded yeast cell trapped inside. It can be seen that all the electric potential, electric field and total current density are disturbed around the cell. The ten points in Fig. 3.3 represent the electrical resistance of the channel as a function of cell volume in the range from 33.49 µm^3 to 66.96 µm^3. A best fit linear relationship between the resistance and the cell volume is also plotted in Fig. 3.3.

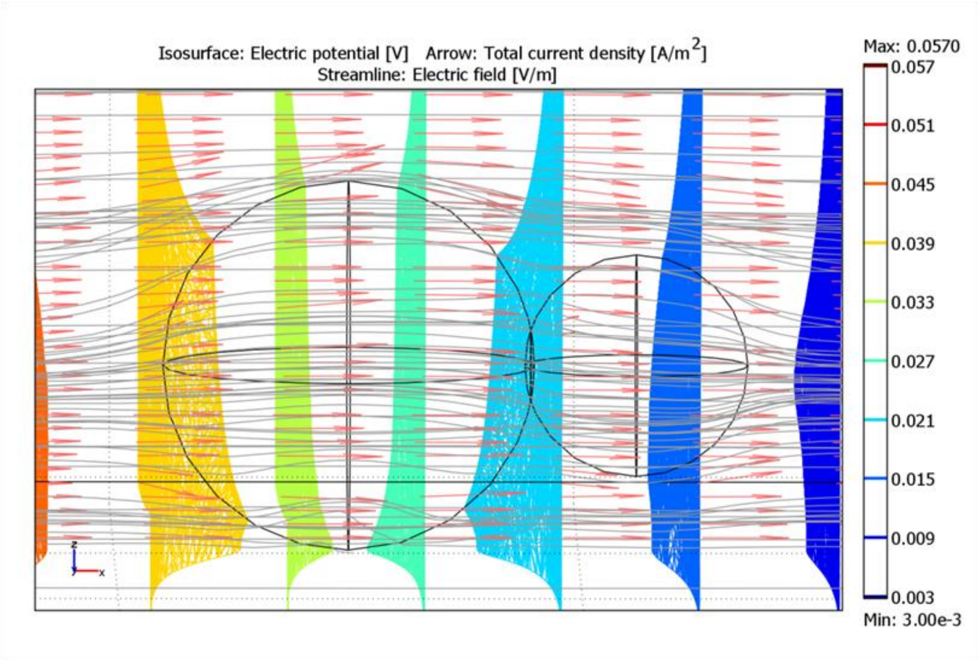

Figure 3.2: Finite element analysis of the electric potential (isosurfaces), the electric field (streamlines) and total current density (arrows) in the channel with a budded yeast cell inside.

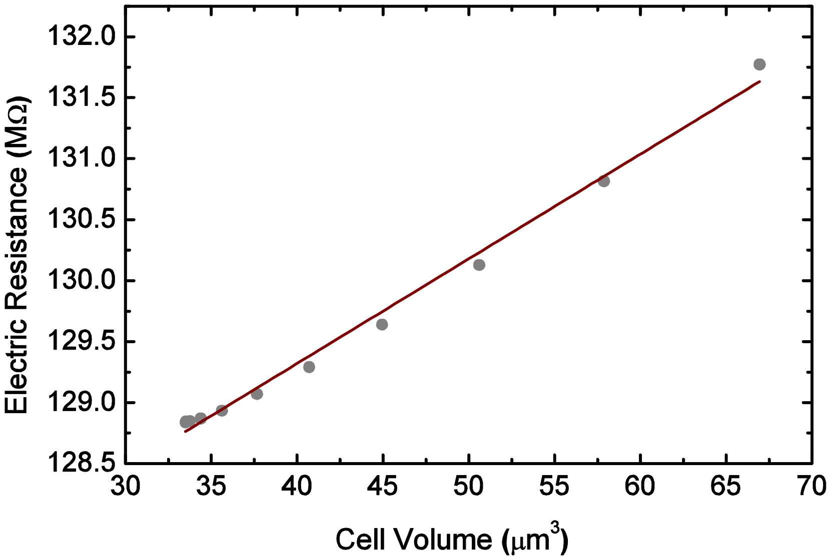

Figure 3.3: Plot of the cell volume versus the electrical resistance of the channel. The solid line represents the best fit linear relationship between the two terms.

Experimental Methods

Device Fabrication

An optical micrograph of a prototype reference channel-based microfluidic device is shown in Fig. 3.4. The device contains a horizontal main flow channel of 100 μm wide and 8 μm deep, bisected by a sensing region with reduced cross-section in which the sensing channel and the reference channel are designed to be identical (15 μm×8 μm×15 μm in terms of the channel width, depth and length, respectively). Four vertical microchannels located at the inlet and exit of the sensing and the reference channel are constructed for voltage measurements.

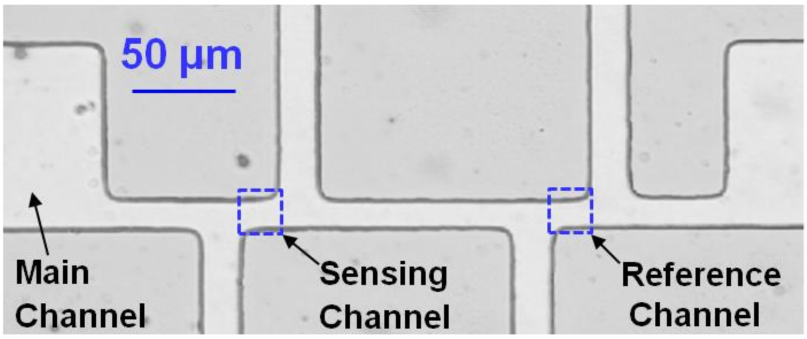

Figure 3.4: An optical micrograph of a prototype reference channel-based microfluidic device.

The device was fabricated following standard soft lithography techniques (Sia and Whitesides 2003). SU-8 2005 photoresist (MicroChem Corp) was first spin-coated on a 3 inch silicon wafer at 500 rpm for 10 sec followed by 1000 rpm for 30 sec to obtain the desired thickness (8 μm). The coated wafer was soft-baked and then exposed to ultraviolet light through a photomask containing the pattern of microfluidic channels. After exposure, the wafer was baked again at 95 °C for 3 min and soaked in SU-8 developer (MicroChem Corp) to dissolve the unexposed photoresist. The patterned SU-8 master mold was then hard-baked at 150 °C for 5 min to anneal microcracks in SU-8. Degassed PDMS (mixed in a 10:1 ratio of PDMS base with curing agent, Sylgard 184, Dow Corning Inc) was cast over the mold and baked at 80 °C for 3 hr in an oven. The PDMS with embedded channels was subsequently diced by razor blade and removed from the master mold. The horizontal inlet and outlet ports as well as four vertical sensing ports at the ends of the channels were punched through the PDMS by a 4 mm biopsy punch. Finally, the PDMS was bonded to a glass substrate after oxygen plasma treatment for 30 sec.

Experimental Procedure

Fig. 3.5 shows the measurement setup of the reference channel-based microfluidic device. In the measurement, a low concentration yeast suspension (LHY3865, a strain of *Saccharomyces cerevisiae*, at 1×10^3 cells/mL) in YNB media was perfused through the microfluidic channels. Six platinum wire electrodes were submerged into each filling port to connect the fluidic circuits to the external electronic circuit. After an unbudded yeast cell coated with poly-d-lysine was deposited into the sensing channel, four vertical ports were covered by a thin PDMS layer serving as a tight fluid seal. Then, a small DC voltage (Agilent E-3612A, Agilent Technologies) was applied across the horizontal channels. The voltage drops across the sensing and reference channels are measured by two differential amplifiers (AD621, 100× gain, Analog Devices, Inc.) with large internal impendence (10 GΩ). The fluidic circuit was placed into an aluminum

Faraday cage to eliminate environmental electromagnetic noise. The device temperature was held constant at 29±1°C by radiation heating from a lamp. The sensing electronics, power source, and the data acquisition system were all commonly grounded. The output signals and the ratio between them were recorded and calculated using a LABVIEW code through a data acquisition board (PCI 6281, National Instruments).

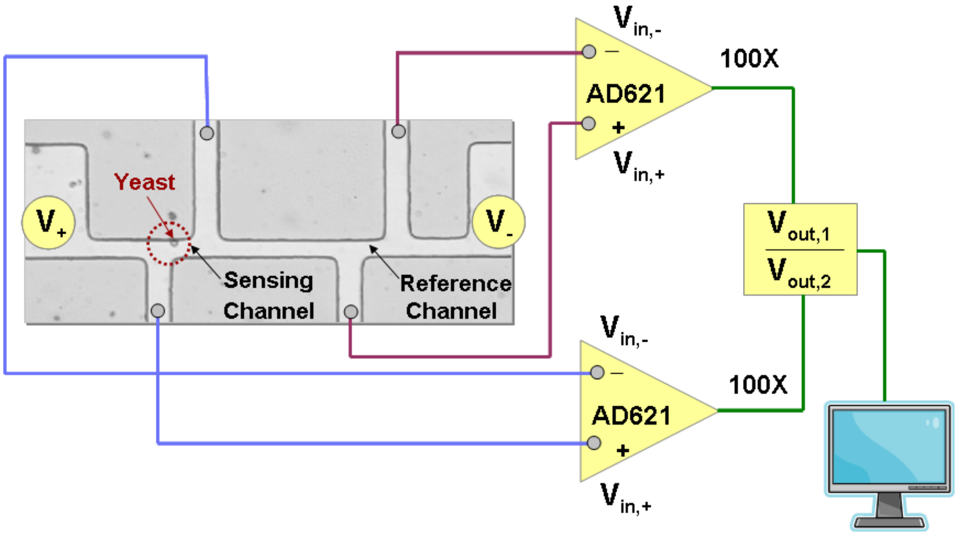

Figure 3.5: A schematic of the measurement setup of the reference channel-based microfluidic sensing scheme.

Results and Discussions

Calibration of the Reference Channel-based Microfluidic Sensor

Ideally, the ratio of the voltage drops across the sensing channel and the reference channel is proportional to the resistance ratio of the two channels because the same ionic current, which passes through both channels, is cancelled out. To verify that the ratio of the voltage drops is not affected by factors such as media evaporation and electrical drift, etc. over a long period of time, the first experiment carried out was a long term stability test. The stability test was performed by filling the microfluidic channels with 75 mM borate buffer and recording the voltage drops across the sensing and the reference channel for about 2.5 hours, after which the buffer solution in the upstream reservoir was replaced with 10 mM borate buffer and the measurement was continued for another 5.5 hours. The ratio of the voltage drops was calculated using a LABVIEW® code and plotted in Fig. 3.6. Fig. 3.6a plots the voltage drops with a 100× gain across the sensing channel and reference channel, and Fig. 3.6b shows the ratio of the voltage drops across the two channels over the whole test period. It can be seen that although the voltage drops across the sensing and the reference channel drift over time, their ratio remains nearly as a constant, and does not change with the buffer concentration replacement, either. The maximum residual drift of the voltage ratio including any noise is estimated to be ~0.205%, as shown in Fig. 3.6b.

The same experiment was repeated with the YNB media filled into the device and the measured voltage drops and their ratio are plotted in Fig. 3.7. In this case, we found that the ratio of the voltage drops is still constant with a slightly larger maximum residual drift of ~0.270% over a time period of 3 hours. Compared with the borate buffer, the ingredients of the YNB media are much more complex. The pH value and the concentration of each ingredient may change inside the microfluidic channel with time. Fortunately, the experimental results, as shown in Fig. 3.7b, indicate that the voltage ratio still remains constant with the YNB media. Therefore, the reference channel-based microfluidic sensing scheme can be used to measure the volume growth of live cells over time.

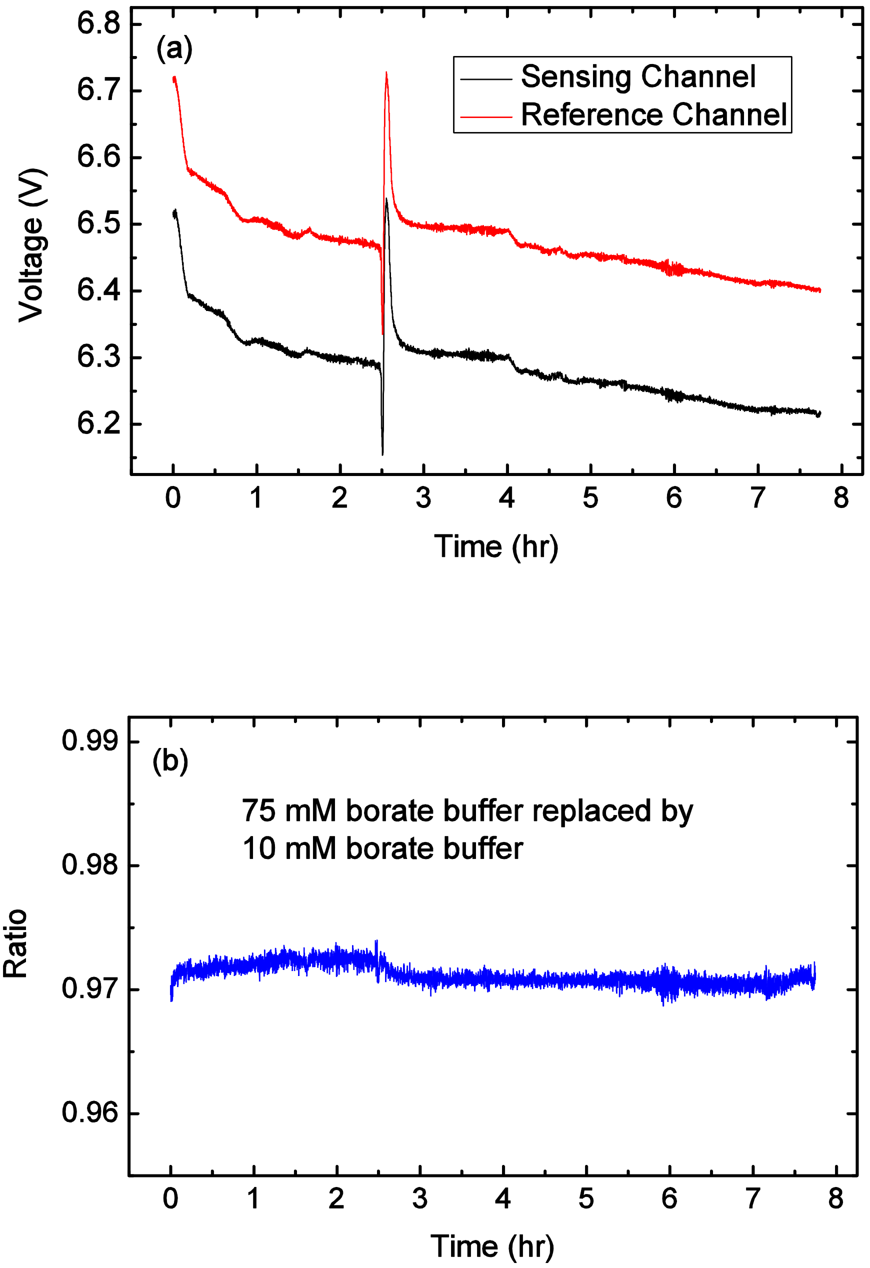

Figure 3.6: (a) Voltage drops with 100× gain across the sensing and the reference channel primed with 75 mM borate buffer, which is replaced with 10 mM borate buffer at ~ 2.5 hr; (b) The ratio of the voltage drops across the sensing and reference channels over a total test period of 8 hr with a maximum residual voltage ratio drift of ~0.205%.

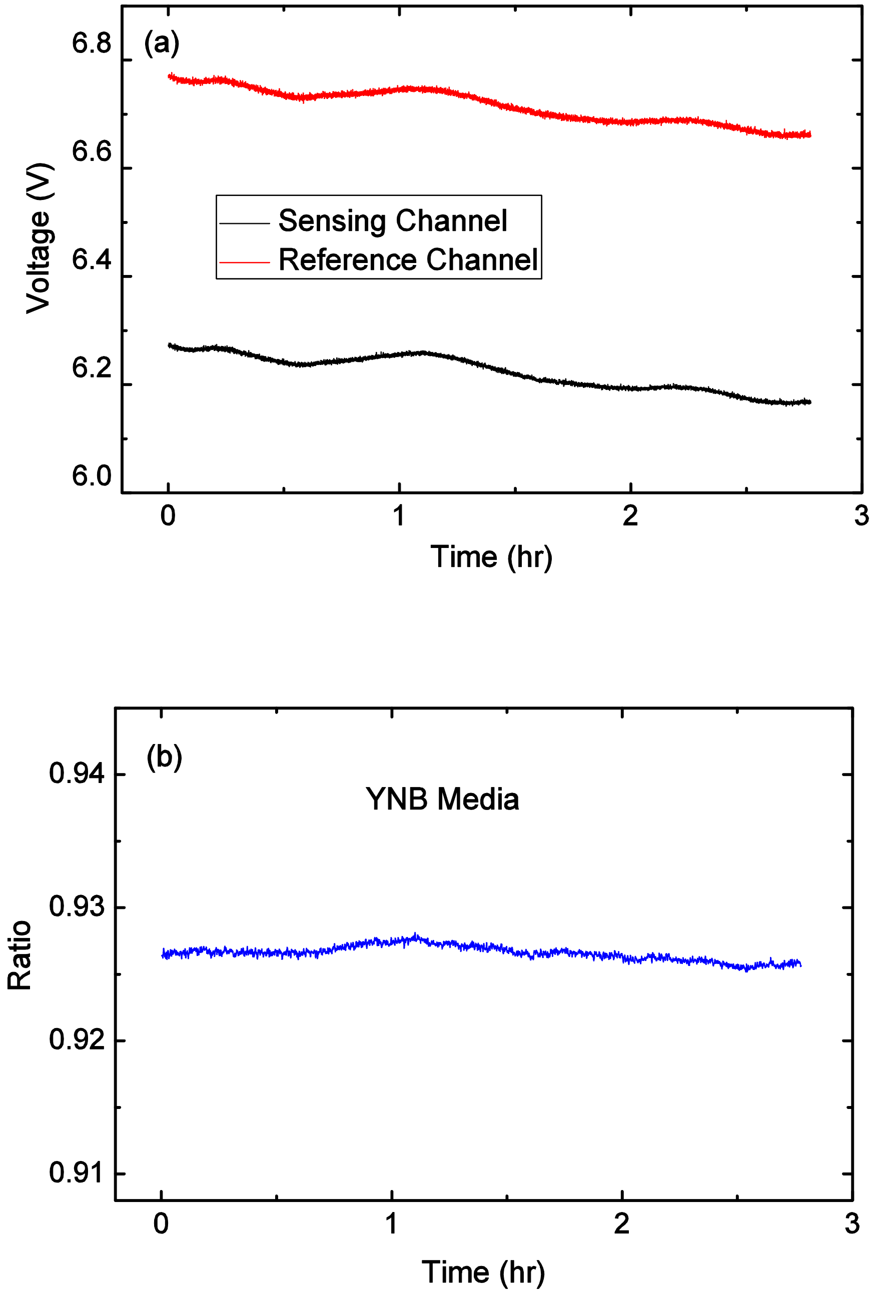

Figure 3.7: (a) Voltage drops with 100× gain across the sensing channel and the reference channel primed with YNB buffer; (b) The ratio of the voltage drops between the two channels over a test period of 3 hr with a maximum residual voltage ratio drift of ~0.270%.

To determine the volume growth of the budding yeast, as in the MOSFET-based sensing scheme, the performance of each device was calibrated with over a hundred of 4.84 μm diameter polystyrene beads (PS05N, Bangs Laboratories, Inc.) in a dilute suspension, with results plotted in Fig. 3.8.

Fig. 3.8 shows the transient voltage modulation as the polystyrene beads were translocated through the sensing and the reference channel. Each translocation event contributed to a transient increase in resistance of either the sensing or reference channel, which consequently led to two voltage pulses corresponding to bead translocation through each of the two channels. Since the cross-sectional area of the bead is much smaller than the sensing and the reference channel, the amplitude of the voltage pulse is proportional to the volume of the bead. The mean diameter of the microbeads was taken as 4.84 μm, and the average amplitude of the upward voltage ratio pulse was determined (4.95%). This ratio of voltage drops was then used as a reference for calculation of the volume of the budding yeast inside the sensing channel.

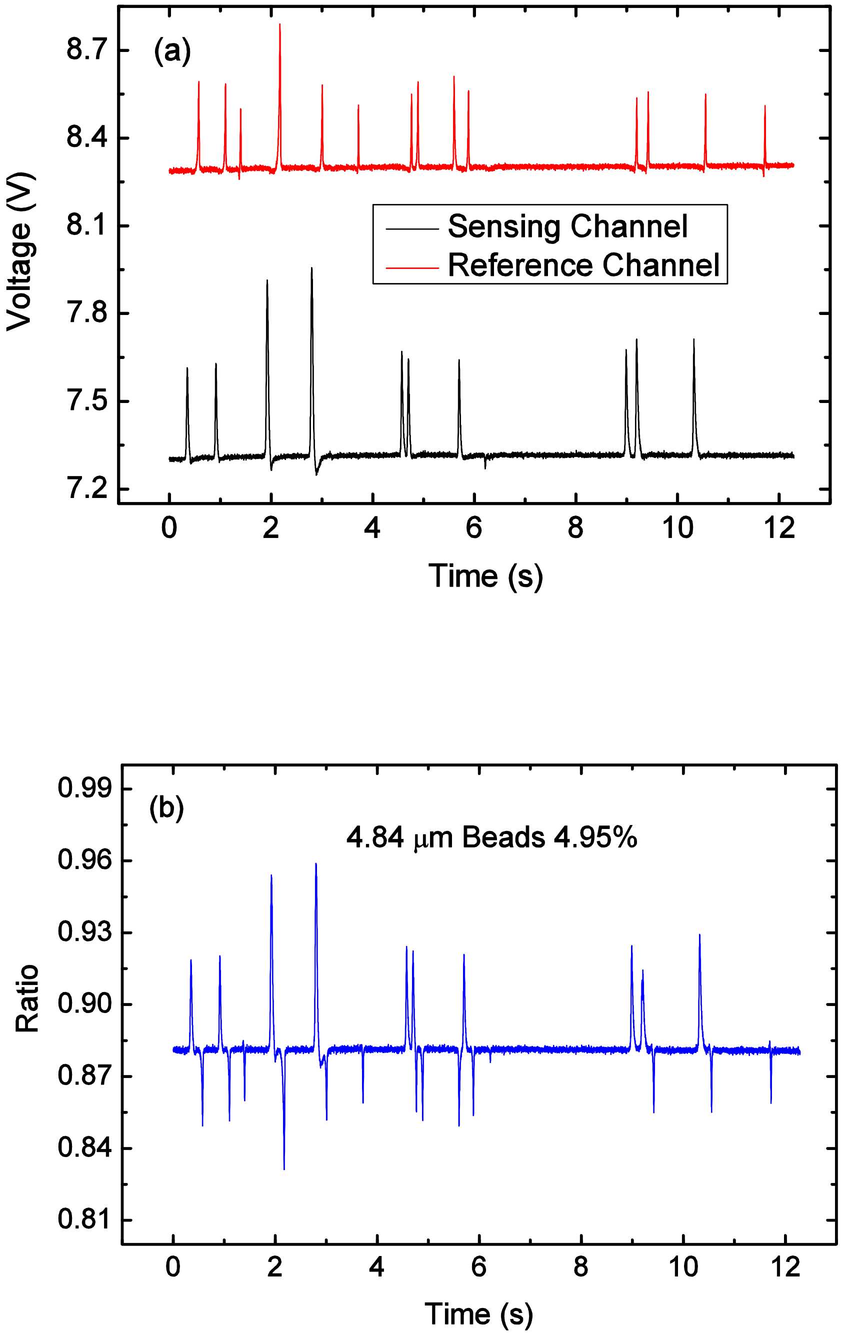

Figure 3.8: (a) Voltage modulation with 100× gain of the sensing and the reference channel during the passage of 4.84 μm in diameter polystyrene beads; (b) The voltage ratio pluses between the two channels. Note that some signals correspond to double beads.

Measurement of Yeast Volume Growth with the Reference Channel-Based Sensing

Due to the presence of a single yeast cell that can be regarded as an insulating object, the electrical resistance of the sensing channel was slightly increased. For live cells, the channel resistance will increase continuously as the cell grows in the sensing channel, whereas the resistance of the reference channel remains the same. As a result, the ratio of the sensing channel resistance to the reference channel resistance will increase continuously and the cell volume growth can be derived from the measured resistance ratio versus time. In this way, the reference channel-based sensing scheme cancels out any drifts of the electrical conductivity of the culture media due to factors such as evaporation. In addition, in this sensing scheme, the cell does not need to be moved back and forth with electroosmotic flow because it stays within the sensing channel. Accordingly, a relatively low potential can be used and the induced electric field within the microfluidic circuits is much smaller than that in the MOSFET-based sensing scheme. Therefore, any unexpected negative effects from both the electric field and the related Joule heating, can be further reduced. With the much smaller electric field, the voltage can be applied constantly and the measurement becomes real-time with small time interval between any two neighboring data points.

After the calibration run, the volume growth rate of a single daughter cell was measured and the voltage drops across the sensing and the reference channel are shown in Fig. 3.9. Fig. 3.9 clearly indicates that the ratio of the sensing channel resistance to that of the reference channel increases over time. The volume of the measured yeast cell was calculated based on the average amplitude of the upward voltage ratio pulses recorded from the translocation of the polystyrene beads. In the experiment, the ratio of the voltage drops across the sensing and the reference channel increases from 0.913 to 0.941, which corresponds to an initial size of a single daughter yeast cell of 4.2 μm in diameter and a volume growth of 36.8 μm^3, respectively.

Fig. 3.9 indicates that similar to the measurement results from the MOSFET-based microfluidic Coulter counter, a continuous increase in cell volume is obtained from the reference channel-based microfluidic volume sensor during the 2.5-hour measurement. The continuous measurement leads to a real-time volume growth curve, in contrast to the discrete data points with a ~15 min interval from the MOSFET-based microfluidic Coulter counter. Besides providing real-time measurement data, with a significantly lower electric field (30 V/cm), the reference channel-based microfluidic device possibly offers a more amicable microenvironment for yeast cell growth, as compared to the MOSFET-based microfluidic Coulter counter (122.6 V/cm across the sensing channel). The trend of the growth curve also agrees well with the measurement based on optical microscopy observation (Woldringh et al., 1993).

We have also measured the volume growth trends of another two single yeast cells using the same sensing scheme. The time course of absolute volume growth of three single cells was plotted in Fig. 3.10. The absolute volume increase were found in the range of 32.7~40.7 μm^3. The variation in volume growth may be the result of different generations of cells and multimodal volume distribution.

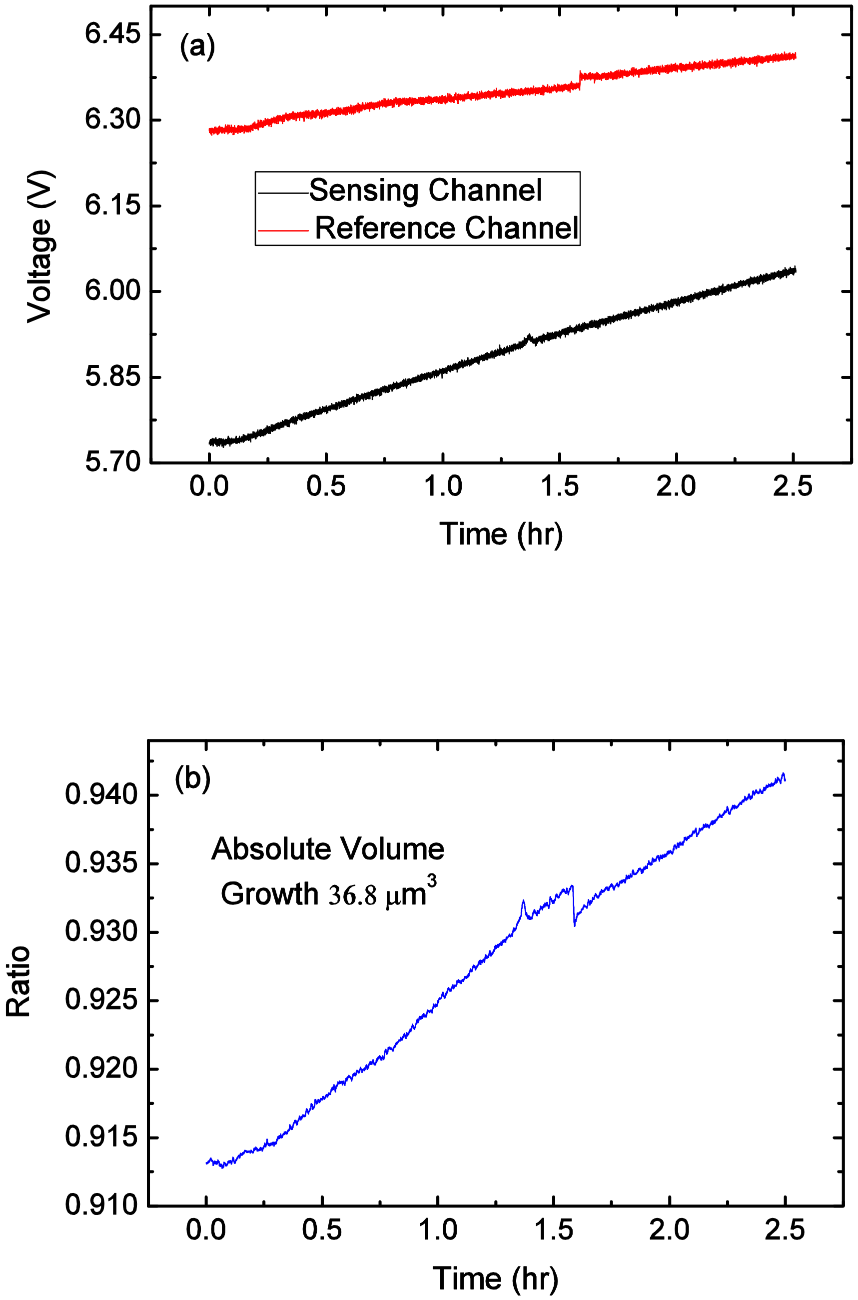

Figure 3.9: (a) The voltage drops across the sensing channel and the reference channel with 100× gain when a daughter yeast cell grows inside the sensing channel; (b) The daughter yeast volume growth curve, which corresponds to a volume growth of 36.8 µm^3.

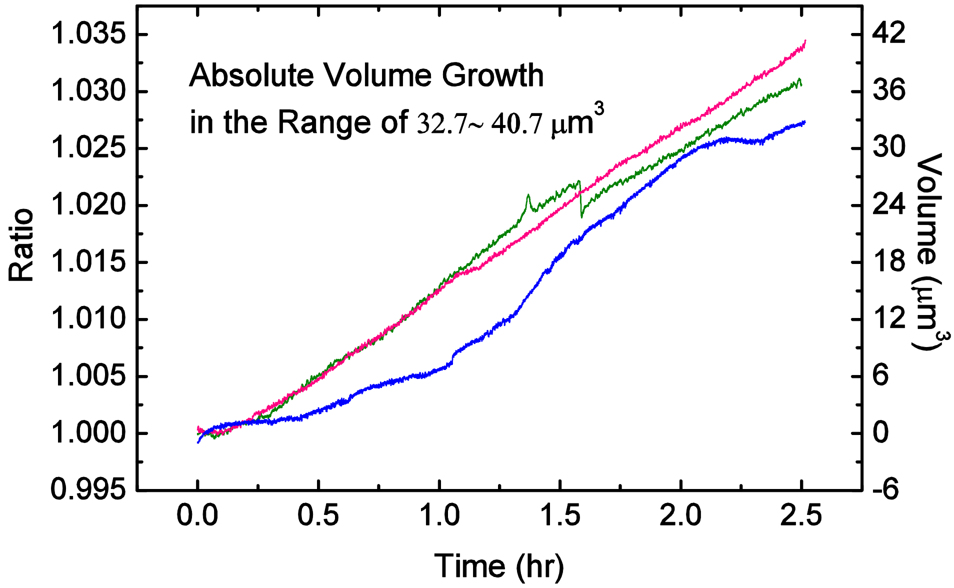

Figure 3.10: Plot of the time course of absolute volume growth of three single cells. The absolute volume increase was found to be in the range of 32.7~40.7 μm^3.

Summary

A reference-channel based microfluidic sensing scheme has been developed and applied to measure the budding yeast volume growth rate. Measurement results demonstrate that similar to the MOSFET-based microfluidic Coulter counter, the reference channel-based volume sensing technique can successfully measure the volume growth rate of individual budding yeast cells. The MOSFET-based Coulter-type sensing scheme is more sensitive while the reference channel-based scheme can provide real-time data. In addition, the reference channel-based sensing scheme allow for volume measurement of cells that need to attach to the substrate to be healthy and function well. The lower applied electric field further reduces any potential side effects of external electric field to cells.

The measured volume growth profile reveals a continuous increase in cell volume with respect to time, similar to that reported in the literature using traditional measurement methods. Although this work is focused on the volume measurement of single yeast cells, we expect that this technique can be used for other applications such as detecting the volume change of kidney cells in response to their microenvironment alteration and measuring the volume increase of other mammalian cells at the single cell level.

CHAPTER IV

SIMULTANEOUS SIZE-BASED MICROFLUIDIC CELL SEPARATION AND CHARACTERIZATION

As previously described, DC dielectrophoresis (DEP) involves creation of DEP force acting on dielectric objects, such as particles and cells, under a non-uniform DC electric field. DC DEP can be utilized to separate cells by size because it deflects cells and alters their trajectories to different levels according to the cell size. Integration of the size-based DC DEP cell separation and MOSFET-based resistive-pulse sensing can provide quantitative characterization of cell separation performance and insights for device optimization based on the characterization results. In this chapter, we present the study of DC DEP on-chip separation of particles and cells and simultaneous on-chip characterization of the separation performance. We demonstrate that the separation performance depends on the cell flow rate in a nearly linear manner within certain range. We also show that this device can be used to separate mammalian breast cancer cells from bone marrow cells. Quantitative characterization data indicate that good separation was achieved.

Motivation

Flow cytometry and cell separation are critical technologies that have played important roles in cell biology studies and biomedical diagnostics since their inception over half a century ago. Recent development in microfluidics offer advantages in many aspects and new functions to this established technology, which dovetail with the contemporary interest in the behavior of small cell populations or even single cells in controlled microenvironments. The advantages of microfluidic devices include low sample and reagent consumption, portability, and integrated functions, etc (Pamme, 2007; Tsutsui and Ho, 2009; Radisic et al., 2006).

There are a wide variety of biological applications and settings in which such devices can make big impacts. For instance it has been suggested that an on-chip device with size-based separation capability could maintain yeast cell population synchrony for over 30 cycles of mitotic division as opposed to the current best of 3-4 cell cycles (Stowers et al., 2010). This drastically elongated cell cycle synchrony will not only change studies of cell cycle and cell cycle dependent gene regulation, but also transform industrial processes in which product is recovered from micro-organisms whose metabolic activities are cell cycle dependent. Bioseparation is also vital in many areas of cancer biology. For instance it is of great interest to isolate metastasizing tumor cells from a serum sample. Metastatic lesions can be genetically different from the primary tumors. Considering the fact that majority of deaths from cancer in human patients result from metastasis, it is extremely important to better understand the difference between metastatic tumor cells and the primary tumor cells. Therefore, a device that separates and concentrates a population of circulating tumor cells provides the means to study this important cell type.

As pointed out at the end of chapter I, currently the development of microfluidic cell separation techniques mainly focuses on the separation principle and lacks attention to careful quantitative characterization of the separation performance. For example, microfluidic DC DEP cell sorters have recently been developed to separate a mixture of different size cells or particles; however, the separation performance of the microfluidic DC DEP cell sorters has only been shown with qualitative images but not evaluated quantitatively (Kang et. al., 2006; Kang et. al., 2008). Therefore, careful simultaneous on-chip characterization of the cell separation performance would yield important information about the cell separation technique, which can be used for better device design or operation protocol.

Theoretical Analysis of Size-Based DC DEP Cell Separation

In an aqueous electrolyte-filled microchannel, an electric double-layer (EDL) at the solid-liquid interface is formed because of the interactions between the surface charges and ions in the solution. Under an externally applied electric field, an electroosmotic flow (EOF) will occur due to the motion of the net mobile ions within the EDL. In the limit of thin electric double layers, a slip velocity exists at the channel wall for the EOF, which can be described by the *Helmholtz-Smoluchowski* equation (Probstein, 1994) as:

$$\vec{u}_{slip} = -\frac{\varepsilon_s \zeta_w \vec{E}}{\mu}, \tag{4.1}$$

In the above equation, μ is the solution's dynamic viscosity, ε_s is the permittivity of the electrolyte solution, ζ_w is the zeta potential of the microchannel wall, and $\vec{E} = -\nabla V$ is the strength of the external electric field, where V is the electric potential.

If a spherical particle is brought into the microfluidic channel, a hydrodynamic drag force, also known as the Stokes frictional force, is exerted on the particle because of the relative motion of the particle with regard to the fluid. Given the assumption that the diffusion of the particle is negligible, the formula for the hydrodynamic drag force can be derived by solving the Stokes flow for small Reynolds numbers, which yields (Morgan and Green, 2003):

$$\vec{F}_H = -6\pi\mu a\left(\vec{u}_p - \vec{u}\right), \tag{4.2}$$

where a is the radius of the spherical particle, $\vec{u}_p$ and $\vec{u}$ are the velocities of the particle and the fluid, respectively.

If the particle has surface charges, it also experiences an electrophoretic force. Under the thin EDL assumption, the general expression of the electrophoretic force on a charged particle is written as (Probstein, 1994):

$$\vec{F}_{EP} = 6\pi\zeta_p\varepsilon_s a\vec{E}, \tag{4.3}$$

where ζ_p is the zeta potential of the particle.

If the electric field inside the microfluidic channel is non-uniform, the particle is also subjected to a dielectrophoretic force. Therefore, the total force exerted on a particle inside the microfluidic channel is composed of the hydrodynamic drag force, dielectrophoretic force and electrophoretic force as:

$$\vec{F}_{Total} = \vec{F}_H + \vec{F}_{DEP} + \vec{F}_{EP}. \tag{4.4}$$

The direction of the electroosmotic and the electrophoretic motion is along the direction of the electric field, whereas the dielectrophoretic motion is related to the gradient of the electric field (Eqn. 1.14). Since the magnitude of the DEP force is proportional to the volume of the particle, in a non-uniform electric field, particles of different sizes will be deflected to different trajectories under the combined effects of hydrodynamic, electrophoretic and dielectrophoretic forces.

To characterize the size effects on the particle transport, a two-dimensional finite element model of the system has been constructed. The system consists of four channels (branches) and a middle triangle hurdle as drawn to scale in Fig. 4.1. The electric field inside the microchannels can be described by the Laplace equation:

$$\nabla \cdot (\sigma_i \nabla V) = 0, \tag{4.5}$$

where σ_i represents the electrical conductivities of the electrolyte in the simulation domain.

Furthermore, the electroosmotic flow in the microfluidic sorter is governed by the continuity equation and the Navier-Stokes equation:

$$\nabla \cdot \vec{u} = 0, \tag{4.6a}$$

$$\rho \vec{u} \cdot \nabla \vec{u} = -\nabla \mathrm{P} + \mu \nabla^2 \vec{u}. \tag{4.6b}$$

The slip boundary condition (Eqn. 4.1) is applied at the channel wall.

The above equations are numerically solved subject to $V1 = 120\,V,\ V2 = 110\,V,$ $V3 = 10\,V,\ V4 = 20\,V$ and $\zeta_w = -40\,mV$ using the finite element package Comsol Multiphysics 3.3 (Comsol, Inc.). Fig. 4.1a plots the distribution of electric potential (surface), the electric field (contours: equal magnitude lines) and direction of the electric field (streamline: electric field direction). Fig. 4.1b is the zoom-in view of the electric field, in which the arrows represent the minus gradient of the square of the magnitude of the electric field intensity around the triangle hurdle. Simulation results indicate that at the hurdle, the electric field intensity is strongly non-uniform and the gradient of the square of the magnitude of the electric field intensity is significant near the hurdle, which will generate sensible DEP force in the direction perpendicular to the hurdle surface.

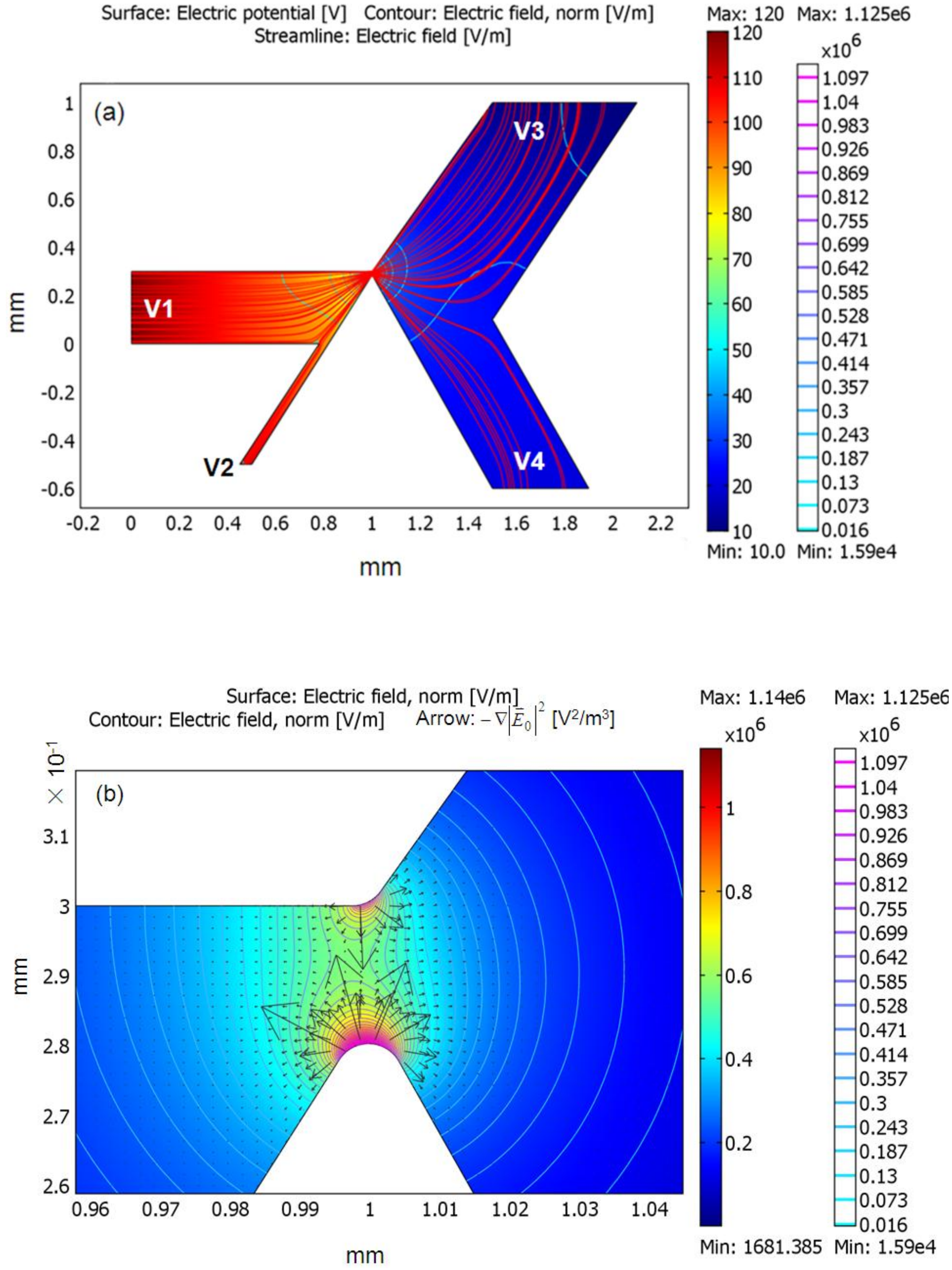

Figure 4.1: (a) Distribution of the electric potential (surface), the electric field (contours: equal magnitude lines) and the direction of the electric field (streamlines) inside the microfluidic channels; (b) Zoom-in view of the electric field around the triangle hurdle. The arrows represent the minus gradient of the square of the magnitude of the electric field intensity, $-\nabla|\vec{E}_0|^2$, which reaches maximum values on the hurdle surface.

For a spherical particle inside the microfluidic sorter, the motion of the particle is simulated based on the Lagrangian tracking method. That is, the trajectory of the charged particle is predicted by integrating the force balance on the particle, governed by the following equation (Kang et. al., 2006):

$$m\frac{d\vec{u}_p}{dt} = \vec{F}_{Total}\,, \tag{4.7}$$

where $\vec{F}_{Total}$ is given by Eqn. (4.4).

The spherical particle is first fed into the microfluidic sorter through branch V2 and driven toward the triangle insulating hurdle by electroosmotic flow. The gradient of the electric field intensity in the branch V2 and V1 is very small so the DEP effect is negligible before the particle traverses the hurdle. When the particle moves close to the hurdle, it experiences strong DEP force generated by the highly non-uniform electric field. The induced DEP force points towards the minus gradient of the square of the magnitude of the electric field intensity so it will repulse the particle away from the gradient maximum on the hurdle surface. Because the magnitude of the DEP force depends on the size of the particle, bigger particles experience larger DEP force and tend to be pushed further away than smaller ones. Therefore, different size particles will be deflected to different streams after they traverse the hurdle. The particle separation can be further optimized by adjusting the voltages applied to the well V3 and V4. The trajectories of six particles ($\zeta_p = -15\,mV$) ranging from 1 μm to 6 μm in diameter with the same initial position has been predicted via Lagrangian tracking method and solved numerically using the Fluent$^{®}$ software (ANSYS, Inc.) (Fig. 4.2). It can be seen that clear trajectory separation between particles occurs after they pass through the hurdle.

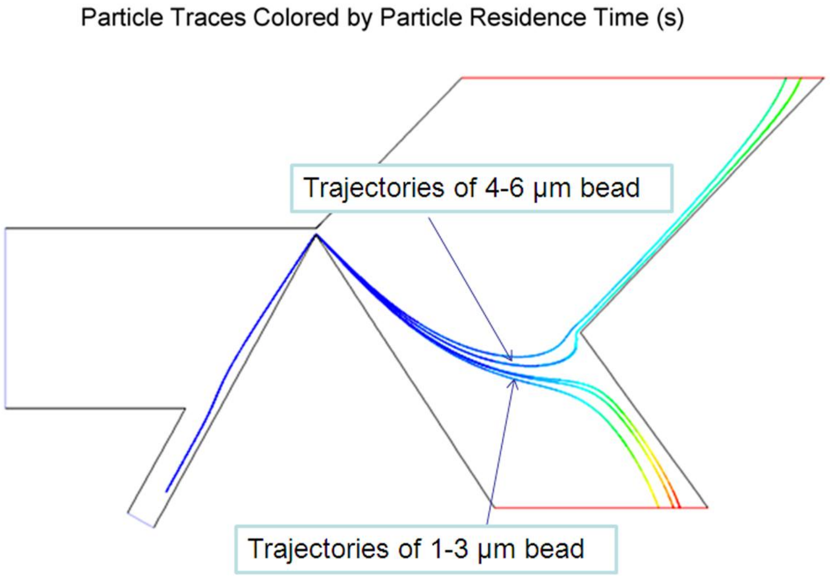

Figure 4.2: The trajectories of six particles ranging from 1 μm to 6 μm initiated from the same initial position.

Experimental Methods

Microfluidic Device Design

The design of the microfluidic device for simultaneous on-chip cell separation and characterization, composed of a separation fluidic circuit and a characterization circuit, is depicted in Fig. 4.3. The device is fabricated with PDMS microchannels bonded to a glass substrate (Fig. 4.4). The whole device contains eight branches connected to eight wells (all 4 mm in diameter).

In the separation circuit, the well V1 contains pure driving buffer while the well V2 is filled with buffer containing a binary mixture of different size beads, yeast colony, or tumor and bone marrow cells. The dimension of the horizontal driving microchannel (branch V1) and the tilted input channel (branch V2) are 5.5 mm long and 300 μm wide, and 3.5 mm long and 60 μm wide, respectively. A 60 degree triangle insulating hurdle is sandwiched between the upstream branches (branch V1 and branch V2) and the middle stream branches (branch V3' and branch V4'). The narrowest gap between the microchannel wall and the tip of the hurdle is 20 µm. The lower tilted branch V4' is 1.5 mm long and 300 µm wide while the upper tilted branch V3' is 1.5 mm long and 450 µm wide. The branch V3' (or V4') is connected to a vertical channel of 100 µm wide, which is connected to the horizontal microfluidic circuit for size characterization.

The characterization circuit consists of a pair of mirror-symmetric microfluidic circuits. Each characterization circuit is similar to a MOSFET-based microfluidic Coulter counter with two large microchannels sandwiching a small sensing channel (50 µm long and 15 µm wide). For each characterization circuit, a vertical microchannel (4 mm long and 110 µm wide) connects the downstream end of the sensing channel to the gate of a MOSFET (through Well V5 and well V6). The well V3 is 1.5 mm above the horizontal channel (branch V3), which provides an additional port to set the electrical potential in the fluidic circuit. The tilted connection branch between well V3 and the horizontal channel is 2 mm long and 800 µm wide. The horizontal branch V7 is 6 mm long and 500 µm wide. All channels are 15 µm in depth. The characterization circuit works exactly as described in Chapter II for the yeast cell volume growth measurement.

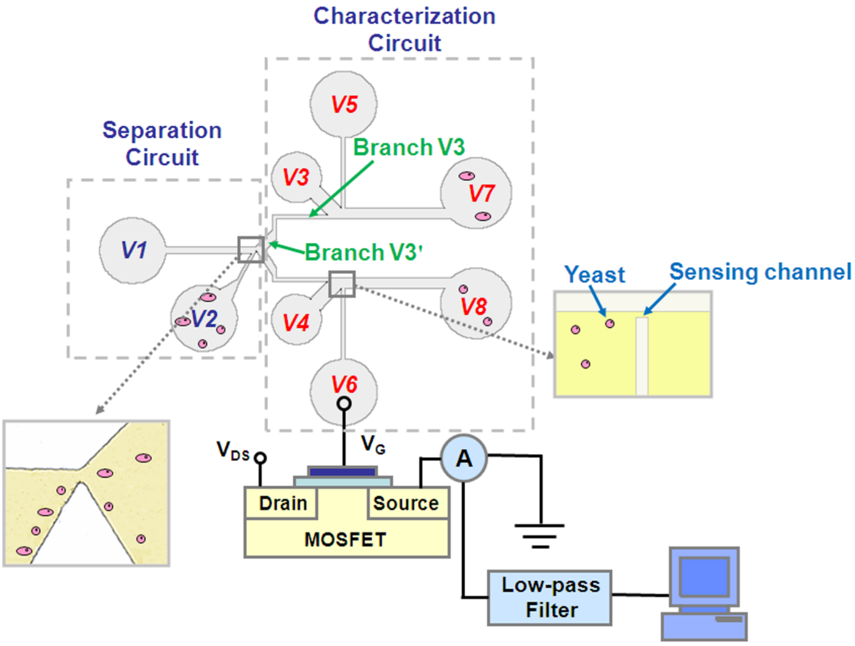

Figure 4.3: A schematic of the microfluidic device layout with integrated DEP separation and resistive-pulse sensing characterization circuits.

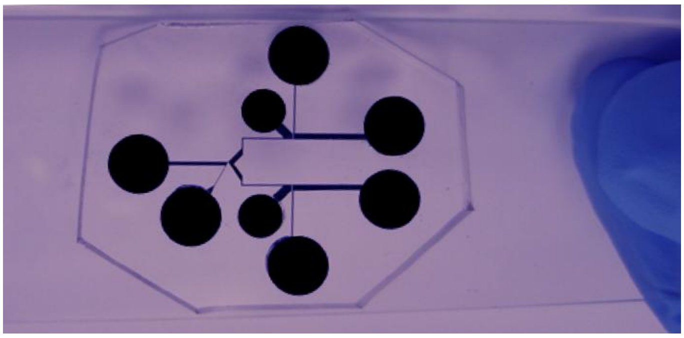

Figure 4.4: A picture of the microfluidic device that enables simultaneously size-based cell separation and characterization.

Experimental Procedure

In the experiment, the buffer solution (composed of 10 mM sodium chloride and 10 mM phosphate, pH 7.2) was first loaded into the eight wells of the microfluidic device. Platinum electrodes were submerged into each well to connect the fluidic circuits to the external electronic circuit. Binary mixtures of polystyrene beads (1.97

μm and 4.84 μm in diameter) or yeast colony with a concentration of 1-5 $\times 10^6$ particles or cells/mL were then loaded into well V2. Two high-voltage DC power supplies (Keithley 6487, Keithley Instruments Inc.) were used to provide 120 V and 110 V voltages to well V1 and well V2 in order to introduce electroosmotic flow to drive the bead/cell mixture through the separation circuit. Two relatively low voltages were applied to well V3 (10 V) and V4 (20 V) by another two power supplies (Agilent E-3612A, Agilent Technologies). An additional power supply (Agilent E-3617A, Agilent Technologies) was used to supply a constant source-drain bias (0.15 V) to induce the MOSFET drain current. A negative voltage ranging from -8 V to -18 V was applied to well V7 or V8 to ensure that the MOSFET (2N7000 N-channel FET, Fairchild Semiconductor) works in the sub-threshold regime. The MOSFET drain current was measured by a current preamplifier (Keithley 428, Keithley Instruments Inc.). The measured drain current was passed through a low-pass filter (SR 560, Stanford Research Systems) with a cut-off frequency of 100 Hz followed by a 50/60 Hz noise eliminator (Hum bug noise eliminator, Quest Scientific Instruments Inc.) before it was fed into the digital data acquisition system. The fluidic and MOSFET circuits were commonly grounded. In some experiments, the particle motion was monitored using an inverted optical microscope (Nikon Eclipse TE-2000U, Nikon Corp.) and recorded by a CCD camera (Nikon digital sight DS-U1, Nikon Corp.). The frame rate was set to be 9.8 frames per second.

Results and Discussions

The microfluidic device for simultaneous sized-based DC DEP cell separation and characterization have been used to sort different sized polystyrene beads, yeast cells, and 4T1 breast cancer cells and bone marrow cells. The results and related discussions are presented in this section.

Separation and Characterization of Polystyrene beads

As discussed in the previous section, microbeads under a non-uniform electric field experience dielectrophoretic force whose magnitude is related to the bead size. Larger beads would be deflected more than smaller ones, which can be used to realize size-based DC DEP separation. Experiments showed that after the mixture of 1.97 μm and 4.84 μm diameter polystyrene beads flowed through the narrow gap between the hurdle and the channel wall, the single stream of beads mixture was divided into several streams. In agreement with the theoretical prediction, the streams moved upward into branch V3' contained 4.84 μm beads, whereas the streams moved downward into branch V4' contained 1.97 μm beads. The trajectories of the moving beads were obtained by superimposing multiple consecutive image frames within 1 minute using Adobe Photoshop CS3 (Adobe Systems) (Fig. 4.5). As shown in Fig. 4.5, most 4.84 μm polystyrene beads moved into branch V3 while most 1.97 μm polystyrene beads moved into branch V4. The separation was conducted at different bead flow rates. Fig. 4.5a depicts a relatively high bead flow rate DEP separation with an average count of 0.778 beads/sec, and Fig. 4.5b depicts a low bead flow rate separation with an average count of 0.485 beads/sec. The DEP separation at different bead flow rates was achieved by altering the bead concentration in the binary beads mixture. We performed the separation at different bead flow rates because bead-bead interaction between two nearby dielectric beads could give rise to an attraction force, resulting in undesirable bead deflection and degraded the separation performance (Choi and Park, 2005).

In the experiment, the separation efficiency (purity of each separated streams) was simultaneously determined by a pair of integrated MOSFET-based microfluidic Coulter counters. Fig. 4.6 shows snapshots of the measured MOSFET drain current of the upper (Fig. 4.6a) and lower sensing channels (Fig. 4.6b) as a function of time. As can be seen from Fig. 4.6, in each stream of the separated 4.84 μm (or 1.97 μm) beads, there are a small number of 1.97 μm (or 4.84 μm) beads presented, indicating that the separation is not 100%. By counting the number of 1.97 μm and 4.84 μm beads that translocated through each sensing channel, the separation efficiency or purity of the separated beads can be obtained, as summarized in Table 4.1. The measured separation efficiency provides an accurate quantitative characterization of the performance of the microfluidic sorter.

Table 4.1 The separation efficiency of the microfluidic sorter determined by the integrated MOSFET-based microfluidic Coulter counter.

	High flow rate (0.778 beads/sec)		**Low flow rate (0.485 beads/sec)**	
	Upper	**Lower**	**Upper**	**Lower**
Time (s)	1500	570	2550	810
# of 4.84 μm beads	288	7	257	306
# of 1.97 μm beads	35	314	7	3
Purity (%)	**89.16**	**97.82**	**97.35**	**99.03**

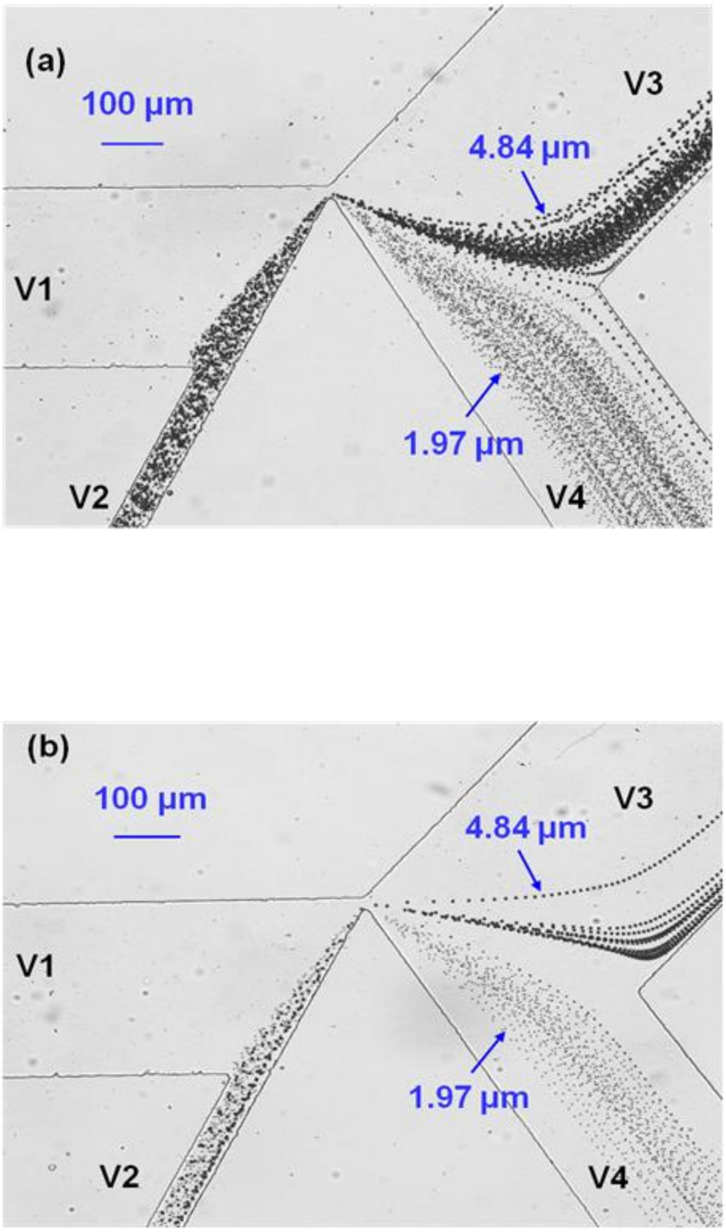

Figure 4.5: The microparticle separation images from superimposing 1 minute consecutive images of the moving beads under the same experimental conditions. (a) High bead flow rate separation of 1.97 µm and 4.84 µm in diameter polystyrene beads mixture; and (b) Low bead flow rate separation.

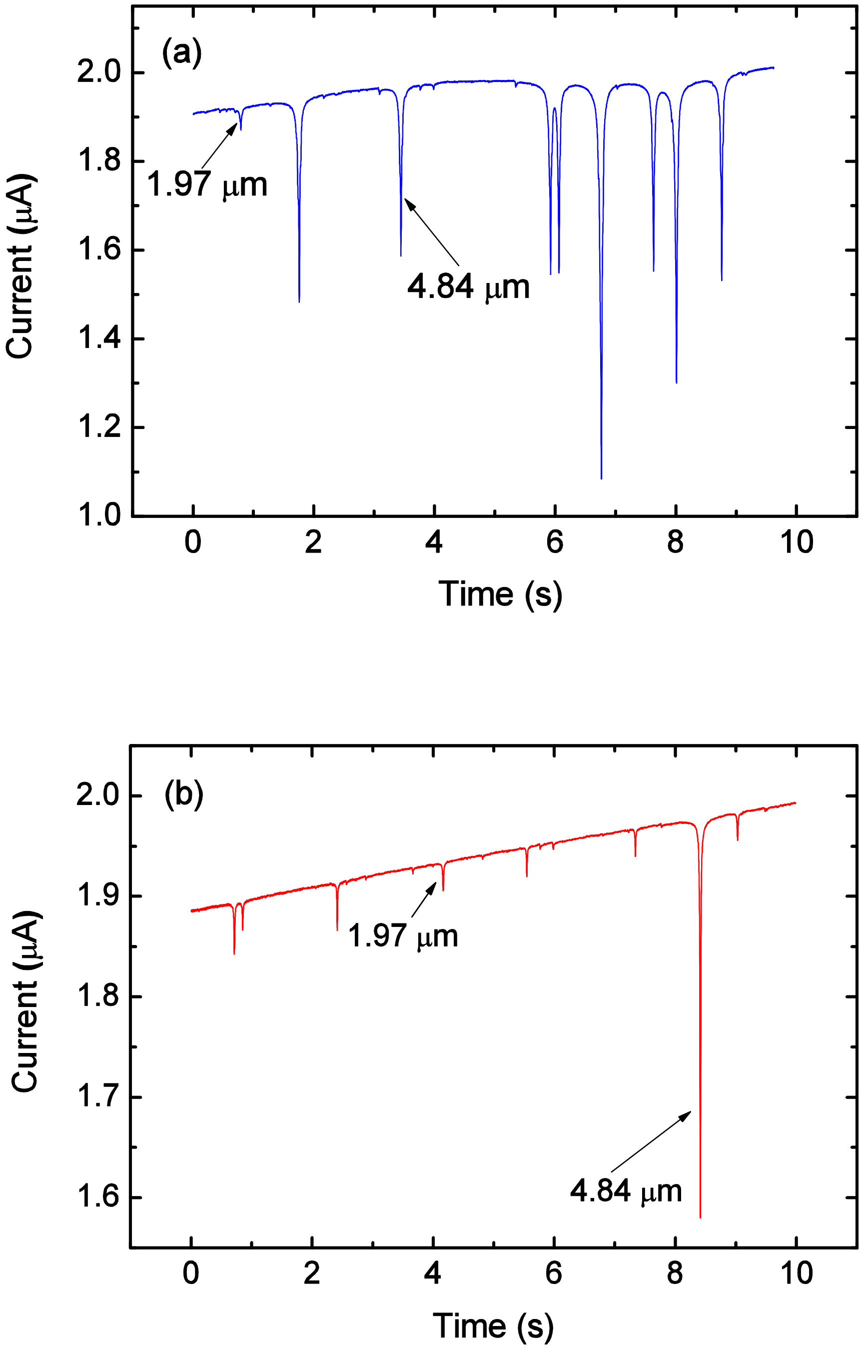

Figure 4.6: (a) The MOSFET drain current of the upper sensing channel containing mostly 4.84 μm polystyrene beads (with one 1.97 μm bead); (b) The MOSFET drain current of the lower sensing channel containing mostly 1.97 μm polystyrene beads (with one 4.84 μm bead).

Separation and Characterization of Yeast Cells

As demonstrated in the above section and in the literature, DEP-based microfluidic sorters can separate microparticles according to their size (Kang et al., 2006; Kralj et al., 2006). However, the experimental objects used in these studies were either a binary mixture of beads or two different types of cells, which had a significant size difference. Real biological samples often contain cells of continuous size distribution. To test the performance of the microfluidic DC DEP sorters in separating these more complex samples, we performed separation of yeast cells with a continuous size distribution (S. cerevisiae strain CEN.PK 113-7D) under three different cell flow rates (0.37 cells/sec, 0.9 cells/sec, and 1.79 cells/sec) by adjusting the cell concentration.

Under the same experimental condition, the trajectories of yeast cells separated at different cell flow rates were obtained by superimposing 30 seconds consecutive images, as seen in Fig. 4.7 (a-c). At low flow rate (0.37 cells/sec), we observed that the single stream of yeast cells was split into several after traversing the PDMS hurdle. Almost all the cells deflected into the upper branch were larger than those into the lower branch. As the cell flow rate increases, we noticed that some small cells were diverted up, and some large ones were diverted down at the same time after translocating the DEP separation region. This indicates that as the cell flow rate increases, interactions between neighboring cells near the PDMS hurdle could affect the DEP force and lead to more complex cell trajectories, which result in degraded separation performance.

After being separated by the DEP force, the deflected cells entered the characterization circuit consisted of small sensing channels, in which the MOSFET-based resistive-pulse sensing was used to measure the volume of the separated cells.

Similar to that described in Chapter II, calibration of the sensing channel was done with more than two hundred of 4.84 μm diameter polystyrene beads to obtain a reference MOSFET drain current modulation, which was then used to extract the absolute volume of cells. Histograms of separated cell volume distributions in both the upper (V5 and V7) and the lower branches (V6 and V8) for different cell flow rates are drawn in Fig. 4.7 (d-f). The snapshots of the measured MOSFET drain current of the upper and lower sensing channels at the flow rate of 0.9 cells/sec are plotted in Fig. 4.8a and Fig. 4.8b, respectively. Statistical results for the separated yeast cells in the upper (V5 and V7) and the lower branches (V6 and V8) at different cell flow rates are listed in Table 4.2. It can be clearly seen from Fig. 4.7 (d-f) that the overlap between the two size distributions in the upper and the lower branches substantially enlarges as the cell flow rate increases from 0.37 cells/sec to 1.79 cells/sec. The average volume of yeast cells in the upper branch first decreases from 80.04 μm^3 to 77.99 μm^3, and then declines to 70.27μm^3, as the flow rate increases from 0.37 cells/sec to 1.79 cells/sec. Meanwhile, the average yeast cell volume in the lower branch increases from 38.32 μm^3 to 44.42 μm^3, and further to 44.77μm^3 in response to the increased cell flow rate (Table 4.2). These results confirm that the separation performance degrades as the cell flow rate increases, similar to what we observed using polystyrene beads.

Table 4.2 The volume of the separated yeast cells in the upper and the lower branches determined by the MOSFET-based microfluidic Coulter counter.

Flow rate	**0.37 cells/sec**		**0.9 cells/sec**		**1.79 cells/sec**	
	Upper	**Lower**	**Upper**	**Lower**	**Upper**	**Lower**
Time (s)	610	610	571	571	315	315
# of yeast cells	138	82	293	218	212	212
Average volume (μm^3)	**80.04**	**38.32**	**77.99**	**44.42**	**70.27**	**44.77**

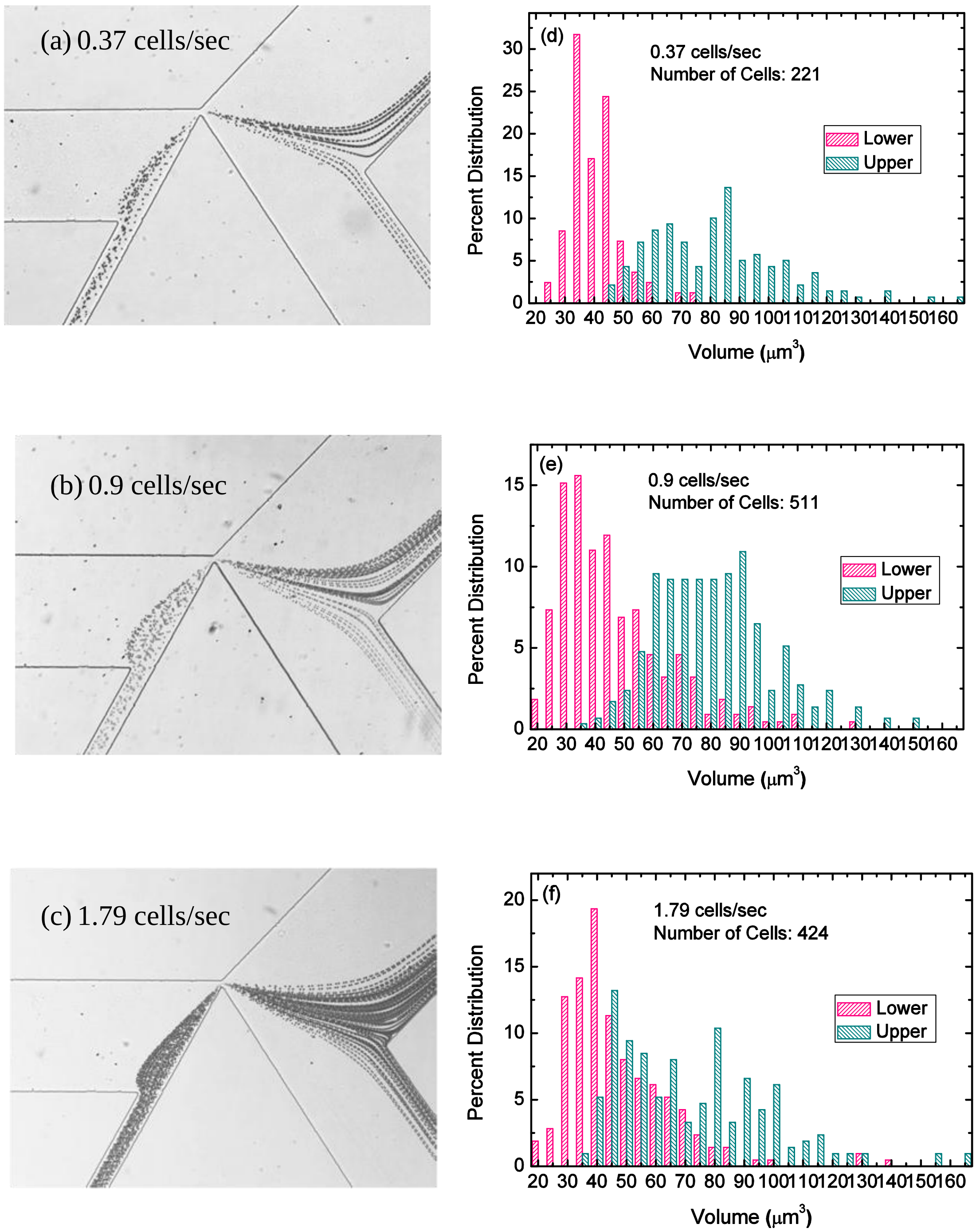

Figure 4.7: Left, (a)-(c) The traces of yeast cells by superimposing 30 seconds consecutive images of moving yeast cells at three different flow rates; Right, (d)-(f) The corresponding histograms of percentage size distribution of yeast cells for the upper branch (V5 and V7) and the lower branch (V6 and V8) after separation.

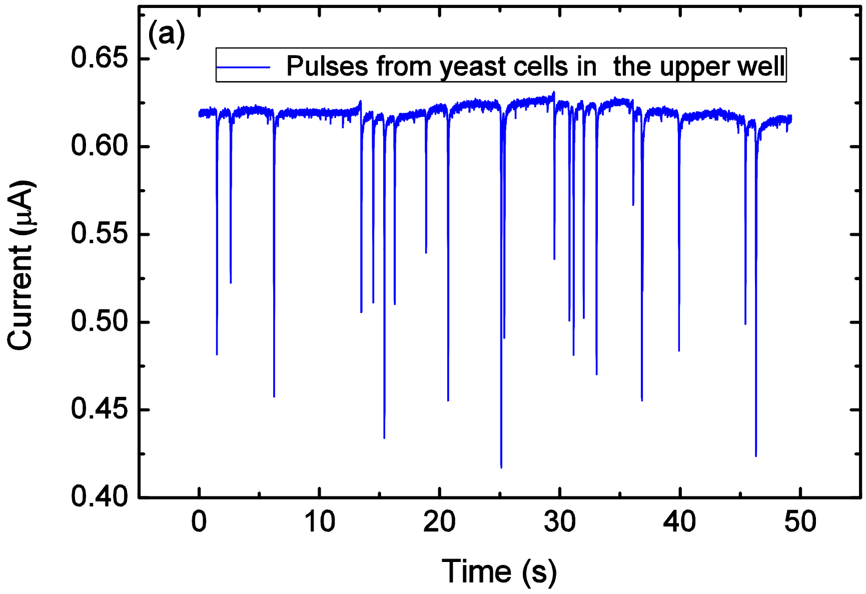

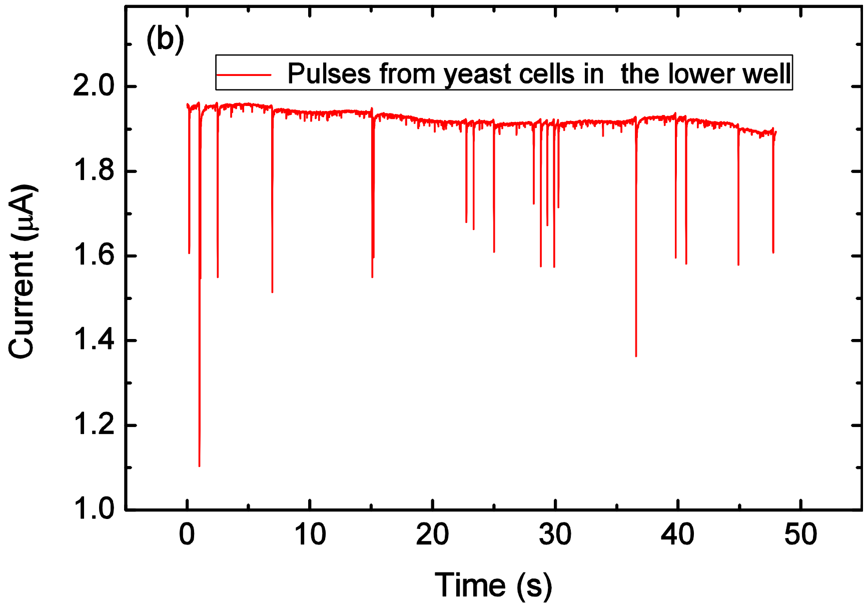

Figure 4.8: (a) The snapshots of the measured MOSFET drain current of the upper sensing channel as a function of time; (b) The snapshots of the measured MOSFET drain current of the lower sensing channel as a function of time.

To further quantitatively analyze the separation performance, we choose the Receiver operator characteristics (ROC) method, which is a powerful technique to analyze the degree of overlap between two populations or distributions. In the current setting we are faced with assessing the degree to which the microfluidic device can separate a single population into two distinct populations with a minimum of overlap. The ROC technique is depicted in Fig. 4.9 and described in numerous sources (Greiner et al., 2000; Hanczar et al., 2010). Briefly, for each choice of a separation threshold one calculates the sensitivity and specificity of that choice. The ordered pair of values (sensitivity, 1-specificity) defines one point on the parametric ROC curve. When two populations are identical then the ROC curve is seen to be the line, $sensitivity + specificity = 1$, or said another way the diagonal in the ROC plane. When two populations are perfectly separated then the ROC is the union of the segments (0, sensitivity) and (1-specificity, 1), where the values of 1-specificity and sensitivity varies monotonically from 0 to 1 as the threshold value passes through its range. Every other pair of distributions lies between these extremes. The area under the ROC curve (AUC) times 2 minus 1, provides a normalized and consistent measure of fractional separation (FS). We have used this measure to characterize the relationship between the flow rate of cells through the DEP based microfluidic sorter and the subsequent degree of separation. Fig. 4.10 shows the ROC curves for the various cell flow rates and the linear relationship between the FS and the cell flow rate. Certainly there is an asymptotic value of separation that becomes independent of cell flow rate below some minimum value, causing the curve to deviate from linearity at low cell flow rate. Similarly, there might be a minimum of separation that is independent of the cell flow rate at high cell flow rates that depends only on the geometry of the device and the gradient of the field at the PDMS hurdle. These considerations would indicate that the true curve that describes the relationship between cell flow rate and fractional separation is a sigmoid.

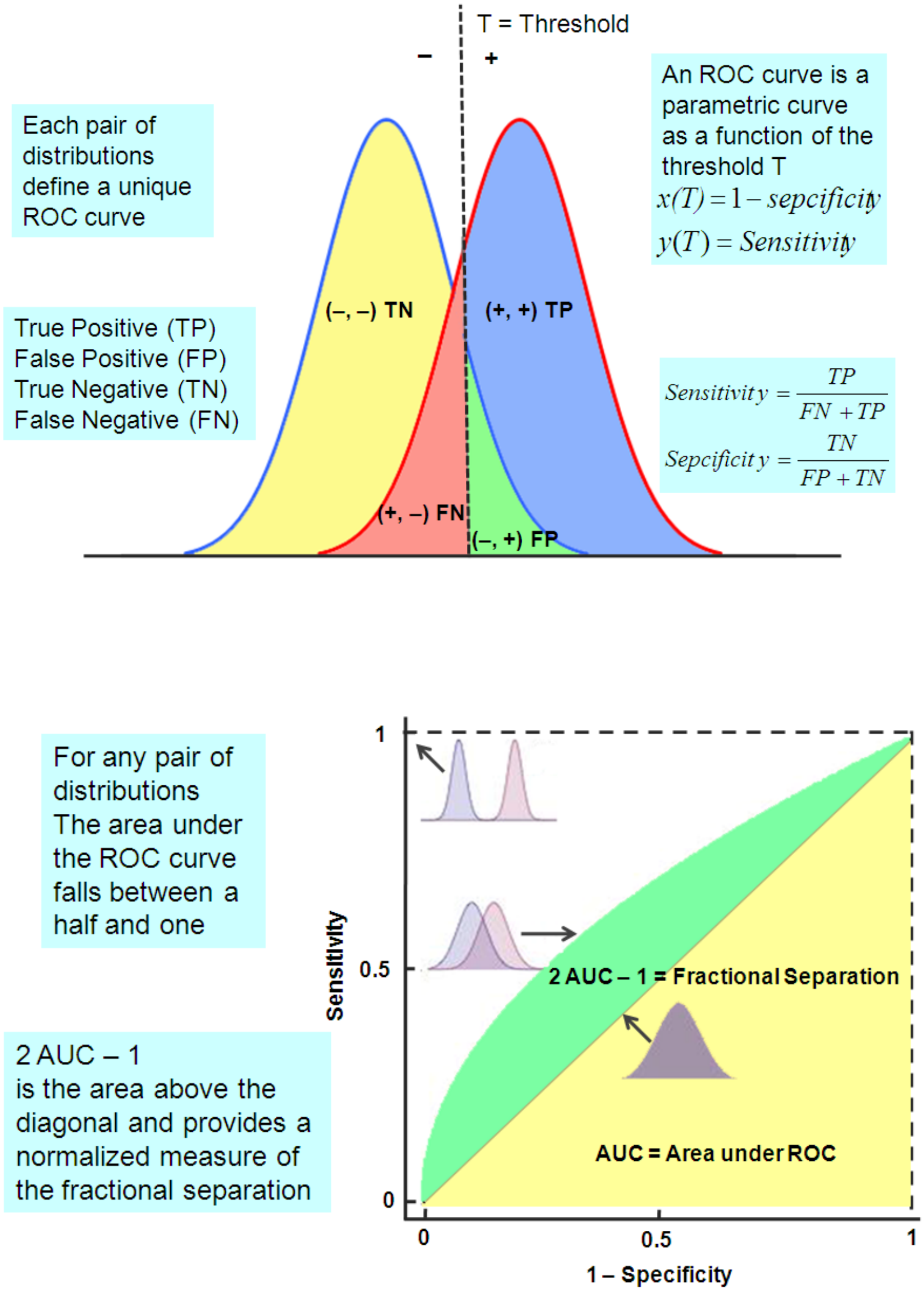

Figure 4.9: Receiver operator characteristics (ROC).

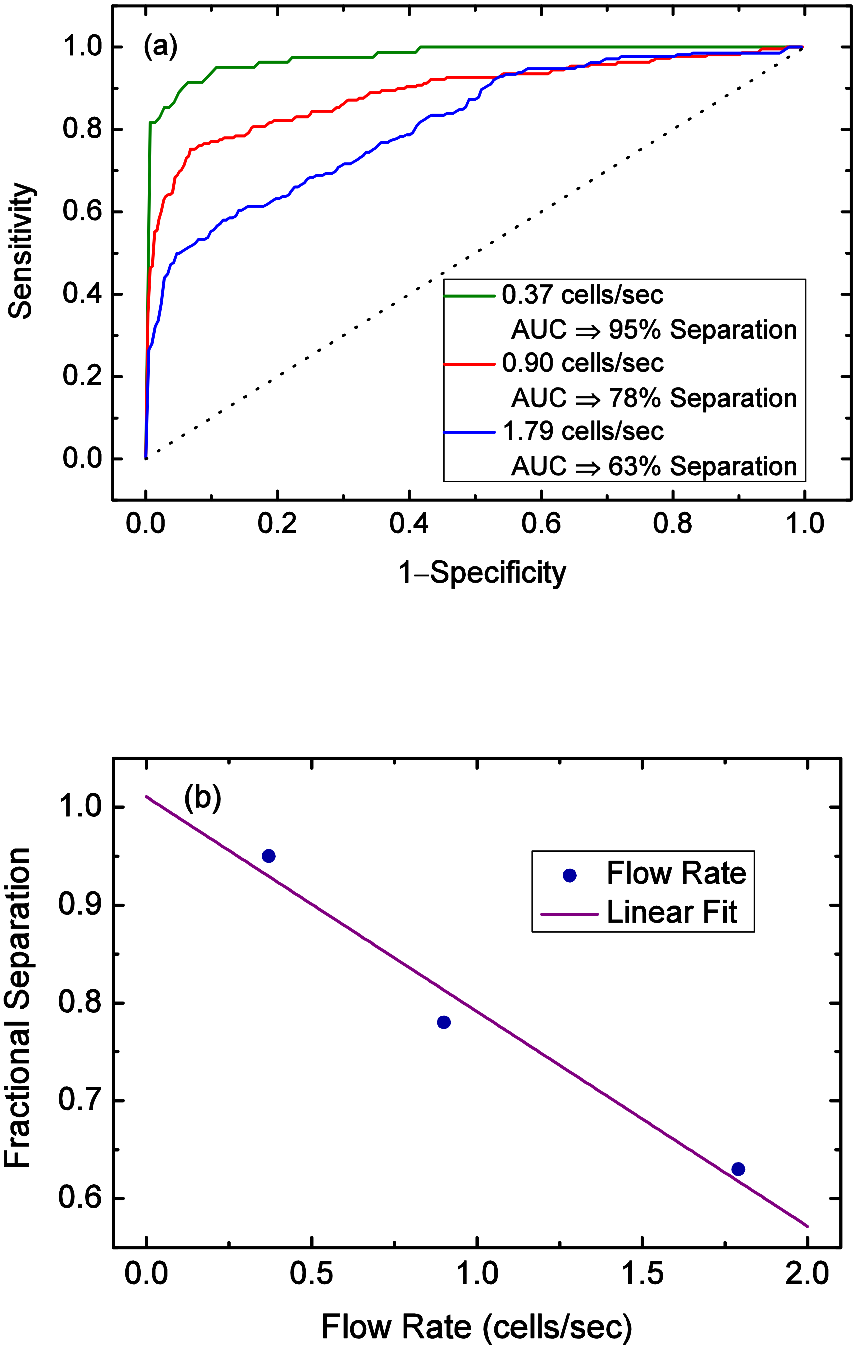

Figure 4.10: (a) The ROC curves for various cell flow rates; (b) The relationship between the FS and the cell flow rate.

Questions can be asked about whether all yeast cells passing through the separation circuit are detected by the sensing circuits and whether the detected size distributions reflect the actual yeast cell size distribution. Therefore, we performed one more experiment to verify that the MOSFET-based resistive-pulse sensing captures the true size distribution of the yeast cells by running a yeast colony from the same yeast culture using only the sensing circuit in one branch without first separate the yeast cells. The results are then compared with the size distribution of the sum of the yeast cells in the upper and lower branches. The histogram of a yeast colony without separation process was obtained by passing 1985 cells through a MOSFET-based microfluidic Coulter counter, and the cell size histogram of separated cells was obtained by summing the separated yeast cells in both the upper and lower branches at three different cell flow rates (Fig. 4.11). These two well-matched distributions suggest that the sensing circuit faithfully captured the size distribution of the separated cells.

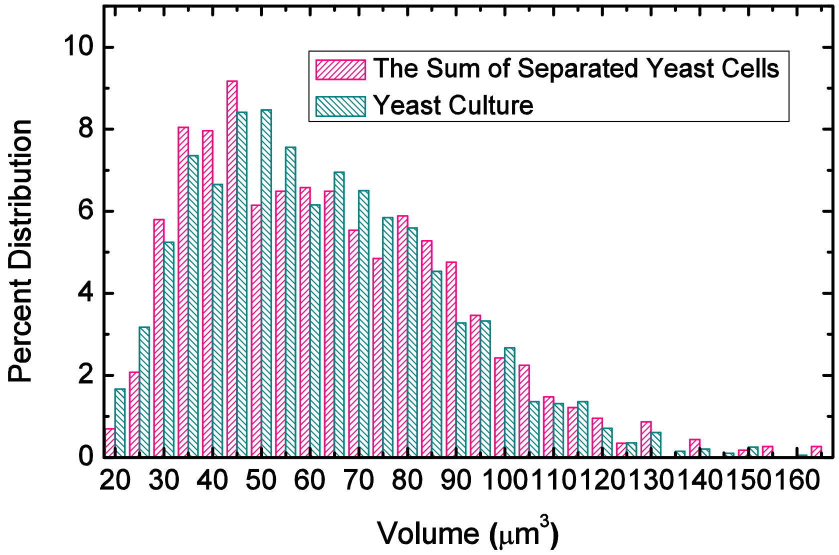

Figure 4.11: The percentage size distribution of the sum of separated yeast cells compared with that of a whole yeast culture.

Separation and Characterization of 4T1 Breast Cancer Cells and Bone Marrow Cells

To demonstrate that the above described separation and characterization techniques can also be applied to mammalian cells, we tried to separate the mixture of two different mammalian cells – breast cancer cells (4T1) and murine bone marrow cells, and characterize the separation performance. In this case, due to the larger size of the cancer cells, the DEP separation region is enlarged (the narrowest gap between the hurdle and channel wall is 30 μm × 30 μm for length and width) as well as the sensing channel (30 μm × 30 μm × 50 μm for width, depth and length, respectively). In addition, the shape of the PDMS hurdle at the upstream side is designed to be an arc to ensure that cells enter the DEP separation region from approximately the same initial position. Experiments showed that the separation of 4T1 and bone marrow cells could be achieved at applied voltages of 150 V to well V1, 100 V to well V2, 15.1 V to well V3, 34.7 V to well V4, -12.51 V to well V7 and -66.2 V to well V8. The size of separated cells was determined based on a calibration test of more than 200 of 9.77 μm beads.

Fig. 4.12a shows the traces of the cancer and bone marrow cells from superposing 5.7 sec consecutive images. As expected, the cancer cells, of larger sizes than the bone marrow cells, are deflected into the upper separation branch. On the other hand, the bone marrow cells flow into the lower branch. It should be noted that after separation, an overlap in the size range of 9-13 μm was observed, as shown in the histogram of percentage size distributions for the upper and lower branches (Fig. 4.12b). The ROC separation analysis gives an 87% separation (Fig. 4.13). It is worth noting that the separation is performed at a relatively high cell flow rate since the mammalian cells tend to deposit on the substrate surface if the flow speed is low.

This could be the reason that the separation performance is only 87%. However, one more reason could be that the bone marrow cells tend to stick to the cancer cells, and pose more challenge to better separation.

To further examine the separation performance, we counted the number of 4T1 and bone marrow cells using optical microscopy in well V7 and V8, which gave 61 4T1 cells and 8 bone marrow cells in the upper well (Fig. 4.14a), and 26 bone marrow cells and 2 4T1 cells in the lower well (Fig. 4.14b).

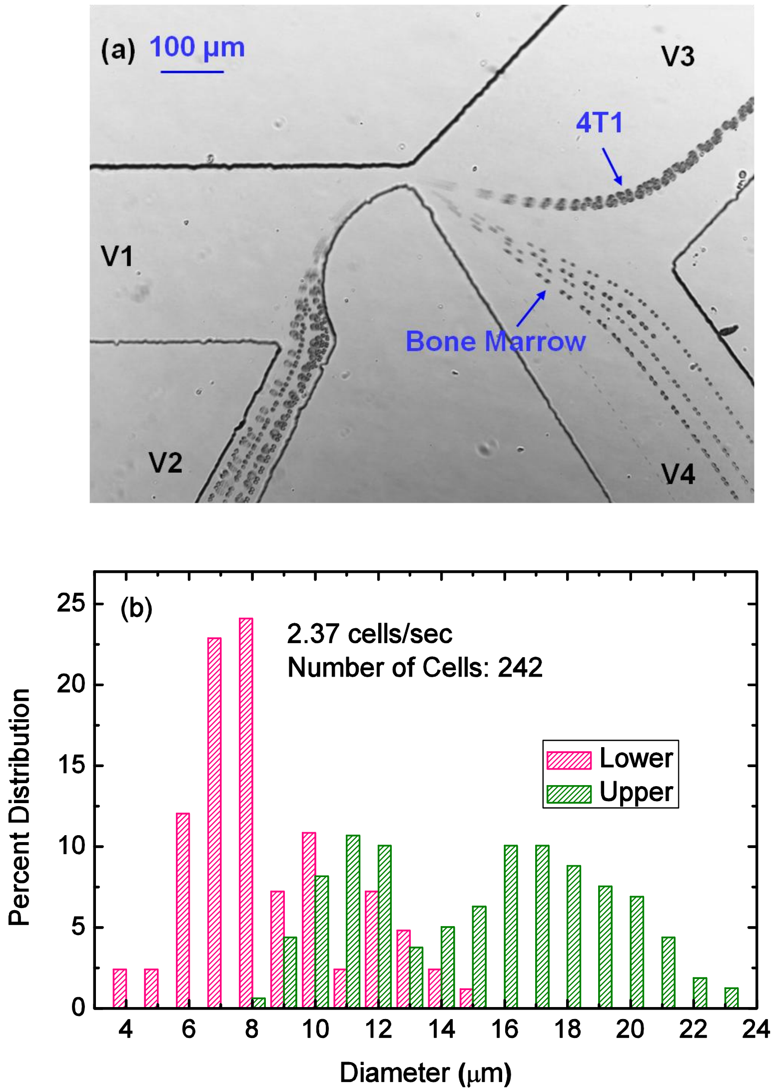

Figure 4.12: (a) The traces of 4T1 breast cancer cells and bone marrow cells from superimposing 5.7 sec consecutive images of the moving cells; (b) The histograms of percentage size distribution for the upper and lower branches.

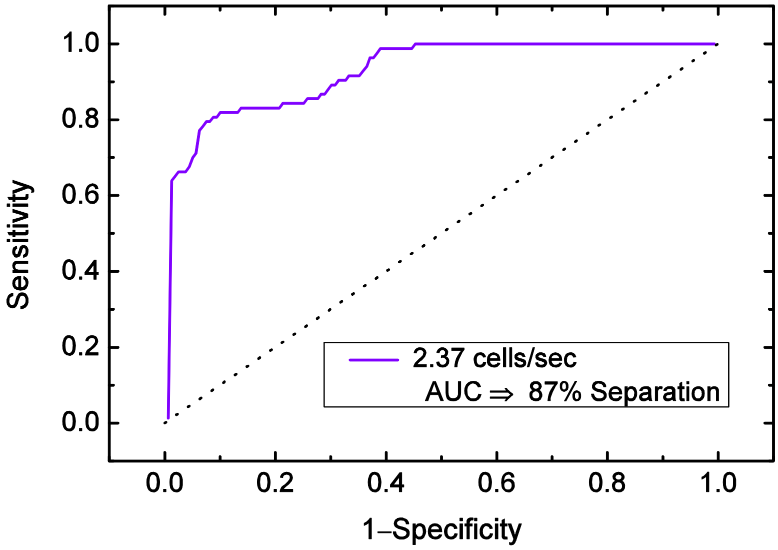

Figure 4.13: The ROC separation curve for 4T1 and bone marrow cells, indicating an 87% fractional separation.

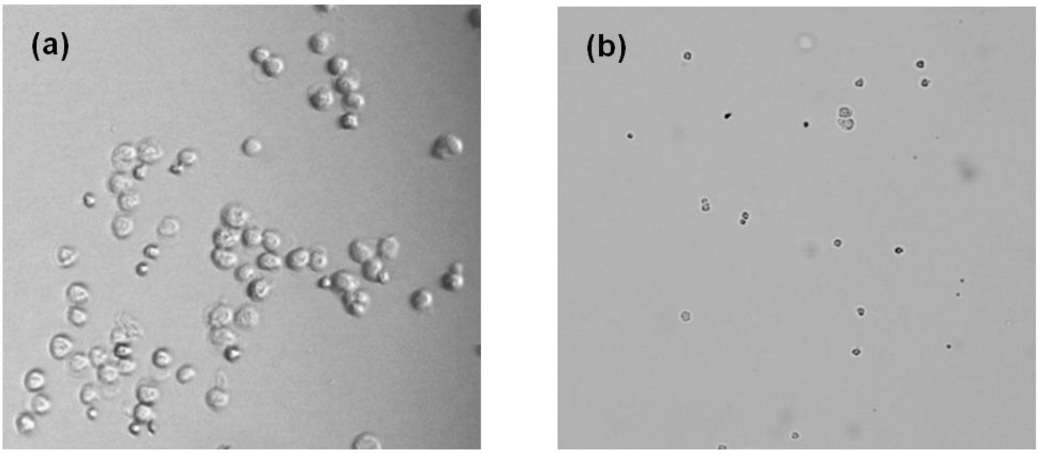

Figure 4.14: (a) Optical image of cells in the upper well V7; (b) Optical image of cells in the lower well V8.

Summary

We have characterized the separation performance of microfluidic DC DEP sorters under different conditions with integrated on-chip MOSFET-based Coulter counters. In general, the performance of DC DEP separation of different sized particles or cells depends on the flow rate of particles or cells through the separation region. Through quantitative characterization, we conclude that at low particle/cell flow rates, there is less interference to the DEP field from other particles or cells and the separation efficiency is better. However, as the flow rate increases, the chance for multiple particles or cells exist in the DEP cell separation region increases, which will interfere the interaction between the particles or cells and the DEP field; and therefore, degrade the separation performance.

The same trend is observed for all different size polystyrene beads, yeast colony with continuous size distribution, and 4T1 breast cancer cells and murine bone marrow cells. For cells with a continuum size distribution, the Receiver operator characteristics method is used to extract a quantitative separation performance. For yeast cells, it is shown that within a cell flow rate regime from 0.37 to 1.79 cells/sec, the fractional separation correlates with the cell flow rate in an approximately linear manner with degraded performance for higher cell flow rates.

CHAPTER V

CONCLUSIONS AND FUTURE WORK

This dissertation presents the development of two microfluidic resistance sensing schemes and demonstrates their applications: (1) to measure the volume growth rate of single budding yeast cells; and (2) to characterize the performance of size-based on-chip DC dielectrophoretic cell separation.

The first sensing scheme is based on the MOSFET-based microfluidic resistive-pulse sensing, which amplifies the percentage modulation of the resistance modulation of the sensing microchannel when microparticles or cells are translocated through it. This dissertation demonstrates that the percentage modulation of the MOSFET drain current is independent of the baseline MOSFET drain current if the MOSFET works in the sub-threshold regime. More importantly, selected single cells can be moved back and forth through the sensing aperture electrokinetically to allow for a long term measurement of the cell volume growth rate. Analysis shows that any side effects of the applied electrical field on cell growth have been reduced as much as possible in the carefully designed operational protocol. Measurements of ten individual budding yeast cells show that their volume growth follows a sigmoid profile with lower growth rate at the initial (before the bud emerges) and the final (after the daughter cell matures) stages of the cell cycle. Analysis of the data strongly suggests a local exponential volume growth phenomenon, while globally the growth phenomena can be represented by several models including piecewise linear, and two non-linear functions.

Because of the time needed to switch the flow direction and to minimize the exposure of cells to the relatively strong electric field in the small sensing channel, the

MOSFET-based resistive-pulse sensing scheme can only measure cell volume growth at discrete time points with relatively large time intervals (10~20 minutes). In order to realize continuous measurement, a reference-channel based resistance sensing scheme has been developed. This novel design of a dual-channel system consists of a sensing channel and a reference channel aligned in a serial manner. The introduction of the reference channel allows for cancellation of the effects of baseline ionic current drift, which always exists in microfluidic devices. The same ionic current flows through both the sensing and the reference channel; and therefore, the ratio of the voltage drops across the two channels is only related to the electrical resistance ratio between the two channels. When a single cell stays inside the sensing channel, the cell volume change can be continuously recorded in a real-time manner by monitoring the ratio of the voltage drop across the sensing and the reference channels. Based on the measured resistance ratio, the volume change of the cell as it grows or in response to the varying microenvironmental conditions can be derived, as demonstrated with the measured real-time volume growth rate of single yeast cells.

To further demonstrate the applications of the developed sensing schemes and the possibility of integrating them with other on-chip analytical functions, the MOSFET-based resistive-pulse sensing scheme is integrated with a direct current dielectrophoretic (DC DEP) cell separation scheme to characterize the separation performance. Microfluidic cell separation technique is essential for many lab-on-a-chip assays to isolate distinct cell types for further analysis. However, to date, the development of microfluidic cell separation techniques mainly focuses on the separation scheme without paying much attention to careful characterization of the separation performance. Combining the MOSFET-based resistive-pulse sensing scheme with the DC DEP size-based separation technique, simultaneous on-chip microparticle/cell separation and characterization can be achieved. Results from different sized polystyrene beads, yeast colony, and 4T1 breast cancer cells and bone marrow cells indicate that the separation performance depends on the particle/cell flow rate, which provides insights into better separation results.

This dissertation demonstrates the sensing scheme and their potential applications. Future efforts based on the research presented in this dissertation include: (1) Integration of cell trapping technology with the reference-channel based sensing scheme. The presented research has proven that the reference-channel based sensing scheme works; however, it is very challenging to place a single cell into the sensing channel. Therefore, adding a cell trapping mechanism to facilitate cell placement will be necessary for extensive applications of this technology; (2) Applications of the reference-channel based sensing scheme to mammalian cells such as to study the volume change of kidney cells in response to their microenvironment alteration; (3) Integrate the MOSFET-based microfluidic Coulter counter with other microfluidic cell sorters to characterize their performance, and provide insights into better design and operation.

REFERENCES

Ackerman, G. A. and Knouff, R. A. (1959), 'Lymphocytopoiesis in the bursa of Fabricius', *Am J Anat,* 104, 163-205.

Anderson, J. A., et al. (1992), 'Functional expression of a probable Arabidopsis thaliana potassium channel in Saccharomyces cerevisiae', *Proc Natl Acad Sci U S A,* 89 (9), 3736-40.

Ateya, D. A., et al. (2005), 'Volume cytometry: microfluidic sensor for high-throughput screening in real time', *Anal Chem,* 77 (5), 1290-4.

Barbulovic-Nad, I., et al. (2006), 'DC-dielectrophoretic separation of microparticles using an oil droplet obstacle', *Lab on a Chip,* 6 (2), 274-79.

Baumstarkkhan, C., Rink, H., and Zimmermann, H. P. (1986), 'Radiation-Induced Formation of Giant-Cells in Saccharomyces-Uvarum .3. Effect of X-Rays on Nuclear Division', *Radiation and Environmental Biophysics,* 25 (1), 23-30.

Bayley, H. and Martin, C. R. (2000), 'Resistive-pulse sensing - From microbes to molecules', *Chemical Reviews,* 100 (7), 2575-94.

Bayley, H. and Cremer, P. S. (2001), 'Stochastic sensors inspired by biology', *Nature,* 413 (6852), 226-30.

Bayne-Jones, S. and Adolph, E. F. (1932), 'Growth in size of micro-organisms measured from motion pictures', *J Cell Comp Physiol,* 1, 387-407.

Becker, F. F., et al. (1995), 'Separation of human breast cancer cells from blood by differential dielectric affinity', *Proc. Natl. Acad. Sci. USA,* 860-864.

Berge, L. I., Feder, J., and Jossang, T. (1989), 'A Novel Method to Study Single-Particle Dynamics by the Resistive Pulse Technique', *Review of Scientific Instruments,* 60 (8), 2756-63.

Bezrukov, S. M., Vodyanoy, I., and Parsegian, V. A. (1994), 'Counting Polymers Moving through a Single-Ion Channel', *Nature,* 370 (6487), 279-81.

Bitterman, K. J., Medvedik, O., and Sinclair, D. A. (2003), 'Longevity regulation in Saccharomyces cerevisiae: Linking metabolism, genome stability, and heterochromatin', *Microbiology and Molecular Biology Reviews,* 67 (3), 376-99.

Blow, J. Julian (1996), *Eukaryotic DNA replication* (Frontiers in molecular biology 15; Oxford ; New York: IRL Press) xix, 232 p.

Boczko, Erik M., et al. (2010), 'ODE, RDE and SDE models of cell cycle dynamics and clustering in yeast', *Journal of Biological Dynamics,* 4, 328-45.

Bonner, W. A., et al. (1972), 'Fluorescence activated cell sorting', *Review of Scientific Instruments,* 43 (3), 404-9.

Brejning, J., Arneborg, N., and Jespersen, L. (2005), 'Identification of genes and proteins induced during the lag and early exponential phase of lager brewing yeasts', *Journal of Applied Microbiology,* 98 (2), 261-71.

Brewer, B. J., Chlebowicz-Sledziewska, E., and Fangman, W. L. (1984), 'Cell cycle phases in the unequal mother/daughter cell cycles of Saccharomyces cerevisiae', *Mol Cell Biol,* 4 (11), 2529-31.

Butler, L. M., et al. (2001), 'Inhibition of transformed cell growth and induction of cellular differentiation by pyroxamide, an inhibitor of histone deacetylase', *Clin Cancer Res,* 7 (4), 962-70.

Carbonaro, A. and Sohn, L. L. (2005), 'A resistive-pulse sensor chip for multianalyte immunoassays', *Lab on a Chip,* 5 (10), 1155-60.

Cen, E. G., et al. (2004), 'A combined dielectrophoresis, traveling wave dielectrophoresis and electrorotation microchip for the manipulation and characterization of human malignant cells', *J. Microbiol. Methods.,* 58 (3), 387-401.

Chang H, Kosari F, Andreadakis G, Alam MA, Vasmatzis G, Bashir R. 2004. DNA-mediated fluctuations in ionic current through silicon oxide nanopore channels. *Nano Lett* 4:1551-6

Chen, P., et al. (2004a), 'Atomic layer deposition to fine-tune the surface properties and diameters of fabricated nanopores', *Nano Letters,* 4 (7), 1333-37.

--- (2004b), 'Probing single DNA molecule transport using fabricated nanopores', *Nano Letters,* 4 (11), 2293-98.

Chen, H., et al. (2004c), 'Tyrosol is a quorum-sensing molecule in Candida albicans', *Proceedings of the National Academy of Sciences of the United States of America,* 101 (14), 5048-52.

Choi, S. and Park, J. K. (2005), 'Microfluidic system for dielectrophoretic separation based on a trapezoidal electrode array', *Lab Chip,* 5 (10), 1161-67.

Coleman, Hugh W. and Steele, W. Glenn (1999), *Experimentation and uncertainty analysis for engineers* (2nd edn.; New York: Wiley) xvii, 275 p.

Coulter, W.H. (1956), 'High speed automatic blood cell counter and cell size analyzer', *Proc. Natl. Electron. Conf.,* 12, 1034-40.

Coulter, W.H. (1953), 'Means for counting particles suspended in a fluid', *U.S. Patent No. 2,656,508*.

Crombie, T., Gow, N. A. R., and Gooday, G. W. (1990), 'Influence of Applied Electrical Fields on Yeast and Hyphal Growth of Candida-Albicans', *Journal of General Microbiology,* 136, 311-17.

Cummings, E. B. and Singh, A. K. (2003), 'Dielectrophoresis in microchips containing arrays of insulating posts: theoretical and experimental results', *Anal. Chem.,* 75 (18), 4724-31.

Davis, J. A., et al. (2006), 'Deterministic hydrodynamics: taking blood apart', *Proc. Natl. Acad. Sci. USA,* 103 (40), 14779-84.

Deamer, D. W. and Akeson, M. (2000), 'Nanopores and nucleic acids: prospects for ultrarapid sequencing', *Trends in Biotechnology,* 18 (4), 147-51.

Deblois, R. W. and Bean, C. P. (1970), 'Counting and Sizing of Submicron Particles by Resistive Pulse Technique', *Rev. Sci. Instrum.,* 41 (7), 909-16.

DeBlois, R.W. and Wesley, R.K.A. (1977), 'Sizes and concentrations of several type C oncornaviruses and Bacteriophage T2 by the resistive-pulse technique', *J. Virol. ,* 23, 227-33.

Erickson, D., Sinton, D., and Li, D. Q. (2003), 'Joule heating and heat transfer in poly(dimethylsiloxane) microfluidic systems', *Lab on a Chip,* 3 (3), 141-49.

Fan, R., et al. (2005), 'DNA translocation in inorganic nanotubes', *Nano Letters,* 5 (9), 1633-37.

Fologea, D., et al. (2005), 'Slowing DNA translocation in a solid-state nanopore', *Nano Letters,* 5 (9), 1734-37.

Gershon, H. and Gershon, D. (2000), 'The budding yeast, Saccharomyces cerevisiae, as a model for aging research: a critical review', *Mech. Ageing. Dev.,* 120 (1-3), 1-22.

Greiner, M., Pfeiffer, D., and Smith, R. D. (2000), 'Principles and practical application of the receiver-operating characteristic analysis for diagnostic tests', *Prev Vet Med,* 45 (1-2), 23-41.

Grier, D. G. (2003), 'A revolution in optical manipulation', *Nature,* 424 (6950), 810-6.

Griffin, D. H. (1994), *Fungal Physiology, 2nd Edition* (New York: John Wiley & Sons, Inc.).

Grosse, C. and Schwan, H. P. (1992), 'Cellular membrane potentials induced by alternating fields', *Biophysical Journal*, 63 (6), 1632-42.

Grover, N. B. and Woldringh, C. L. (2001), 'Dimensional regulation of cell-cycle events in Escherichia coli during steady-state growth', *Microbiology,* 147 (Pt 1), 171-81.

Han, K. H. and Frazier, A. B. (2006), 'Paramagnetic capture mode magnetophoretic microseparator for blood cells', *IEE Proc. Nanobiotechnol.,* 153 (4), 67-73.

Hanczar, B., et al. (2010), 'Small-sample precision of ROC-related estimates', *Bioinformatics,* 26 (6), 822-30.

Hartwell, L. H. and Unger, M. W. (1977), 'Unequal division in Saccharomyces cerevisiae and its implications for the control of cell division', *J. Cell. Biol.,* 75 (2 Pt 1), 422-35.

Helmstetter, C. E. (1991), 'Description of a baby machine for Saccharomyces cerevisiae', *New Biol,* 3 (11), 1089-96.

Hu, X.Y., et al. (2005), 'Marker-specific sorting of rare cells using dielectrophoresis', *Proc. Natl. Acad. Sci. USA*, 102, 15757-61.

Hua, S. Z. and Pennell, T. (2009), 'A microfluidic chip for real-time studies of the volume of single cells', *Lab on a Chip,* 9 (2), 251-56.

Jaffe, L. F. and Poo, M. M. (1979), 'Neurites Grow Faster Towards the Cathode Than the Anode in a Steady-Field', *Journal of Experimental Zoology,* 209 (1), 115-27.

Jagtiani, A. V., Sawant, R., and Zhe, J. (2006), 'A label-free high throughput resistive-pulse sensor for simultaneous differentiation and measurement of multiple particle-laden analytes', *Journal of Micromechanics and Microengineering,* 16 (8), 1530-39.

John, P. C. L. (1981), *The Cell cycle* (Seminar series / Society for Experimental Biology; Cambridge Cambridgeshire ; New York: Cambridge University Press) viii, 276 p.

Johnston, G. C. and Singer, R. A. (1983), 'Growth and the Cell-Cycle of the Yeast Saccharomyces-Cerevisiae .1. Slowing S-Phase or Nuclear Division Decreases the G1 Cell-Cycle Period', *Exp. Cell. Res.,* 149 (1), 1-13.

Jones, T. B. (1995), *Electromechanics of particles* (Cambridge ; New York: Cambridge University Press) xxii, 265 p.

Jorgensen, P. and Tyers, M. (2004), 'How cells coordinate growth and division', *Curr. Biol.,* 14 (23), R1014-27.

Kang, K. H., et al. (2006), 'Continuous separation of microparticles by size with direct current-dielectrophoresis', *Electrophoresis,* 27 (3), 694-702.

Kang, Y., et al. (2008), 'DC-Dielectrophoretic separation of biological cells by size', *Biomed. Microdevices,* 10 (2), 243-9.

Karnik, R., et al. (2005), 'Electrostatic control of ions and molecules in nanofluidic transistors', *Nano Letters,* 5 (5), 943-48.

Kasianowicz, J. J., et al. (1996), 'Characterization of individual polynucleotide molecules using a membrane channel', *Proceedings of the National Academy of Sciences of the United States of America,* 93 (24), 13770-73.

Koch, M. , Evans, A.G.R., and Brunnschweiler, A. (1999), 'Design and fabrication of a micromachined Coulter counter', *J. Micromech. Microeng.,* 9, 159-61.

Koschwanez, J., et al. (2004), 'Identification of budding yeast using a fiber-optic imaging bundle', *Review of Scientific Instruments,* 75 (5), 1363-65.

Kralj, J. G., et al. (2006), 'Continuous dielectrophoretic size-based particle sorting', *Analytical Chemistry,* 78 (14), 5019-25.

Kubitschek, H. E. (1958), 'Electronic counting and sizing of bacteria', *Nature,* 182 (4630), 234-5.

Kubitschek, H. E. and Friske, J. A. (1986), 'Determination of bacterial cell volume with the Coulter Counter', *J Bacteriol,* 168 (3), 1466-7.

Kubitschek, H.E. (1969), *in Methods in Microbiology*, eds Ribbons R. W. and Norris J. R. (London: Academic) 503.

Landau, L. D. and Lifschitz, E. M. (1959), *Fluid mechanics,* London: Addison-Wesley Pub. Co. 536 p. pp.

Lapizco-Encinas, B. H., et al. (2004), 'Insulator-based dielectrophoresis for the selective concentration and separation of live bacteria in water', *Electrophoresis,* 25 (10-11), 1695-704.

Larsen, U.D., Blankenstein, G. , and Branebjerg, J (1997), 'Microchip Coulter particle counter. ', *Proceedings of the IEEE Transducers '97 Conference* (Chicago, IL), 1319-22.

Li, J., et al. (2001), 'Ion-beam sculpting at nanometre length scales', *Nature,* 412 (6843), 166-69.

Li, J. L., et al. (2003), 'DNA molecules and configurations in a solid-state nanopore microscope', *Nature Materials,* 2 (9), 611-15.

Li, Y. L. and Kaler, K. V. I. S. (2004), 'Dielectrophoretic fluidic cell fractionation system', *Analytica Chimica Acta,* 507 (1), 151-61.

Lindegren, C. C. and Haddad, S. A. (1954), 'Growth rate of individual yeast cells', *Genetica,* 27, 45-53.

Lord, P. G. and Wheals, A. E. (1980), 'Asymmetrical division of Saccharomyces cerevisiae', *J. Bacteriol.,* 142 (3), 808-18.

Mandrusov, E., et al. (1995), 'Membrane-based cell affinity chromatography to retrieve viable cells', *Biotechnol. Prog.,* 11 (2), 208-13.

Maxwell, James Clerk and Thomson, J. J. (1904), *A treatise on electricity and magnetism* (3d edn.; Oxford,: Clarendon) 2 v.

Meller, A. and Branton, D. (2002), 'Single molecule measurements of DNA transport through a nanopore', *Electrophoresis,* 23 (16), 2583-91.

Miltenyi, S., et al. (1990), 'High gradient magnetic cell separation with MACS', *Cytometry,* 11 (2), 231-8.

Mitchison, J. M. (1958), 'The growth of single cells. II. Saccharomyces cerevisiae', *Exp. Cell Res.,* 15 (1), 214-21.

--- (2003), 'Growth during the cell cycle', *Int. Rev. Cytol.,* 226, 165-258.

Mohamed, H., et al. (2004), 'Development of a rare cell fractionation device: application for cancer detection', *IEEE Trans Nanobioscience,* 3 (4), 251-6.

Morgan, Hywel and Green, Nicolas G. (2003), *AC electrokinetics : colloids and nanoparticles* (Microtechnologies and microsystems series; Philadelphia, PA: Research Studies Press) xvi, 324 p.

Nurse, P. (1975), 'Genetic control of cell size at cell division in yeast', *Nature,* 256 (5518), 547-51.

Owe Berg , T. G. and B., Ljunggren (1982), 'The rate of growth of a single yeast cell', *Biotechnol. Bioeng.,* 24, 2739-41.

Pamme, N. (2007), 'Continuous flow separations in microfluidic devices', *Lab on a Chip,* 7 (12), 1644-59.

Parikesit, G. O. F., et al. (2008), 'Size-dependent trajectories of DNA macromolecules due to insulative dielectrophoresis in submicrometer-deep fluidic channels', *Biomicrofluidics,* 2, 24103.

Petersson, F., et al. (2005), 'Continuous separation of lipid particles from erythrocytes by means of laminar flow and acoustic standing wave forces', *Lab on a Chip,* 5 (1), 20-2.

Pohl, Herbert A. (1978), *Dielectrophoresis : the behavior of neutral matter in nonuniform electric fields* (Cambridge monographs on physics; Cambridge ; New York: Cambridge University Press) xii, 579 p.

Probstein, Ronald F. (1994), *Physicochemical hydrodynamics : an introduction* (2nd edn.; New York: John Wiley & Sons) xv, 400 p.

Radisic, M., Iyer, R.K., and Murthy, S.K. (2006), 'Micro- and Nano-technology in Cell Separation', *Int. J. Nanomedcine.,* 1, 3-14.

Ramos, A., et al. (1998), 'Ac electrokinetics: a review of forces in microelectrode structures', *Journal of Physics D-Applied Physics,* 31 (18), 2338-53.

Roberts, K., et al. (1999), 'A silicon microfabricated aperture for counting cells using the aperture impedance technique', *Canadian Journal of Electrical and Computer Engineering-Revue Canadienne De Genie Electrique Et Informatique,* 24 (3), 109-13.

Rosa, C. A. and Peter, G. (2006), *In Biodiversity and Ecophysiology of Yeasts, The Yeast Handbook,* (Heidelberg: Springer-Verlag).

Ryan, T. A., et al. (1988), 'Molecular Crowding on the Cell-Surface', *Science,* 239 (4835), 61-64.

Sabounchi, P., et al. (2008), 'Sample concentration and impedance detection on a microfluidic polymer chip', *Biomed Microdevices,* 10 (5), 661-70.

Saleh, O. A. and Sohn, L. L. (2001), 'Quantitative sensing of nanoscale colloids using a microchip Coulter counter', *Rev. Sci. Instrum.,* 72 (12), 4449-51.

--- (2003a), 'An artificial nanopore for molecular sensing', *Nano. Lett.,* 3 (1), 37-38.

--- (2003b), 'Direct detection of antibody-antigen binding using an on-chip artificial pore', *Proceedings of the National Academy of Sciences of the United States of America,* 100 (3), 820-24.

Scott, R., Sethu, P., and Harnett, C. K. (2008), 'Three-dimensional hydrodynamic focusing in a microfluidic Coulter counter', *Review of Scientific Instruments,* 79 (4), -.

Sia, S. K. and Whitesides, G. M. (2003), 'Microfluidic devices fabricated in poly(dimethylsiloxane) for biological studies', *Electrophoresis,* 24 (21), 3563-76.

Sikdar, D. N. and Hentz, S. J. (1980), 'Kinematic Structure of an Atlantic Cloud Cluster during Gate and Its Time-Variation', *Tellus,* 32 (5), 439-55.

Smeets, R. M. M., et al. (2006), 'Salt dependence of ion transport and DNA translocation through solid-state nanopores', *Nano Letters,* 6 (1), 89-95.

Sridhar, M., et al. (2008), 'Experimental characterization of a metal-oxide-semiconductor field-effect transistor-based Coulter counter', *Journal of Applied Physics,* 103, 104701.

Stowers, C., et al. (2010), 'Extending synchrony and deconvolving population effects in budding yeast through an analysis of volume growth with a structured Leslie model', *J. Biomedical Science and Engineering,* 3, 987-1001.

Stowers, C. C. and Boczko, E. M. (2007), 'Reliable cell disruption in yeast', *Yeast,* 24 (6), 533-41.

Stowers, C. C., et al. (2009), 'Periodic Fermentor Yield and Enhanced Product Enrichment from Autonomous Oscillations', *Applied Biochemistry and Biotechnology,* 156 (1-3), 489-505.

Sun, J., et al. (2010), 'Measurement of the volume growth rate of single budding yeast with the MOSFET-based microfluidic Coulter counter', *Lab on a Chip,* 10 (21), 2986-93.

Sun, J., et al. (2009), 'Experimental characterization of electrical current leakage in poly(dimethylsiloxane) microfluidic devices', *Microfluidics and Nanofluidics,* 6 (5), 589-98.

Tourovskaia, A., Figueroa-Masot, X., and Folch, A. (2005), 'Differentiation-on-a-chip: a microfluidic platform for long-term cell culture studies', *Lab on a Chip,* 5 (1), 14-9.

Trampler, F., et al. (1994), 'Acoustic cell filter for high density perfusion culture of hybridoma cells', *Biotechnology (N Y),* 12 (3), 281-4.

Tsutsui, H. and Ho, C. M. (2009), 'Cell Separation by Non-Inertial Force Fields in Microfluidic Systems', *Mech. Res. Commun.,* 36 (1), 92-103.

van Dam, K. (1996), 'Role of glucose signaling in yeast metabolism', *Biotechnol Bioeng,* 52 (1), 161-5.

Vivier, M. A., Lambrechts, M. G., and Pretorius, I. S. (1997), 'Coregulation of starch degradation and dimorphism in the yeast Saccharomyces cerevisiae', *Crit Rev Biochem Mol Biol,* 32 (5), 405-35.

Voldman, J. (2006), 'Electrical forces for microscale cell manipulation', *Annual Review of Biomedical Engineering,* 8, 425-54.

Walker, G. M. (1999), 'Synchronization of yeast cell populations', *Methods. Cell. Sci.,* 21 (2-3), 87-93.

Weinlich, M., et al. (1998), 'Simultaneous detection of cell volume and intracellular pH in isolated rat duodenal cells by confocal microscopy and BCECF', *Res Exp Med (Berl),* 198 (2), 73-82.

Wheals, A. E. (1982), 'Size control models of Saccharomyces cerevisiae cell proliferation', *Mol. Cell. Biol.,* 2 (4), 361-8.

Woldringh, C. L., Huls, P. G., and Vischer, N. O. (1993), 'Volume growth of daughter and parent cells during the cell cycle of Saccharomyces cerevisiae a/alpha as determined by image cytometry', *J. Bacteriol.*, 175 (10), 3174-81.

Wolfe, A. J. (2005), 'The acetate switch', *Microbiol Mol Biol Rev,* 69 (1), 12-50.

Xu, D., et al. (2007), 'Wide-spectrum, ultrasensitive fluidic sensors with amplification from both fluidic circuits and metal oxide semiconductor field effect transistors', *Applied Physics Letters,* 91, 013901.

Xuan, X. C., et al. (2004), 'Electroosmotic flow with Joule heating effects', *Lab on a Chip,* 4 (3), 230-36.

Zadrag, R., et al. (2006), 'Relationship between replicative age and cell volume in Saccharomyces cerevisiae', *Acta Biochem. Pol.,* 53, 747-51.

Zhe, J., et al. (2007), 'A micromachined high throughput Coulter counter for bioparticle detection and counting', *J. Micromech. Microeng.,* 17 (2), 304-13.